الجمهورية الجزائرية الديمقراطية الشعبية
People's Democratic Republic of Algeria
وزارة التعليم العالي و البحث العلمي
Ministry of Higher Education and Scientific Research

University Mohamed Khider of Biskra
Faculty of Sciences and Technology
Department: Mechanical Engineering

Ref:...

Thesis submitted for obtaining the degree of

Doctorate in: Mechanical Engineering

Option: Energetic

Study of the performance of a solar air collector with different geometrical shapes of baffles

Presented by:

Mr. Zouhair AOUISSI

Thesis defended publicly on: 26 November 2023

The jury members:

Mr. Noureddine MOUMMI	**Professor**	**University of Biskra**	**Chairman**
Mr. Foued CHABANE	**Professor**	**University of Biskra**	**Supervisor**
Mr. Noureddine BELGHAR	**Professor**	**University of Biskra**	**Examiner**
Mr. Yazid HELAL	**MCA**	**University of Ouargla**	**Examiner**

College year: 2022 / 2023

Abstract

In this work, an experimental and numerical study was presented on a solar air collector (SAC) in order to improve the thermo-hydraulic performance through rectangular baffles perpendicular to the air inside the channel (duct). In the experimental study, many cases were studied using different formations of baffles, after that, a numerical model was designed using Computational Fluid Dynamic CFD (Ansys Fluent 18.1) in the Reynolds range from *Re* = 5038 to *Re* = 10635, which was validated based on the experimental results. The turbulence model RNG k-ε was chosen because it gave closer results to the standard correlations of Dittus-Boelter and Modified Blasius, compared to the rest of the models. The results showed that the baffles play a major role in improving the heat transfer of these collectors, the effect of baffles on the heat transfer from the absorber plate to the air was understood through the local heat transfer coefficient along the channel and the velocity fields and their rays, as choosing the appropriate coordination of shape, angle of inclination, number and positioning play an effective role in improving the thermo-hydraulic performances.

Keywords: solar air collector, CFD, Ansys Fluent 18.1, heat transfer, baffles, thermo-hydraulic performances.

ملخص

في هذا العمل، تم تقديم دراسة تجريبية ورقمية على جامع الهواء الشمسي من أجل تحسين الأداء الهيدروليكي و الحراري من خلال حواجز مستطيلة متعامدة مع الهواء داخل القناة (مجرى الهواء). في الدراسة التجريبية، تمت دراسة العديد من الحالات باستخدام حالات مختلفة من الحواجز، وبعد ذلك تم تصميم نموذج رقمي باستخدام ديناميكيات السوائل الحاسوبية Ansys Fluent 18.1 في في نطاق رينولدز من Re = 5038 إلى Re = 10635 والتي تم التحقق من صحتها بناءً على النتائج التجريبية. تم اختيار نموذج الاضطراب RNG k-ε لأنه يعطي نتائج أقرب إلى العلاقات المعيارية Modified Blasius و Dittus-Boelter و ذلك بالمقارنة بباقي النماذج. أظهرت النتائج أن الحواجز تلعب دورًا اساسيا في تحسين الانتقال الحراري للمجمعات الشمسية، وقد تم فهم الية تأثير الحواجز على انتقال الحرارة من لوح الامتصاص إلى الهواء من خلال معامل نقل الحرارة المحلي على طول القناة وكذلك حقول السرعة و اشعتها، حيث أن اختيار التنسيق المناسب للشكل وزاوية الميل والعدد والموضع دورًا فعالًا في تحسين الأداء الهيدروليكي و الحراري.

الكلمات المفتاحية : لاقط شمسي هوائي, ديناميكيات السوائل الحاسوبية, Ansys Fluent 18.1
الانتقال الحراري, الاداء الهيدروليكي الحراري

Résumé

Dans ce travail, une étude expérimentale et numérique a été présentée sur un capteur solaire à air afin d'améliorer les performances thermo-hydrauliques à travers des chicanes rectangulaires perpendiculaires à l'air à l'intérieur du canal (conduit). Dans l'étude expérimentale, de nombreux cas ont été étudiés en utilisant différentes formations de chicanes, après cela, un modèle numérique a été conçu en utilisant Computational Fluid Dynamic CFD (Ansys Fluent 18.1) dans l'intervalle de Reynolds de Re = 5038 à Re = 10635, qui a été validé sur la base des résultats expérimentaux. Le modèle de turbulence RNG k-ε a été choisi car il donnait des résultats plus proches des corrélations standard de Dittus-Boelter et de Blasius modifié, par rapport au reste des modèles. Les résultats ont montré que les chicanes jouent un rôle majeur dans l'amélioration du transfert de chaleur de ces capteurs, l'effet des chicanes sur le transfert de chaleur de la plaque absorbante à l'air a été compris à travers le coefficient de transfert de chaleur local le long du canal et les champs de vitesse et leurs rayons, En plus de ça, le choix de la coordination appropriée de la forme, de l'angle d'inclinaison, du nombre et du positionnement joue un rôle efficace dans l'amélioration des performances thermohydrauliques.

Mots clé : capteur solaire à air, CFD, Ansys Fluent 18.1, transfert thermique, performances thermo-hydrauliques.

Dedication

I dedicate this work to:
My mother and my father
My brothers and sister
My friends
My family
I pray to God "Allah" to perpetuate them and grant them success in their lives.

Acknowledgment

I must first of all thank ALLAH, for having given me the health and the strength to accomplish this work.

The time has come to express my gratitude to my thesis director, ***Pr. Foued CHABANE,*** *Professor at the University of Biskra, for entrusting me with this work, for his precious advice throughout the realization of this work.*

I would like to sincerely thank ***Pr. Noureddine MOUMMI,*** *Professor at the University of Biskra, for having done me the honor of accepting to chair the jury of this thesis.* ***Pr. Nourredine BOULGHAR,*** *Professor at the University of Biskra,****Dr.Yazid Helal*** *, Doctor at University of Ouargla the for agreeing to examine this work.*

Also I would like to express my deep gratitude and thanks to the family of the Mechanical Engineering Department of the University of Biskra, and all the members of the LGM and LGEM laboratories, in particular ***Dr. Mahboub CHAWKI.***

Finally, we thank all CFD committee members, including their leaders ***Pr. Abdelhafid MOUMMI.***

TABLE OF CONTENTS

TABLE OF CONTENTS i
LIST OF FIGURES iv
LIST OF TABLES vii
NOMENCLATURE vii
General introduction 1
I. Literature review 4
I.1 Introduction 4
I.2 Improve thermo-hydraulic performance techniques 4
I.2.1 Active techniques 5
I.2.2 Passive techniques 5
I.2.3 Compound techniques 5
I.3 Solar air collector without baffles (smooth plate) 6
I.4 The influence of the addition of different geometrical shapes of baffles 7
I.5 Effect of the baffles on flow and thermal fields 27
I.6 Influence of the absorber geometry 29
I.7 Influence of passage geometry of SACs with baffles 32
I.8 Conclusion 39
II. Experimental study of the SAC with baffles 41
II.1 Introduction 41
II.2 The global solar irradiation 41
II.2.1 Geographic site 42
II.2.2 Model of the global solar irradiation 42
II.2.2.1 Variable equations a, b, c, and d 43
II.2.3 The ultimate mathematical model of solar radiation 44
II.3 Experimental design 45
II.3.1 Technical characteristics of the uses baffles 47
II.3.2 Uses devises 48
II.3.2.1 Pyranometer 49
II.3.2.2 Thermocouple 49

II.3.2.3 Aspirator 49
II.3.3 Uncertainty of the parameters 49
II.4 Experimentally studied cases 49
II.5 Conclusion 52
III. Numerical study 54
III.1 Introduction 54
III.2 Modeling 54
III.2.1 Model selected 56
III.3 CFD set-up 57
III.3.1 Creation of the CFD geometry 58
III.3.2 Meshing the CFD geometry 59
III.3.3 Turbulence models 62
III.4 Validation 63
III.5 Conclusion 68
IV. Results and discussion 70
IV.1 Introduction 70
IV.1.1 Discuss and compare results of radiation 70
IV.1.2 Analytical view of the change in solar radiation throughout the year 72
IV.1.3 Thermal performances 75
IV.1.3.1 Bottom and absorber plates temperature 75
IV.1.3.1 Inlet and outlet temperature 76
IV.1.3.2 Local temperature and Nusselt numbers 77
IV.1.3.3 Heat transfer coefficient 80
IV.1.3.4 Pressure drop 81
IV.1.3.5 Thermal efficiency 82
IV.2 The first part of the numerical study 83
IV.2.1 Evaluation of the Nusselt number 84
IV.2.2 Pressure drop 84
IV.2.3 Evaluation of the heat transfer coefficient 85
IV.2.4 Evaluation of the friction factor 87
IV.2.5 The thermo-hydraulic performance factor (THPF) 88
IV.3 The second part of the numerical study 89

IV.3.1 Evaluation of the Nusselt number 90
IV.3.2 Evaluation of the heat transfer coefficient 91
IV.3.3 Contours of temperature 93
IV.3.4 Evaluation of the friction factor 95
IV.3.5 The thermo-hydraulic performance factor (THPF) 96
IV.4 Conclusion 96
General conclusion 99
References 102

LIST OF FIGURES

Figure I.1 Flat plate solar air collector. 4
Figure I.2 Schematic of the thermo-hydraulic performance techniques 5
Figure I.3 Schematic view of the SAC [10]. 6
Figure I.4 Variation of collector efficiency at different mass flow rates [10]. 7
Figure I.5 Absorber plate with baffles in semi-cylindrical form [13]. 8
Figure I.6 Thermal efficiency as function of time of the day (with and without baffles)[13]. 8
Figure I.7 Studied cases of SAC, with dimensions: (A) Smooth plate; (B) Case 1(Up); (C) Case 2(Down); (D) Case 3(Middle); (E) Case 4(All)[14]. 9
.**Figure I.8** The local heat transfer coefficient in terms of the length of SAC for all cases, at Re ¼ 2370[14]. 10
Figure I.9 Geometric shape with division using CFD[15]. 10
Figure I.10 Variation of isotherms with arc-baffles[16] 11
Figure I.11 Test section with wavy rib arrangements [18]. 12
Figure I.12 Three-dimensional calculation model [19]. 12
Figure I.13 Temperature of the absorber for different cases [19]. 13
Figure I.14 SAC frame, and three types of absorber plates [20]. 14
Figure I.15 Variation of the efficiency as a function of mass flow rates: v-groove, finned, and smooth plate SACs [20]. 14
Figure I.16 Ribs arrangement on collector plate [21]. 15
Figure I.17 Types and the view of absorber plates in the collector box, (a) type I, (b) type II, (c) type III [22]. 15
Figure I.18 The baffle shape [23]. 16
Figure I.19 Variation of ΔP as a function of Re [23]. 16
Figure I.20 Thermal efficiency as a function of time of the day, according to mode 4, mode 2 [23]. 17
Figure I.21 Sketch of V-shaped baffles with perforation [24]. 17
Figure I.22 Nusselt number of the baffled duct as a function of Reynolds number [24]. 18
Figure I.23 Comparison of a thermo-hydraulic performance parameter in a roughened SAC duct, considering the use of both solid and perforated baffles. [24]. 18
Figure I.24 Thermo-hydraulic performance parameter of the roughened duct as a function of Reynolds number, considering various values of relative roughness height [24]. 18
Figure I.25 V-shape configurations [28]. 19
Figure I.26 Transversal cut SAC with baffles [29]. 19
Figure I.27 Global experimental radiation and proposed models as a function of the time of the day [29]. 20
Figure I.28 Temperature comparison with and without baffles [29]. 20
Figure I.29 Performance comparison [29]. 20
Figure I.30 Experimental device [30]. 21
Figure I.31 Descriptive diagram of baffles [30]. 21
Figure I.32 SAC with the finned system [31]. 22
Figure I.33 The efficiency factor of SAC with the air flow for different cases [31]. 22
Figure I.34 Types of absorber plates[32]. 23
Figure I.35 Geometry of the studied SACs: a) case of PPSC, b) case of PPSCB, c) case of PPSCDB. 24
Figure I.36 Experimental setup [33]. 24
Figure I.37 Variation of thermal efficiency of SAC in terms of time [33]. 25
Figure I.38 The temperature distribution in air domain of SAC [33]. 25
Figure I.39 Absorber plate temperature [33]. 26

Figure I.40 Offset plate fin absorber plate [34]. 26
Figure I.41 Thermal efficiency as a function of mass flow rates: G (kg/hm^2), a: offset plate baffles, L = 2:5 cm; b: offset plate baffles, L = 5 cm; c: offset plate baffles, L = 10 cm; d: offset plate baffles, L =20 cm; e: double glazing, f: triple glazing [34]. 27
Figure I.42 Geometry of the computational domain [11]. 28
Figure I.43 Thermal fields for Re =100 [11]. 28
Figure I.44 A cross-section of the curved solar air collector [35]. 29
Figure I.45 Schematic view of the textile-based SAC, and the smooth plate SAC (FP-SAC). 1: SAC outer body, 2: Textile fabric support, 3:Textile fabric, 4:Transparent top cover, 5:Air inlet-outlet to the textile fabric [36]. 29
Figure I.46 Change in the energy efficiency of the TB-SAC and FP-SAC [36]. 30
Figure I47. Visualization of tested SACs; (a) "Flat Baseline" design; (b) first novel design "Wave-shaped Type I"; (c) second novel design "Wave-shaped Type II [37]. 30
Figure I.48 Collector heat output, Q, vs. irradiance I[37]. 31
Figure I.49 Comparison of the thermal efficiency η, of SACs versus the temperature rise (Tout - Tamb)/I [37]..... 32
Figure I.50 Downward-type SAC, with an internal recycle and baffles attached [39]. 32
Figure I.51 Collector efficiency (T_{fi} =298K) [39]. 33
Figure I.52 Schematic diagram of SAC [40]. 34
Figure I.53 Efficiency of solar air heater obtained from each model[40]. 34
Figure I.54 A diagram illustrating a SAC with a double-pass configuration is shown, where the second channel incorporates porous media. [41]. 35
Figure I.55 The thermal efficiency of the double-pass SAC relation to the temperature rise, revealing its impact on the system's performance. [41]. 35
Figure I.56 Double pass flat plate SAC (DPFPSAH) [42]. 36
Figure I.57 (a) double pass v-corrugated plate SAC, abbreviated as DPVCPSAH. (b) A section of the v-corrugated absorber plate [42]. 36
Figure I.58 The effect of flow rates on the thermal efficiency of the double pass flat (DPFPSAH), and v-corrugated (DPVCPSAH) plate SAC [42]. 37
.**Figure I.59** The geometry of the new absorber plate. 37
Figure I.60 Discretization scheme of the calculation domain [44]. 38
Figure I.61 Jha et al and Tyagi et al ducts [28, 45, 46]. 38
Figure I.62 baffled SAC with internal obstacles attached, and external recycle [47]. 39
Figure II.1. Location of the experimental setup in the map (Biskra) 42
Figure II.2 The solar air collector. 45
Figure II.3 Schematic diagram of our SAC, (1: transparent cover, 2: absorber plate, 3: baffles, 4: air duct, 5 iron support, 6: aspirator, 7: bottom plate, 8: insulation, 9: inlet airflow, 10: outlet airflow, 11 solar radiation, 12: tool table). 46
Figure II.4 Cross-section of the smooth plate SAC. 46
Figure II.5 Temperature measurement points. 47
Figure II.6 The rectangular shape of the baffles. 48
Figure II.7 Cross section of the channel showing the position of baffles. 48
Figure II.8 Used devices, Thermocouple, Aspirator Pyranometer, and airflow pressure device. 48
Figure II.9 Dimensions of baffles inside the channel of M cases. 51
Figure II.10 Different cases of the position baffles β =135°. 51
Figure II.11 Cases M and H 51
Figure III.1 CFD analysis diagram. 58
Figure III.2 Studied models. 59

Figure III.3 The effect of the number of nodes in Mode M at m=0.032Kg/s, I=911W/m^2, and T_{out}=316.9k. **60**
Figure III.4 Meshing the system into contract taking into account Y^+ **61**
Figure III.5 Computational grid, a: channel with baffles, b: near of the wall. **61**
Figure III.6 Predicted values of Nusselt Number for different k-ε, and k- ω turbulence models with Dittus-Boelter correlation. **62**
Figure III.7 Predicted values of Friction Coefficient for different k-ε, and k-w turbulence models with Modified Blasius correlation. **62**
Figure III.8 CFD boundary conditions. **64**
Figure III.9 Outlet temperature as a function of hours of the day for mass flow rate m=0.024kg/s. **64**
Figure III.10 Outlet temperature as a function of hours of the day for mass flow rate m=0.032 kg/s. **65**
Figure III.11 Methodology of validation diagram (M and H cases). **66**
Figure III.12 Numerically and experimentally outlet temperature in terms of mass flow rates for the two cases M and H respectively. **66**
Figure III.13 Heat transfer coefficient as a function of mass flow rates for H case. **67**
Figure III.14 variation of Temperature difference as a function of mass flow rates. **67**
Figure IV.1 Global solar irradiation, according to the season of the winter between measurement, and prediction model. **71**
Figure IV. 2 Global solar irradiation, according to the season of the spring between measurement, and prediction model. **71**
Figure IV.3 Global solar irradiation, according to the season of the summer between measurement, and prediction model. **71**
Figure IV.4 Global solar irradiation, according to the season of the autumn between measurement, and prediction model. **72**
Figure IV.5 Global solar irradiation, and prediction model, according to all the seasons. **72**
Figure IV.6 Global solar radiation of measurements in terms of global solar radiation prediction. **73**
Figure IV.7 The constants a, b, c, and d in every month. **74**
Figure IV.8 Temperature of the absorber plate as a function of the length, in the different mass flow rates. **75**
Figure IV.9 Temperature of the bottom plate as a function of its length for different mass flows. **76**
Figure IV.10 Temperature difference as a function of hours of the day, at different mass flows for all cases. **77**
Figure IV.11 Discretization of zones. **78**
Figure IV.12 The local temperature of air as a function of hours of the day, at different mass flows. **79**
Figure IV.13 The local Nusselt numbers as a function of hours of the day, at different flows. **80**
Figure IV14. The heat transfer coefficient as a function of hours of the day at different flows in all cases. **81**
Figure IV.15 The pressure drop as a function of mass flow rates and different angles of inclination. **82**
Figure IV16. The thermal efficiency as a function of hours of the day at different flows for all cases **83**
Figure IV.17 Nusselt number in terms of Reynolds number for all cases. **84**
Figure IV.18 Pressure drop as a function of Reynolds number for all cases. **85**
Figure IV.19 The local heat transfer coefficient as a function of the lenght channel at Re=5368. ..... **85**
Figure IV.20 The local heat transfer coefficient as a function of the length of channel for the case of 18 baffles at different Reynolds numbers. **86**
Figure IV.21 local heat transfer coefficient as a function of the lenght (18 baffles case). **87**
Figure IV.22 The friction factor as a function of Reynolds number in all cases. **87**
Figure IV.23 The THPF as a function of Reynolds numbers for all cases. **88**
Figure IV.24 Velocity path lines between two baffles (18 baffles case at Re=9515). **89**
Figure IV.25 Velocity field and the direction of vortices at the level of baffle (18 baffles case at Re=9515). **89**
Figure IV.26 The studied modes. **90**

Figure IV.27 Change in Nusselt number in terms of Reynolds number for all cases..... 90
Figure IV.28 Change in the local heat transfer coefficient in terms of the local change for all positions. 91
Figure IV.29 Change in Nusselt number in terms of Reynolds number for all cases. 91
Figure IV.30 Change in the local heat transfer coefficient in terms of the local change for all positions. 92
Figure IV.31 Change in the local heat transfer coefficient of the case H middle for different Reynolds numbers. ... 93
Figure IV.32 Contours of turbulent intensity, mode H middle at Re=10257. 93
Figure IV.33 Temperature of the absorber plate as a function of channel length. 94
Figure IV.34 Temperature of the three modes (with the same number of baffles). 94
Figure IV.35 Change of the Friction coefficient as a function of Reynolds number. 95
Figure IV.36 The THPF as a function of Reynolds number for all modes. 96

LIST OF TABLES

Table I.1 Width of the rooms for different models. 13
Table I.2 Pressure drop for different SAC cases. 13
Table I.3 Experimental results. 22
Table I.4 Further enhancement of performance for: (a) I_0 =830 W/m^2 33
Table II.1 The constants of the model of global solar irradiation, according to the month from January to June. 42
Table II.2 The constants of the model of global solar irradiation, according to the month from July to December. . 43
Table II.3 The constants of the model of equation (2) 43
Table II.4 The constants of the model of equation (3) 44
Table II.5 The constants of the model of equation (4) 44
Table II.6 The constants of the model of equation (5) 44
Table II.7 the dimensions of the SAC's elements. 47
Table II.8 Thermo-physical characteristics of the elements. 47
Table II.9 The uncertainty of the parameters 49
Table III.1 Meshing effect. 60
Table III.2 Boundary conditions. 64

NOMENCLATURE

A	Cross section area, m^2
Cp	Specific heat of air, J/kgK
DH	Hydraulic diameter, m,
h	Heat transfer coefficient,W/m^{2}K
I	Turbulence intensity, %
K	Turbulent kinetic energy, m$^{2/}$s^2
L	Length of the air duct, m
m	Mass flow rate,Kg/s
P	Perimeter m,
ΔP	Pressure drop, pa.
Q	Useful heat gain, W/m^2
S	Absorber plate area, m^2
U	Velocity, m/s

Dimensionless parameters:

f	Friction factor
Nu	Nusselt number
Pr	Prandtl number
Re	Reynolds number
Y+	Dimensionless wall distance

Greek symbols:

λ	Thermal conductivity, W/m^2K.
ρ	Density, Kg/m^3
v	Kinematic viscosity, m^2/s

Subscripts:

0	Smooth
b	Bulk
in	Inlet
out	Outlet
amb	ambient
CFD	Computational Fluid Dynamic
THPF	Thermo-Hydraulic Performance Factor
w	Wall
SAC	Solar air collector

GENERAL INTRODUCTION

General introduction

Energy is an essential component for the growth and development of human societies. It is the driving force behind almost every aspect of modern life, from transportation and industry to healthcare and communication. Without energy, societies would be unable to progress and thrive as they do today. Energy can come in many forms, including fossil fuels, and renewable sources. Each of these sources has its unique advantages and disadvantages, and the choice of which to use depends on a variety of factors, such as availability, cost, and environmental impact [1, 2].

The use of energy has led to tremendous advancements in technology and infrastructure, enabling the creation of vast transportation networks, modern communication systems, and efficient industrial processes. These advancements have helped to improve living standards and reduce poverty in many parts of the world, allowing people to lead more comfortable and fulfilling lives. However, the use of energy also comes with significant environmental and social impacts. The burning of fossil fuels, for example, has been linked to climate change and air pollution, while the construction of large-scale energy projects can displace communities and harm biodiversity. As such, it is important for societies to consider the long-term sustainability of their energy use, and to seek out cleaner and more efficient sources of energy wherever possible. Solar energy is a clean and renewable source of energy that is becoming increasingly popular around the world. The use of solar power has grown rapidly in recent years, as people seek to reduce their reliance on fossil fuels and minimize their impact on the environment. Solar energy has a wide range of applications in our daily lives, from powering homes and businesses to providing electricity to remote communities and powering transportation. Solar panels can be installed on rooftops or in open fields to capture the energy of the sun. [3-5].

One of the most important ways to exploit solar energy is to convert it into thermal energy using the so-called solar air collectors (SAC) [6]. The use of solar air collectors (SAC) is becoming increasingly popular as a means of harnessing solar energy for heating and cooling applications. However, one of the challenges associated with these systems is improving heat transfer within the collectors to increase their overall efficiency. This is where the use of baffles inside the channel comes in. By strategically placing barriers inside the channel, it is possible to disrupt the flow of fluid and create turbulence, which in turn improves heat transfer. The design of the baffles is crucial, as it needs to balance the need for increased turbulence with the need to maintain an efficient flow of fluid through the duct. To achieve this, in this study we focused on designing the geometric shape of the barriers to optimize their thermal and hydraulic performance, where we used both experimental and numerical analysis, including the use of Computational Fluid Dynamics (CFD) software such as Ansys Fluent 18.1, to simulate and visualize the flow within the SAC. The combination of experimental and numerical analysis is a powerful approach, as it allows researchers to validate their simulations with real-world data and make adjustments as needed. By doing so, they can refine their designs and identify the most effective methods for improving heat transfer within the collectors.

In the first chapter of the study, we explored the topic of improving the efficiency of solar thermal collectors by introducing baffles in the channel. We explained the concept of adding baffles to disrupt the flow of fluid and create turbulence, which in turn improves heat transfer. To achieve this, the researchers conducted both CFD and experimental studies to test the effectiveness of different designs and configurations of baffles. Numerical simulations were carried out using software such as Ansys Fluent 18.1, while experimental studies involved the construction and testing of physical models of the collectors. The researchers also noted that the effectiveness of the obstacles depended on their geometric shape, spacing, and orientation. By experimenting with different configurations, they were able to identify the most effective designs to improve the performance of the collectors. The first chapter of the study provided an in-depth analysis of the research conducted on improving the thermal efficiency of the SAC by adding baffles to the duct.

In the second chapter, our experimental work was dealt with in sequence, where the applied side was explained, starting from the structure to measuring the results. Many obstacles formations were presented inside the channel, whose inclination angles, numbers, and positions were studied.

After the experimental work, we entered the CFD analysis in the third chapter, which includes three stages before proceeding with extracting the results, which are the study of the effect of division, choosing a model turbulence to flow validation with the experimental results, and finally validation with the experimental results.

In the last chapter, the results were presented and discussed the results, as a function of the thermo-hydraulic performances of this studied collector.

This study achieved optimal configurations in regarding to thermal and hydraulic factors, while also comprehensively characterizing the heat transfer mechanisms through assessments of thermal diffusion, fluid velocity, and pressure.

Chapter I

I. Literature review

I.1 Introduction

Thermal energy is a vital aspect of our daily lives and is used for a variety of purposes, such as drying and heating, among others. To harness this energy from the sun, a device called a solar air collector (SAC) is utilized Fig I.1, which converts the sun's energy into thermal energy [7]. The operating principle of these collectors involves the exchange of energy between the fluid and the absorber plate. The greater the heat transmission between the fluid and the absorber plate caused a higher of the thermal efficiency. This is why many studies aim to improve the thermal efficiency of SAC by developing techniques that enhance the thermal transfer among the fluid and the absorber, taking into consideration the pressure drop for the collector. SAC with baffles are one such example of a technique aimed at improving the thermal efficiency of SAC. Baffles are fins that are installed inside the collector to enhance the thermal transfer between the fluid and the absorber plate. The main idea behind using baffles is to increase the turbulence intensity of the fluid inside the collector, which in turn leads to a higher heat transfer rate; this increase in the thermal efficiency of the collector, making it more efficient energy-gathering device. In this chapter, we aim to highlight the most important works and findings of these technologies, with a focus on studies of SAC with baffles. By reviewing the latest advancements in this field, we hope to provide insights into the current state of the art and help guide future research in this area. Overall, the use of SAC with baffles represents a promising approach to improving the thermal efficiency of SAC [8, 9]. By exploring the potential of this technique, we can continue to advance the use of renewable energy sources and reduce our dependence on traditional energy sources. In the future, the development of more advanced and efficient SAC with baffles has the potential to play an important role in shaping the energy landscape of our world.

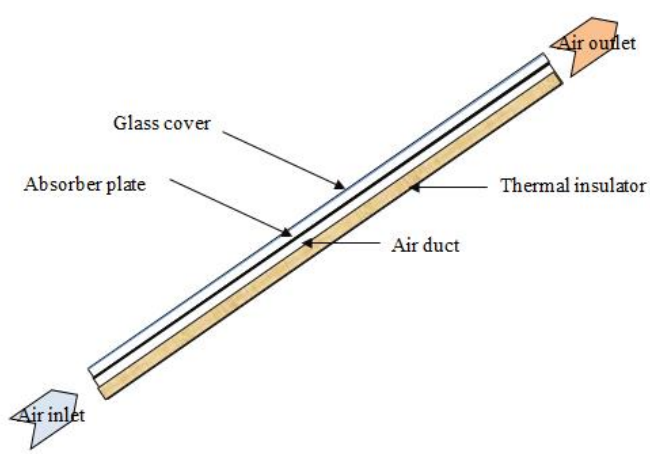

Figure I.1 Flat plate solar air collector.

I.2 Improve thermo-hydraulic performance techniques

There are many technical improvement methods available to increase the heat exchange within SAC, each with its own advantages and disadvantages. The selection of the most suitable

method depends on various factors, such as the collector's size, type, application, and cost-effectiveness. Nevertheless, these technical advancements offer great potential for enhancing the performance and competitiveness of solar thermal energy systems in the future. There are three main ways to improve the heat exchange within solar thermal collectors[2], which are summarized as follows:

I.2.1 Active techniques

Mainly depends on external forces used to improve heat exchange, the efficiency of the system hinges on harnessing these forces to optimize thermal performance and enhance overall energy transfer.

I.2.2 Passive techniques

To increase heat transfer coefficients by altering the flow behaviour, specific surfaces or geometries are required in the flow channel. This can involve integrating artificial roughness or external surfaces, which can be achieved without the need for direct external power. However, it should be noted that these techniques may result in an increase in fluid pressure drop.

I.2.3 Compound techniques

In this area of improvement it incorporates both technologies to improve thermal and hydraulic performance Fig I.2.

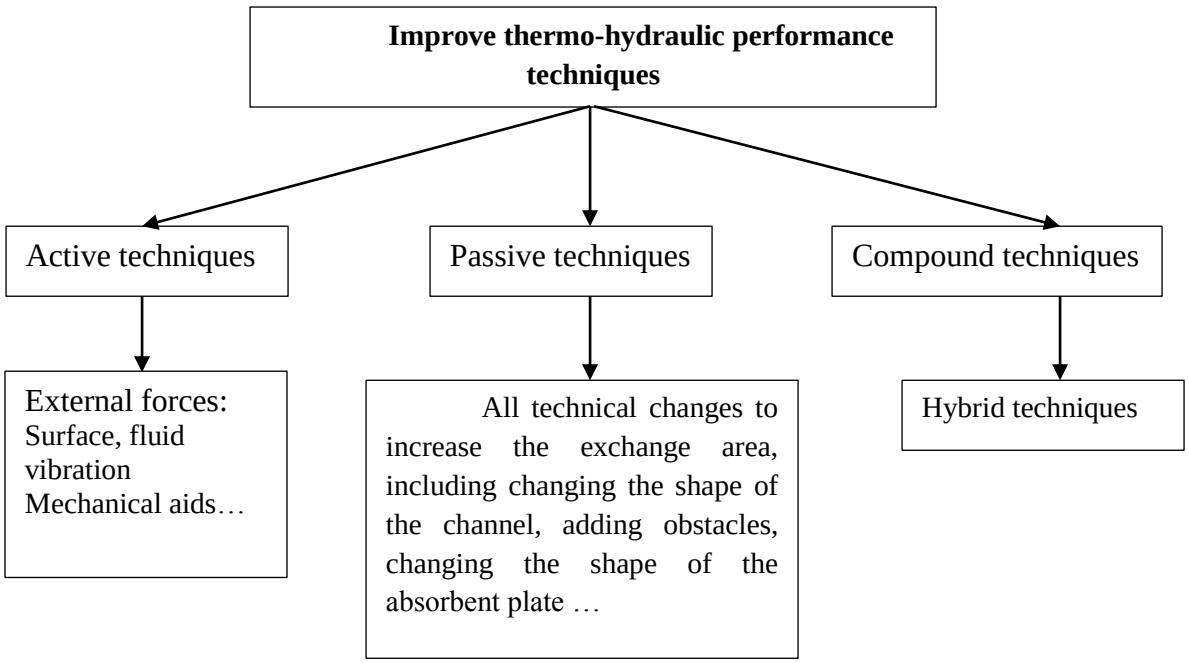

Figure I.2 Organigram of the thermo-hydraulic performance techniques.

In our study, it was relied on to improve the heat transfer on the compound techniques, in this sense; the previous studies available in the literature were selected.

I.3 Solar air collector without baffles (smooth plate)

Typically, the absence of baffles in a solar collector is commonly employed as a baseline reference point for various investigations in the field. The rationale behind this practice is to establish a point of comparison for the examination of the impact of different factors on the performances of the solar collector. By utilizing this reference case, researchers can identify the changes in thermal and hydraulic behavior that result from the inclusion of baffles, and more accurately quantify the benefits and drawbacks of such modifications. In this study, several cases were examined and compared to the reference case to determine the effectiveness of different baffle configurations in optimizing solar collector performances. In this context Chabane et al., [10] report study of an experimental of a SAC with a smooth plate (without baffles) Fig I.3, this work pointed to determine the optimal thermal performances. It was changed the mass flow rates, where they use five values, also they changed the solar intensity, tilt angle, and outside temperature. This study was done in order to find out the thermal behavior of this SAC with the this design.

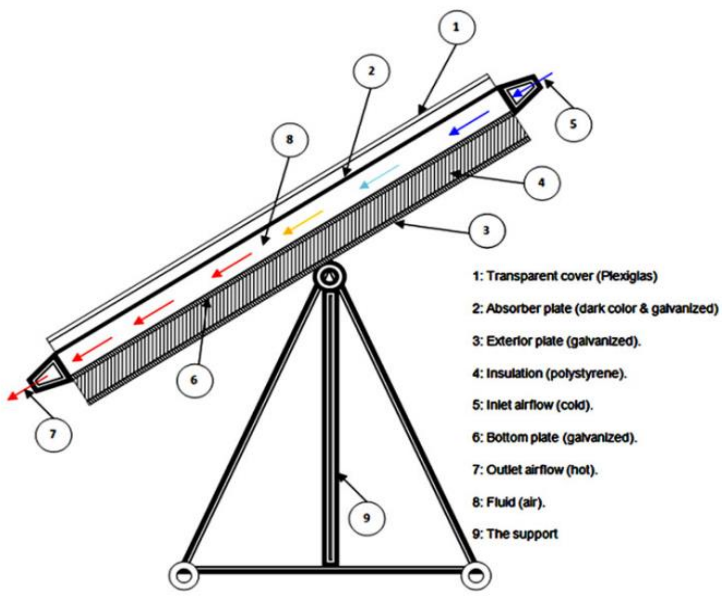

Figure I.3 Schematic view of the SAC [10].

Through the results of this research, which is mainly represented in the study of heat transfer under a fixed of operating conditions to improve the thermal efficiency, it was found that for mass flow rate m=0.0202 kg/s, the efficiency found to be higher than the mass flow rates m=0.0108 kg/s m=0.0161 kg/s, where the best value of efficiency was η=58.30% at 13:15 h, Fig I.4.

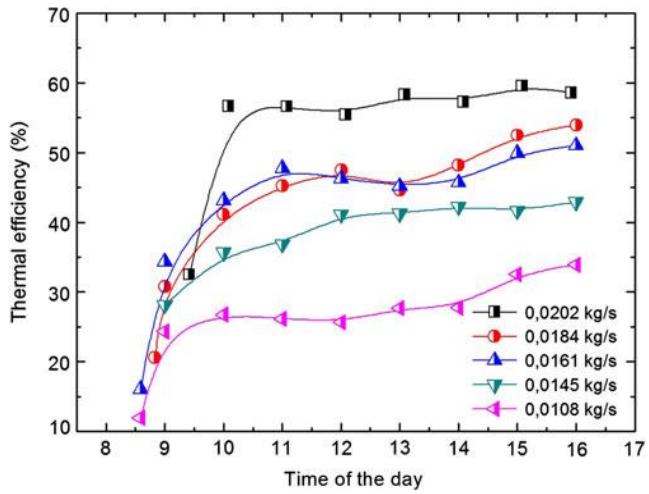

Figure I.4 Variation of collector efficiency at different mass flow rates [10].

Similarly, we remark that the results showed after changing the mass flow rates was affecting directly in the temperature of the bottom plate, and the absorber plate.

I.4 The influence of the addition of different geometrical shapes of baffles

One of the most effective methods for improving thermal performances of collectors is the inclusion of baffles within the collector channel. The use of baffles can significantly enhance heat transfer rates by increasing the flow of fluid through the collector, and increasing the surface area available for heat transfer. There is a wide range of ideas and concepts present in the literature regarding the form, number, and position of baffles within a SAC. For instance, some researchers propose the use of tapered or twisted baffles to promote more turbulent flow, while others suggest using a combination of straight and curved baffles for improved heat transfer. Additionally, the number and placement of baffles can be vary depending on the specific design of the collector, and the intended application. As such, exploring and testing these different baffle configurations is a vital step toward developing more efficient and effective SACs for widespread use. [8, 11-18]. Chabane et al., [19] studied experimentally the thermo-hydraulic performances of SACs with and without baffles, the shape of these baffles is semi-cylindrical, for the tow configuration, where the angle of inclination of collector β= 38 °.

This study was conducted to calculate the thermal efficiency of this SAC with and without baffles, for different air flows, after that monitoring the outlet temperature change. The work presented that the thermal efficiency of the SAC with semi-cylindrical formed of baffles was larger 19 % than the SAC with smooth plate Fig I.5.

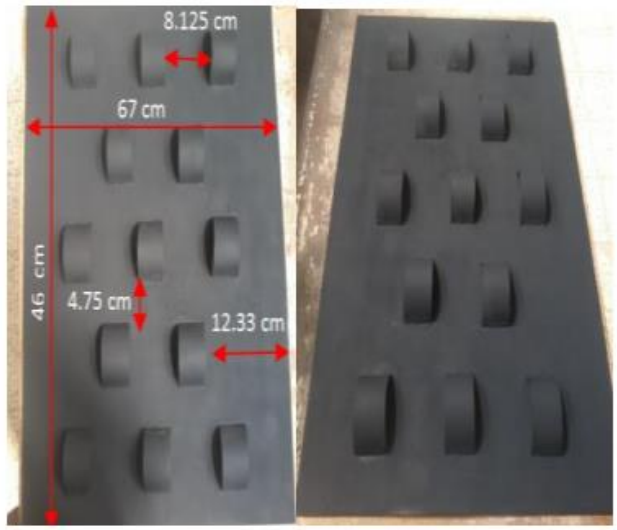

Figure I.5 Absorber plate with baffles in semi-cylindrical form [19].

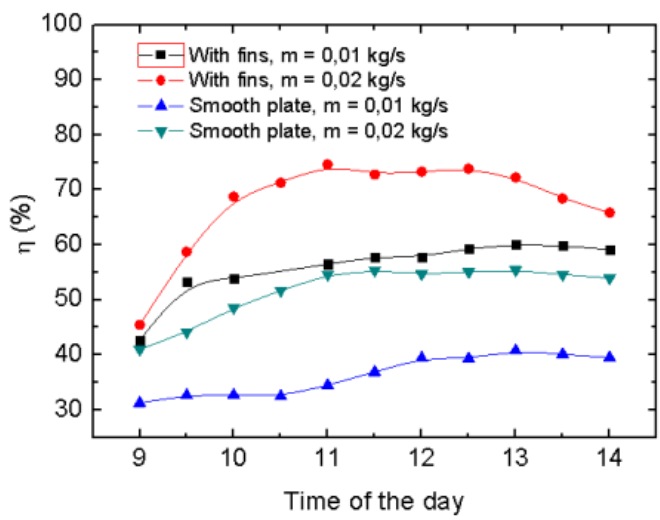

Figure I.6 Thermal efficiency as function of time of the day (with and without baffles)[19].

In the same background, Bensaci et al., [20] changed the local of their rectangular baffles in the an experimental and CFD investigations of SAC (Fig I. 7), where the study confirmed that the positions of baffles are effects on the THPF of the SAC, that is means not just the geometrical shape of them, but its positions plays a great role in that. The new position effects on the coefficients of local convective heat transfer and the thermal efficiency therefore on heat transfer in general.

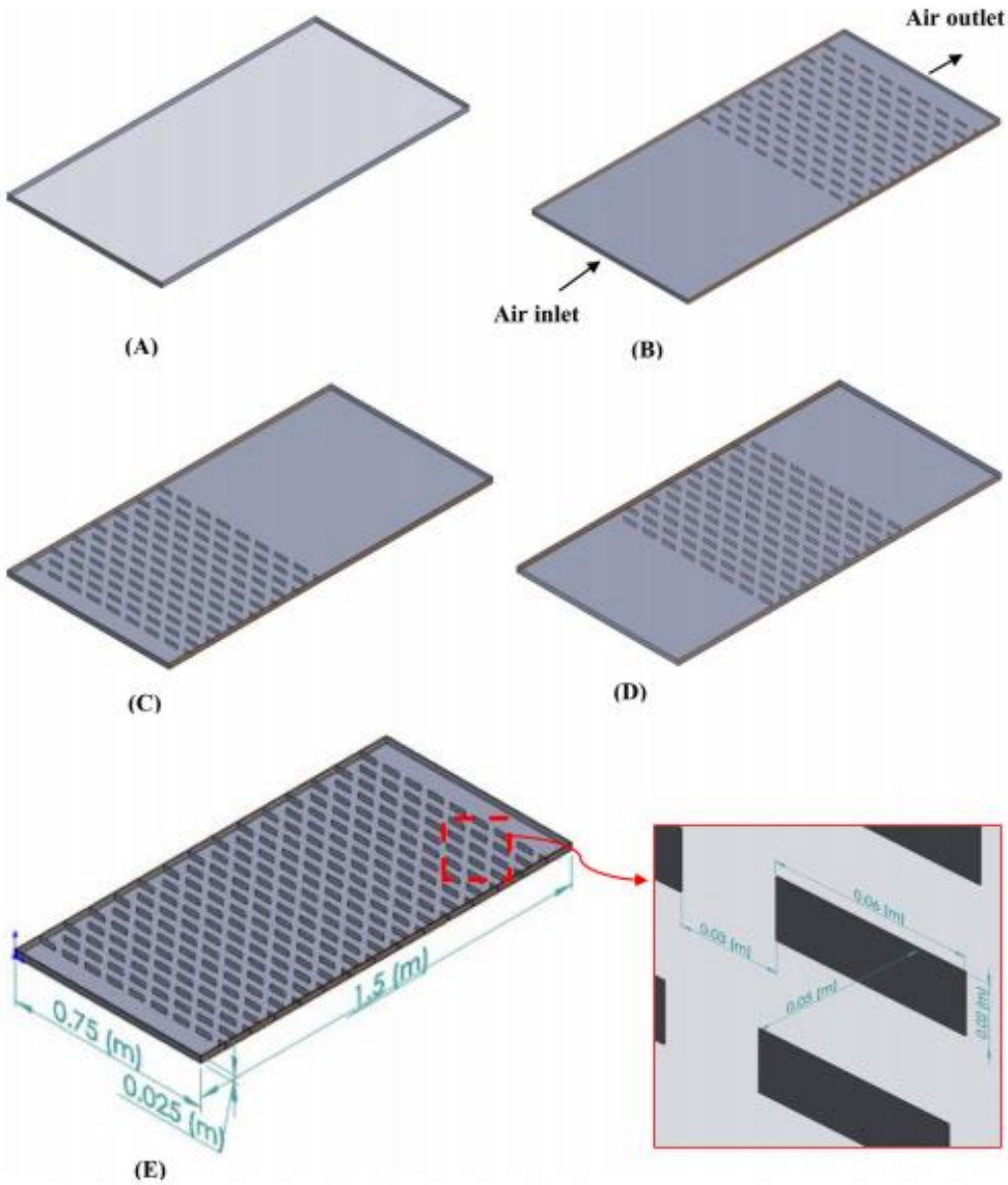

Figure I.7 Studied cases of SAC, with dimensions: (A) Smooth plate; (B) Case 1(Up); (C) Case 2(Down); (D) Case 3(Middle); (E) Case 4(All)[20].

In this work four cases have been studied case 1, 2, 3, and 4 classified according to the percentage and position of the baffles, 50% in the beginning, 50% in the middle, and 50%, at the end 100% (Fig I.8).

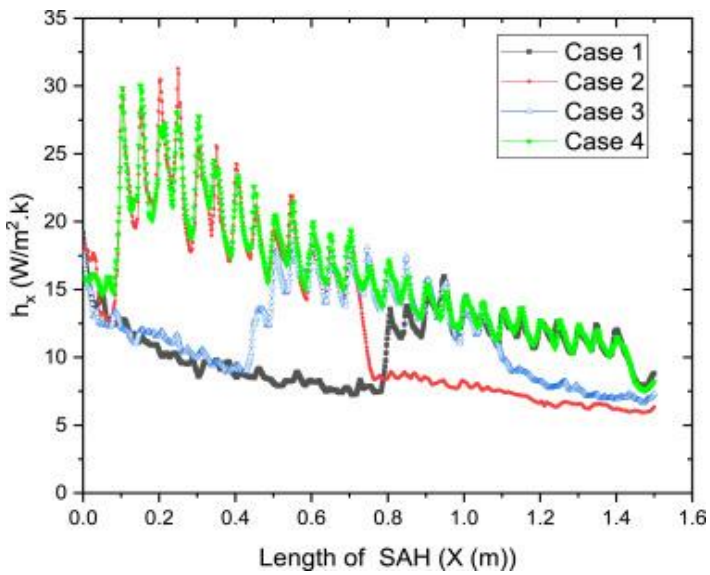

Figure I.8 The local heat transfer coefficient in terms of the length of SAC for all cases, at Re ¼ 2370[20].

The airflow over a diamond-shaped obstruction on the hot surface of the lower wall of a rectangular duct was simulated by Menni et al., [21]. As the Reynolds number increased, there was a significant amount of recirculating flow, which led to an improvement in the rate of heat exchange. The Nusselt number ratio between the modified and the simple duct was from 5.046 to 17.794% for Reynolds numbers from Re=12,000 to 32,000 respectively (Fig I.9). The highest temperature was observed downstream of the diamond-shaped baffles. In the same year, Menni et al., [22] did a numerical study using a commercial CFD to solve a numerical problem related to the impact of arc-baffles spacing on various factors including streamlines, temperature distributions, heat transfer, pressure drop, and thermal enhancement factor. They also studied the effect of an increased shape of baffles inside the channel on thermal and hydraulic performance (Fig I.10) [23].

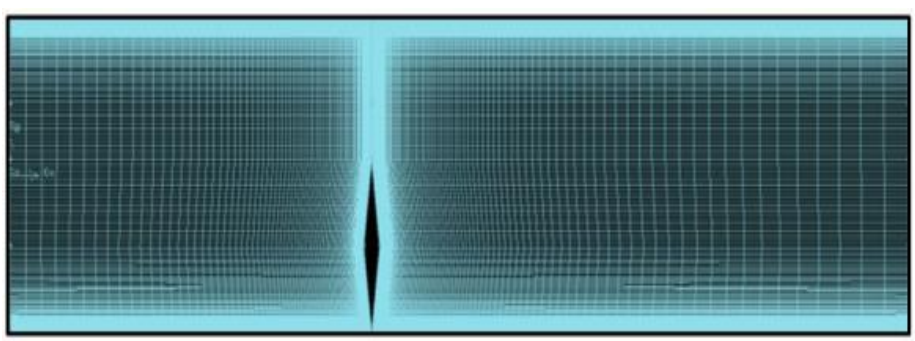

Figure I.9 Geometric shape with division using CFD[21].

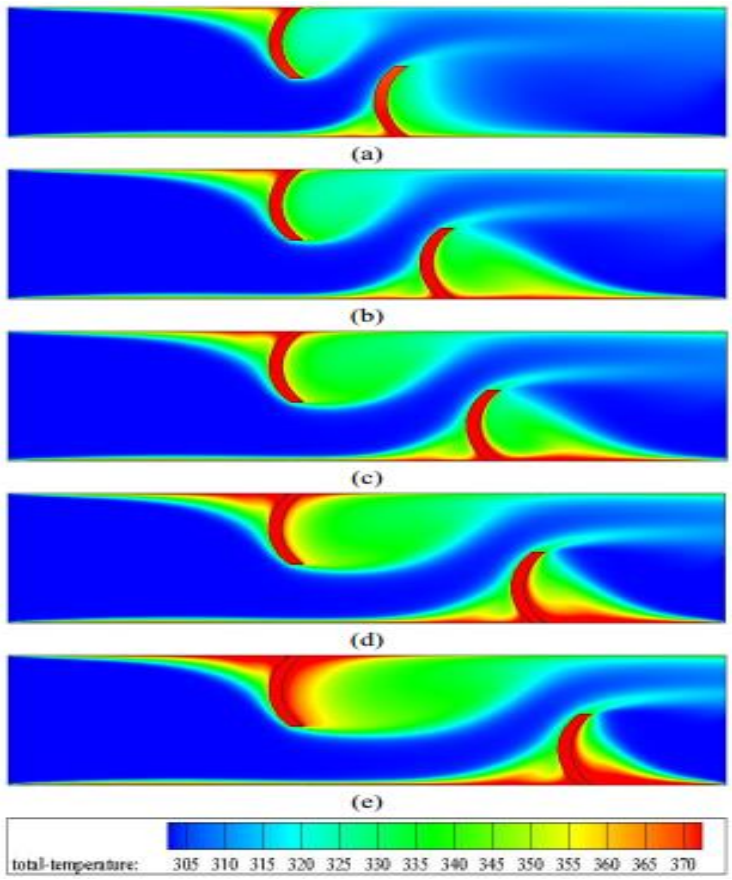

Figure I.10 Variation of isotherms with arc-baffles[22]

Khanoknaiyakam et al., [24] ensured an experimental study of a SAC with V-shaped baffles. The study aimed to investigate the thermal performance of a single-pass solar air collector (SAC) with V-shaped of baffles installed in a rectangular duct. The channel had a width to height ratio of AR=10, and contained baffles with ratios of e/H=0.2, 0.3, and 0.4. The inclination angle of the baffles concerning the direction of airflow was set to α= 30. The experimental setup consisted of a rectangular duct made of galvanized sheet and painted black to enhance solar absorption. The duct was placed on a flat surface. The V-shaped baffles were made of aluminum and were arranged in a staggered pattern to enhance the turbulence of the airflow (Fig I.11).

To estimate the thermal performance of the SAC, the researchers measured the collector's thermal efficiency, heat gain, and outlet temperature for different values of flow rates, and solar radiation intensity. The results showed that the thermal efficiency of the SAC increased with the increase in the mass flow rates, and the radiation intensity. Additionally, the use of V-shaped baffles enhanced the SAC's thermal performance, with a higher thermal efficiency and heat gain observed for baffles with larger ratios of e/H.

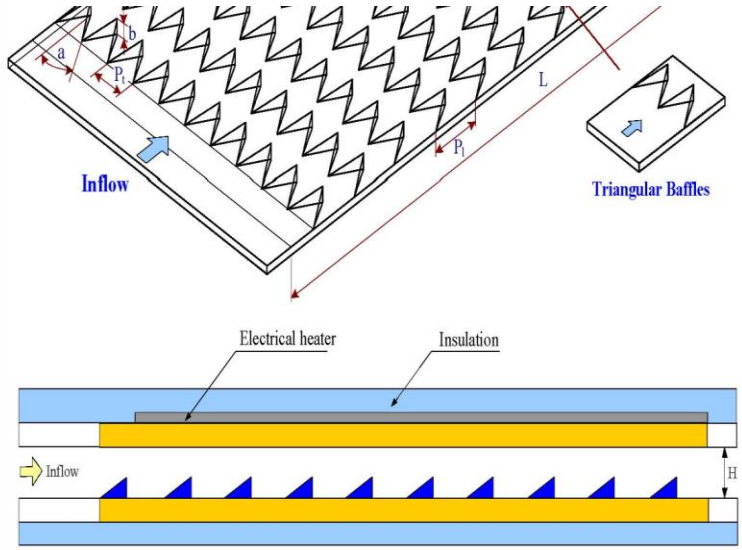

Figure I.11 Test section with wavy rib arrangements [24].

The addition of V-shaped baffles causes a high-pressure drop, also an increase in the heat energy exchange. In the same field, Hu et al., [25] did an experimental and theoretical work of the heat transfer inside a new model of SAC, the baffles were recognized to split the SAC internally into five rooms (Fig I.12).

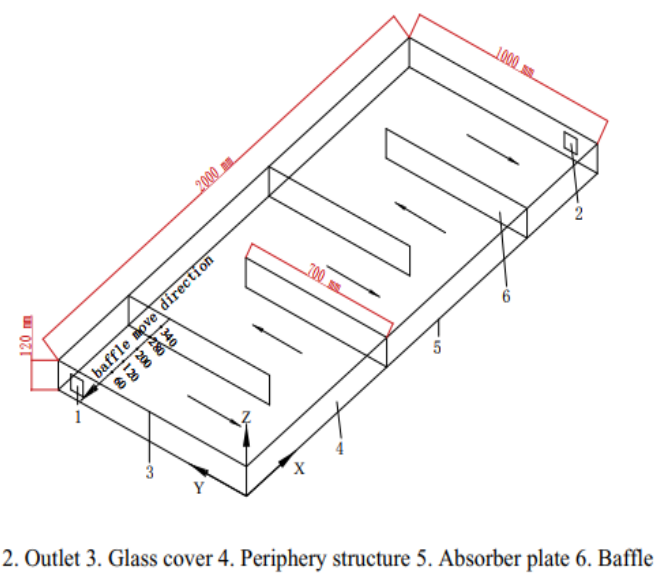

Figure I.12 Three-dimensional calculation model [25].

Through these experimental and theoretical investigations, it was found that the first room width has a major effect on the thermal performances (Fig I.13), and a little effect on the hydraulic performances Table I.1. For the width w=200 mm the thermal efficiency has the highest value which is greater to x=16.90% compared to the SAC with baffles evenly distributed.

Table I.1 Width of the rooms for different models.

MODEL	CHAMBER				
	1	2	3	4	5
0	400	400	400	400	400
1	60	485	485	485	485
2	120	470	470	470	470
3	200	450	450	450	450
4	280	430	430	430	430
5	340	415	415	415	415

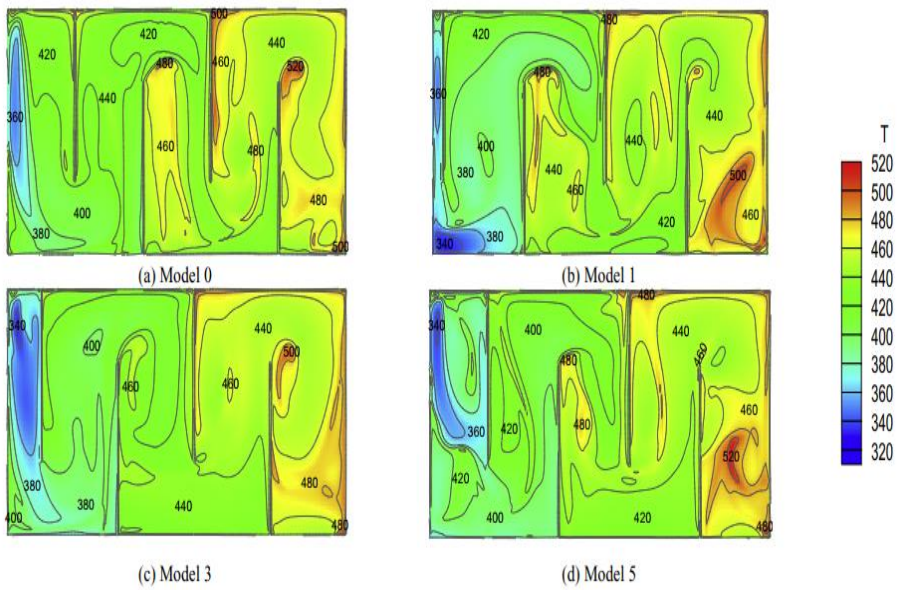

Figure I.13 Temperature of the absorber for different cases [25].

Table I.2 Pressure drop for different SAC cases.

Inlet velocity ($m.s^{-1}$)	Pressure drop of each model (Pa)					
	0	**1**	**2**	**3**	**4**	**5**
2	1.12	0.44	0.13	0.52	0.94	**0.86**
3	9.51	7.95	7.84	8.97	9.83	**9.33**
4	4.03	1.91	1.17	2.97	4.40	**4.01**
6	9.55	4.69	3.89	7.71	11.34	**8.58**

Karim [26] did an experimental study of SACs with three kinds, SACs with a flat plate, with finned, and with V-corrugated, for two modes; double pass and single pass (Fig I.14).

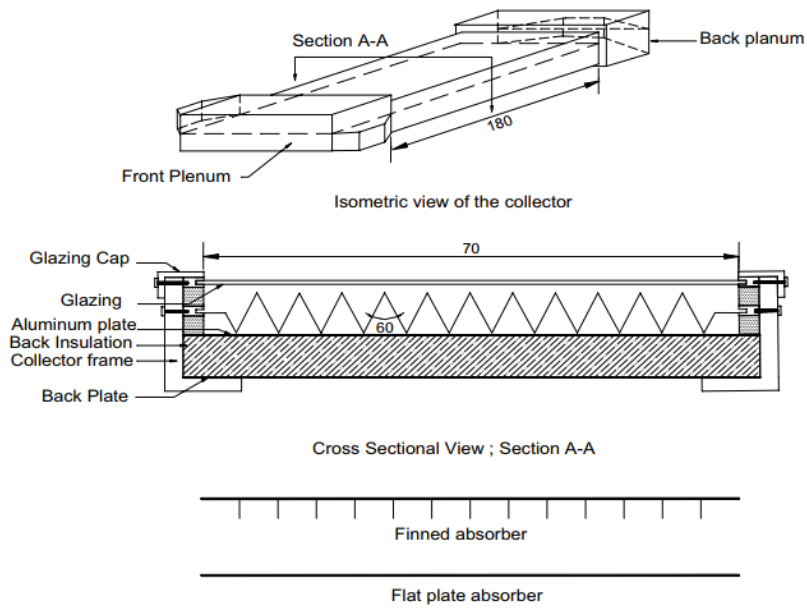

Figure I.14 SAC frame, and three types of absorber plates [26].

Through the work, it was establish that the best collector kind in terms of efficiency is the v-corrugated SAC. The operation of double pass improves the thermal efficiency compared with the single pass; this enhancement shows accurately in the flat plate SACs (Fig I.15).

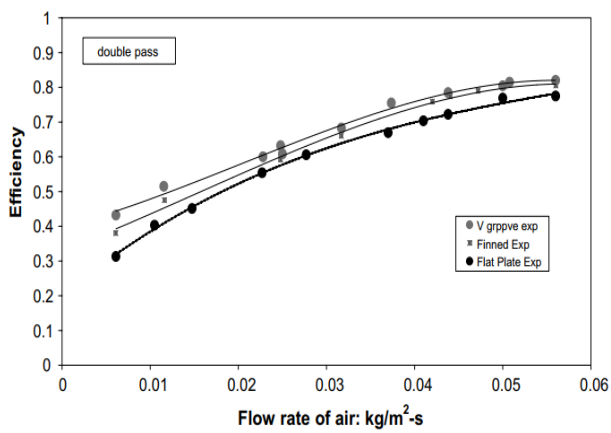

Figure I.15 Variation of the efficiency as a function of mass flow rates: v-groove, finned, and smooth plate SACs [26].

Wang et al., [27] ensured an experimental study of a SAC with s-shapes of baffles (Fig I.16). This collector has airways, where is designed in order to increase the heat exchange from the absorber plate to the air, also for facilitating air passage to improve the hydraulic performances. In this work, a comparative study was conducted to analyze the impact of several significant factors on thermal efficiency and the temperature differential between the inlet and outlet. The findings were subsequently compared to those of the flat plate SACs.

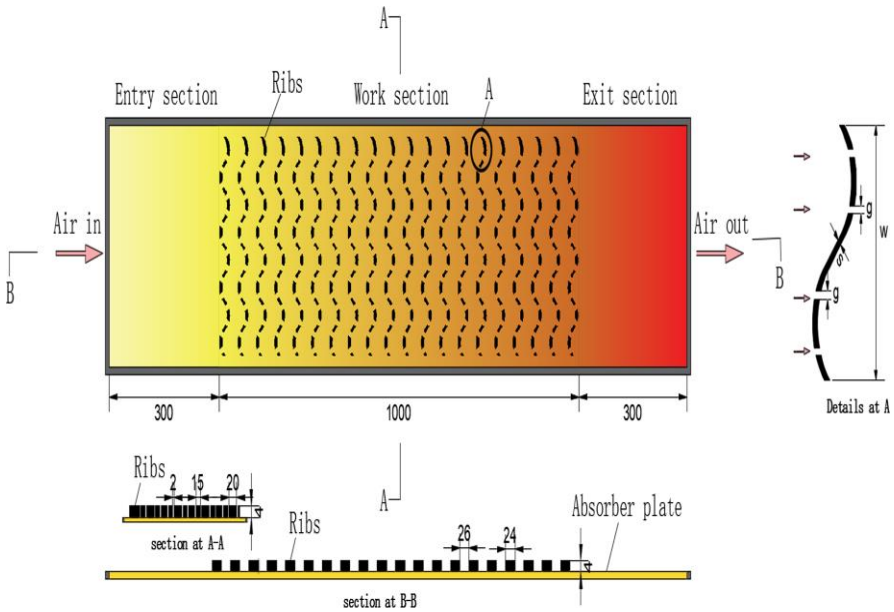

Figure I.16 Ribs arrangement on collector plate [27].

A significant improvement in thermal efficiency was recorded compared with the SAC with a flat plate. The factors that affected heat transfer in this study are the structure of the rib, air passage height, the air mass flow rates, solar radiation, and roughened surfaces.

Ozgen et al., [28] fixed an experimental study of a SAC, its channel consists of a bottom flat-plate, and the absorber plate.

Figure I.17 Types and the view of absorber plates in the collector box, (a) type I, (b) type II, (c) type III [28].

The duct has cans made of aluminum into the tow plate of the channel (Fig I.17), this method was used to improve the thermal performances of the heater with increasing the airflow rates, these leads an increase in the heat exchange from the absorber plate to the fluid. There are three types of absorber plates were studied in this search, the first one (type I) where the cans are arranged criss-cross on the absorber plate, in the second one is arranged regularly (type II), and the last one is flat plate without cans (type III). The best thermal efficiency was recorded in the first type, where the cans created turbulence in the duct of collector.

An experimental study was conducted by Chabane et al., [29] to investigate heat transfer in a SAC (cross-flow heat exchanger), with rectangular fins placed perpendicular with the air stream (Fig I.18). The experiment comprised four cases, as follows: Mode 1 consisted of six baffles positioned at the air stream's entry, Mode 2 involved placing six baffles in the middle of the air stream, and Mode 3 entailed positioning six baffles at the end of the air stream, and the final mode involved placing all 18 baffles across the entire air duct.

Figure I.18 The baffle shape [29].

They aimed to focus on the important of the efficiency of the thermal transfer inside the SAC. It was concluded that the thermal efficiency increases by an important value with adding the baffles. Comparing different configurations, it was observed that installing baffles across the entire air stream (Mode 4) resulted in higher efficiency compared to the other modes (Mode 1, Mode 2, and Mode 3). Furthermore, the analysis indicated that Mode 2 exhibited the most favourable performance while Mode 4 had a higher pressure drop than Mode 2, the performances of both modes was relatively similar. Hence, installing baffles in the center of the air stream was deemed the optimal configuration (Fig I.19, 20).

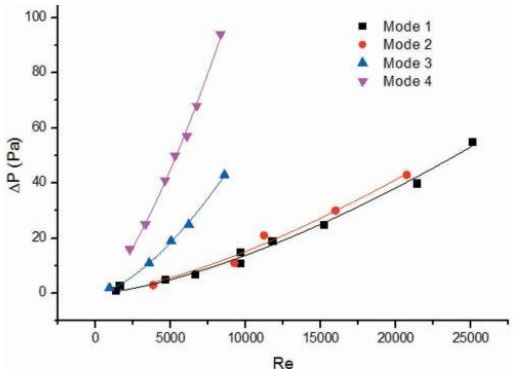

Figure I.19 Variation of ΔP as a function of Re [29].

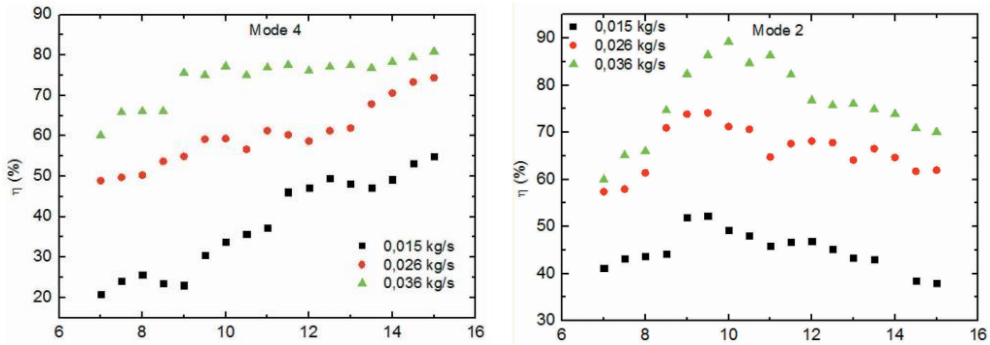

Figure I.20 Thermal efficiency as a function of time of the day, according to mode 4, mode 2 [29].

Chamoli et al., [30] experimentally analyzed the flow characteristics, and heat transfer for V-down perforated baffles (Fig I.21). The duct of the collector was divided into three sections: the inlet, outlet, and test section. Within this collector, an electric heater was installed to provide a consistent heat flux of 1000W/m² to the absorber plate.

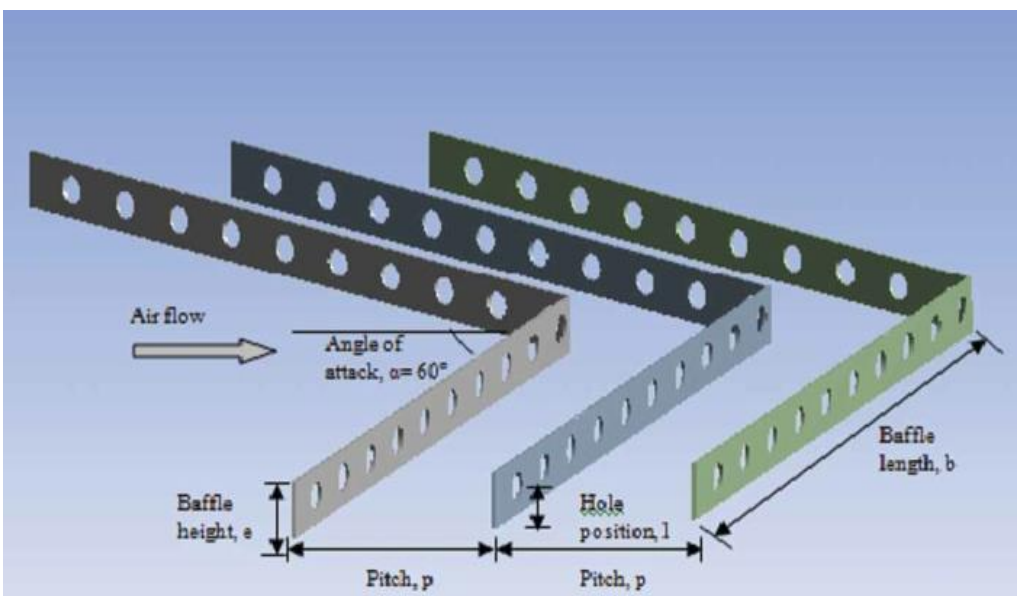

Figure I.21 Sketch of V-shaped baffles with perforation [30].

The parameters of this study are the relative roughness pitch (P/e), the relative roughness (e/H), the open area ratio (β), the Reynolds number, the friction factor (f), and the Nusselt number (Nu). This study confirmed that the Nusselt number is directly related to the relative roughness height, where the Nu increases with the increase in relative roughness height up to 0.514 (Fig I.22).

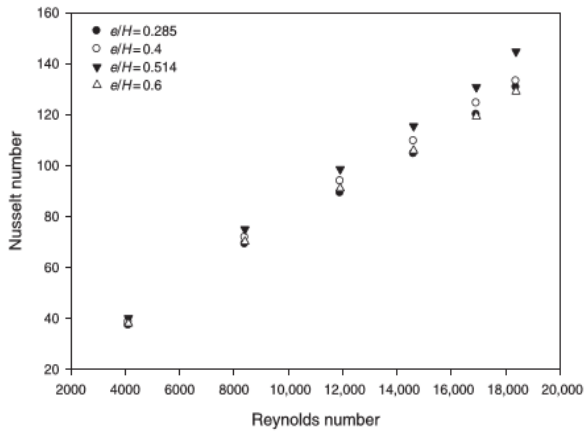

Figure I.22 Nusselt number of the baffled duct as a function of Reynolds number [30].

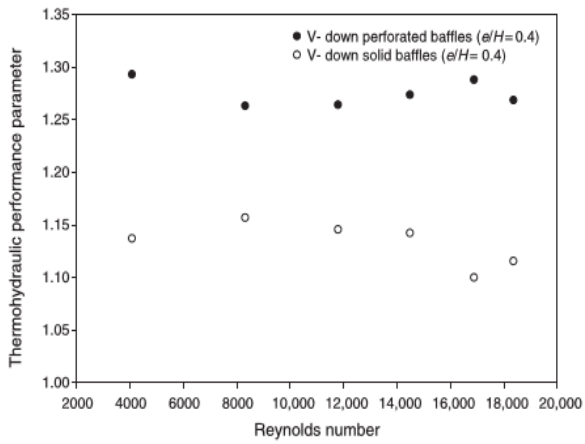

Figure I.23 Comparison of a thermo-hydraulic performance parameter in a roughened SAC duct, considering the use of both solid and perforated baffles. [30].

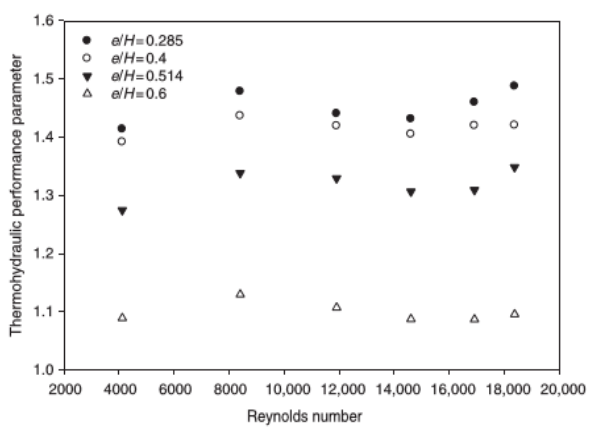

Figure I.24 Thermo-hydraulic performance parameter of the roughened duct as a function of Reynolds number, considering various values of relative roughness height [30].

Through the results, it was concluded that the V-down perforated baffled in the roughened duct is thermo-hydraulically better than the smooth duct SAC, and the perforated baffles are better than solid baffles (Fig I.23, 24).

With the same shape of V-shape obstacles, many researchers have developed this shape by changing the dimensions or adding parts (Fig I.25) [31-33].

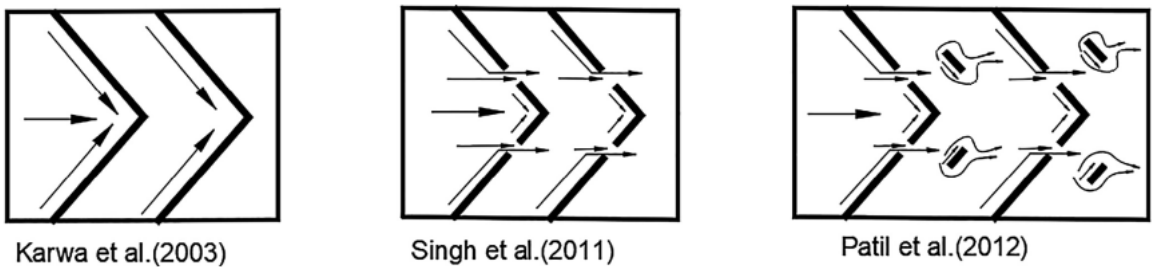

Figure I.25 V-shape configurations [34].

Chabane et al., [35] investigated an experimental study of SAC in Algeria (Biskra region), with cylindrical shape of baffles (Fig I.26), its diameter D= 6cm, and height h= 2cm.

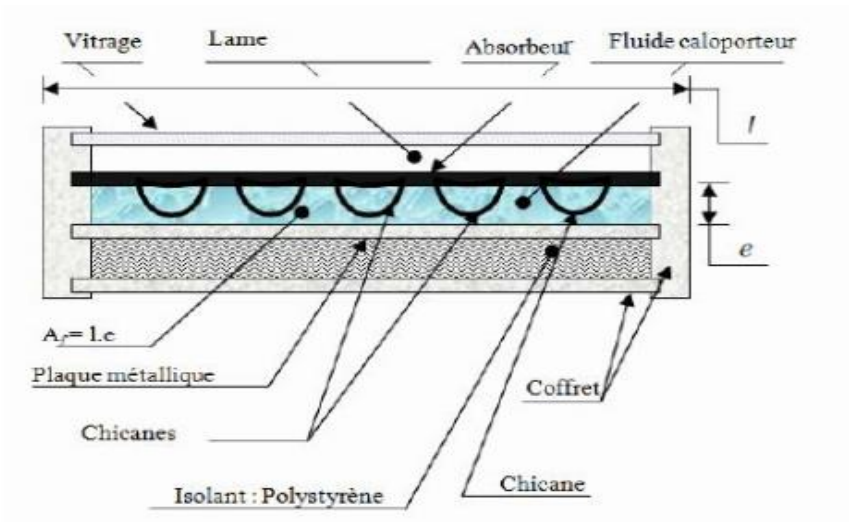

Figure I.26 Transversal cut SAC with baffles [35].

The results were about the heat transfer, and generally the temperature in the most of components of this SAC, the thermal efficiency with and without baffles, the change of direct and diffuse radiation, also the global one for two models, and the experimental one. This study showed some of the most used models of rayonment, like model of Kasten, and the model of M.Capderou. All of these characteristics are as a function of other variables (time of the day, mass flow rates). The results of global solar radiation, confirmed that the experimental results and the results of the proposed models were very close (Fig I.27).

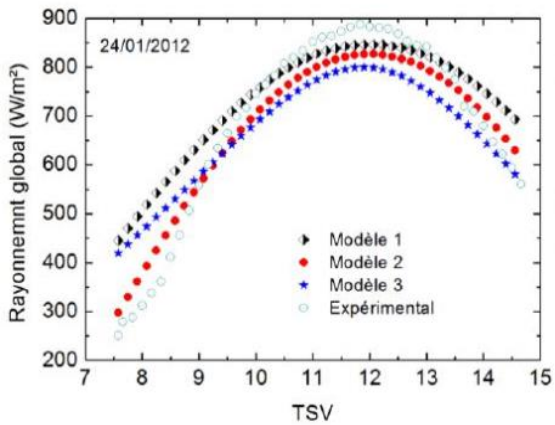

Figure I.27 Global experimental radiation and proposed models as a function of the time of the day [35].

The study also showed that the presence of baffles has increased the thermal performance of the SAC (Fig I.28, 29).

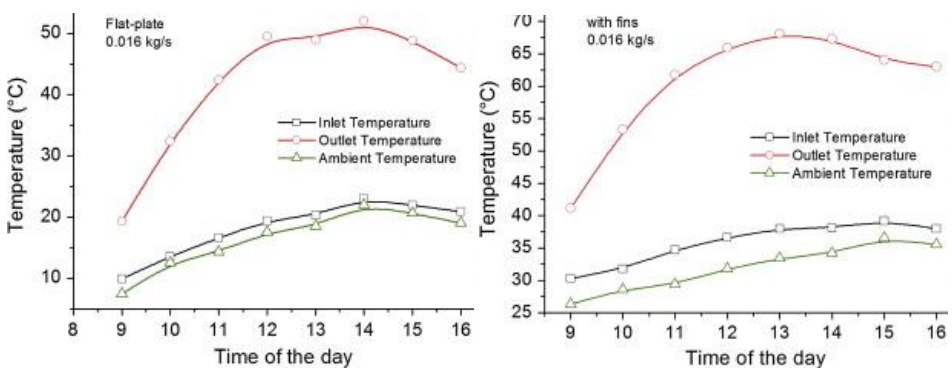

Figure I.28 Temperature comparison with and without baffles [35].

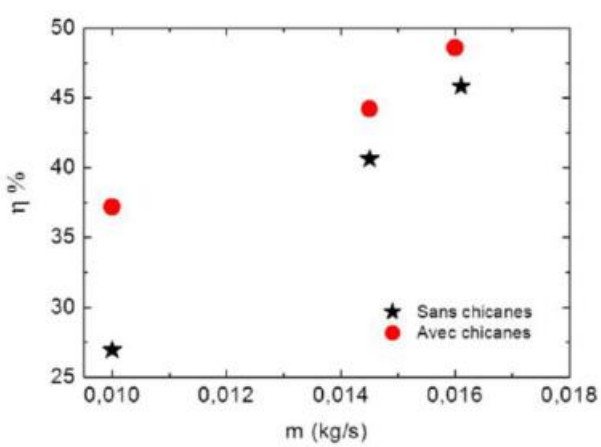

Figure I.29 Performance comparison [35].

In order to develop a SAC, Aoues et al., [36] prepared a series of experiments on the heat transfer inside a flat plate SAC (Fig I.30). During this work, it was measured the solar radiation, wind speed, mass flow rates, ambient, inlet, and outlet temperatures.

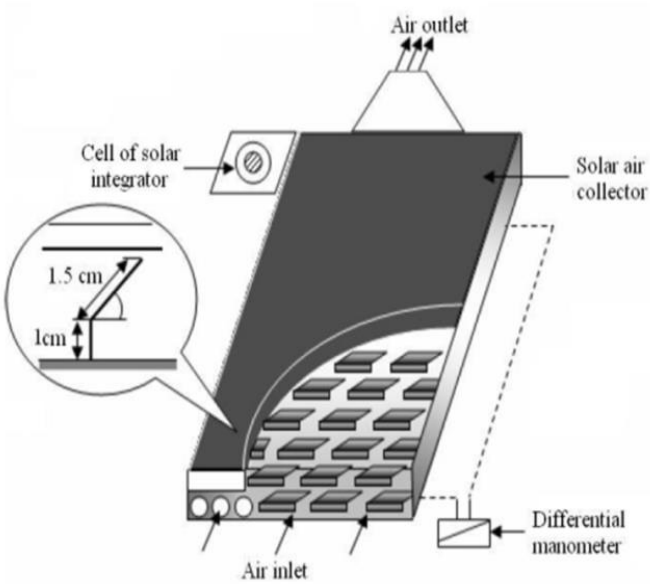

Figure I.30 Experimental device [36].

The dynamic air stream is equipped with rows of thin metal baffles welded perpendicular to the flow, these baffles have two different forms: model 1, and model 2 (Fig I.31), the first one with an angle of inclination α=60°, and the second α= 120°, they are spaced by a distance d = 10 cm, and d = 5cm, according to the two configuration, A and B; which is differentiated by the number of rows equal 152 and 256 baffles respectively.

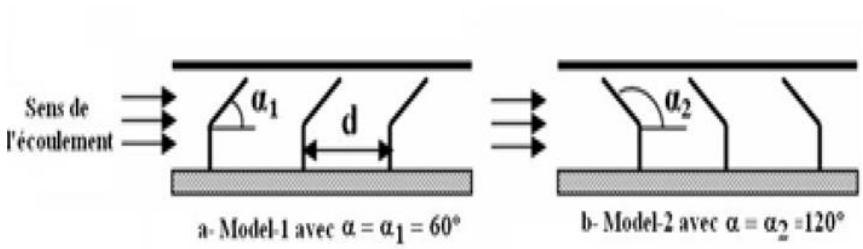

Figure I.31 Descriptive diagram of baffles [36].

It was established that the addition of these kinds of baffles in the duct of fluid allows more heat transfer, where the best efficiency of this SAC recorded in the studied cases is for configuration B, model of baffles 1 (Table I.3).

Table I.3 Experimental results.

Conf.	Temps(h)	$I_G(W/m^2)$	$T_a(°C)$	$T_{fe}(°C)$	$T_{fs}(°C)$	$(T_{fe}-T_{fs})/I_G$	η(%)
A1	11h40	738	28	36	55	0.0108	56.06
A2	10h30	746	24.5	34	54	0.0127	55.67
B2	11h30	743	23	34	50	0.0148	55.11
B1	11h50	739	31	35	66	0.0054	57.80

Through an experimental study, Moummi et al., [37] created a turbulent flow inside a SAC with rectangular baffles perpendicular to the flow direction, this was done in good weather conditions in Biskra, Algeria (Fig I.32).

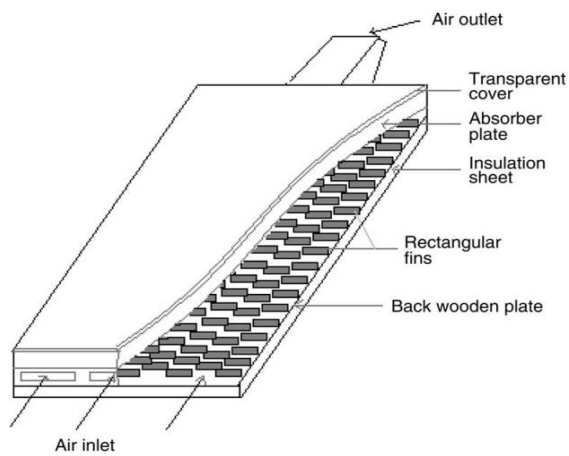

Figure I.32 SAC with the finned system [37].

By a comparison between this type of SAC and that without baffles, also by using two kind of absorber plates, selective and non-selective; they found that the selectivity of the absorber does not present a remarkable enhancement in the presence of baffles (Fig I.33). They also gave an imprecise approach for the calculation of the convective heat transfer coefficient inside the channel, which takes into consideration the nature of the absorber and the type of flow.

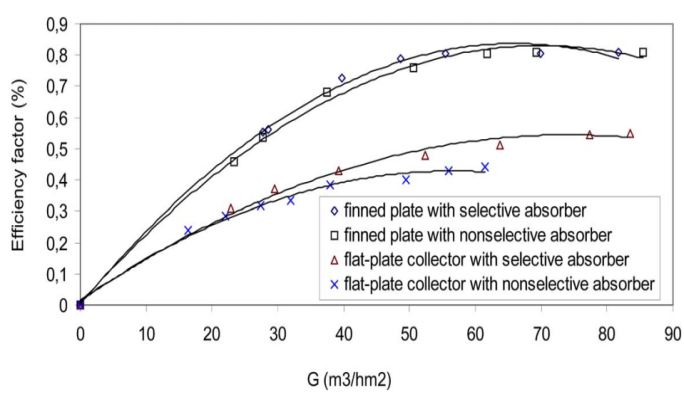

Figure I.33 The efficiency factor of SAC with the air flow for different cases [37].

Esen et al., [38] did an experimental study of a SAC with baffles and with smoothed duct, the aim of this investigation is to increase the heat transfer between the absorber plate and the air by addition the new three geometrical-shaped of baffles with a double channel (Fig I.34). The physical parameters measured are the inlet, outlet and absorber plate temperatures, at different flow rates, and finally, calculate the efficiency.

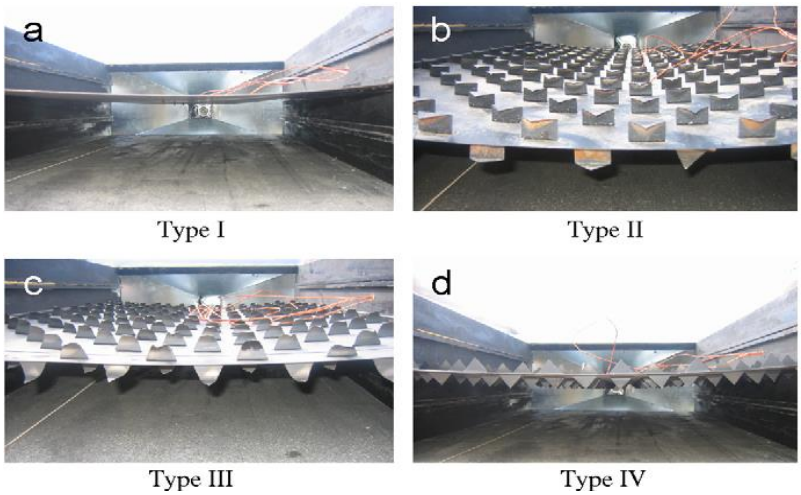

Figure I.34 Types of absorber plates[38].

The results presented that during all conditions the efficiency of the SAC with baffles was much higher than that with smooth plate.

An experimental and numerical study was conducted by Khanlari et al., [14] to investigate the impact of plus-shaped perforated baffles on the drying applications of SACs (cross-flow heat exchangers). The work was divided into three cases: novel SAC with parallel-pass and double ranges of baffles (PPSCDB), SAC with parallel-pass and single ranges of baffles (PPSCB), and parallel-pass with smooth plate (PPSC) (Fig I.35, 36). The experimental study was carried out at two different air mass flow rates, m=0.011 kg/s, and m=0.009 kg/s. In the numerical investigation, Ansys Fluent 18.2 was employed to evaluate the thermal performance of the collector by solving the governing equations, which include the mass conservation, momentum, and energy equations.

Through the experimental results, it was shown that the best efficiency was equal to η=84.30% in mass flow rate m=0.011 kg/s in PPSCDB and the average efficiency of case of PPSC, case of PPSCB and case of PPSCDB are about these ranges η=62.10% to η=66.32%, η=65.72 to η=69.62%, and η=71.12% to η=75.11%, respectively (Fig I.37).

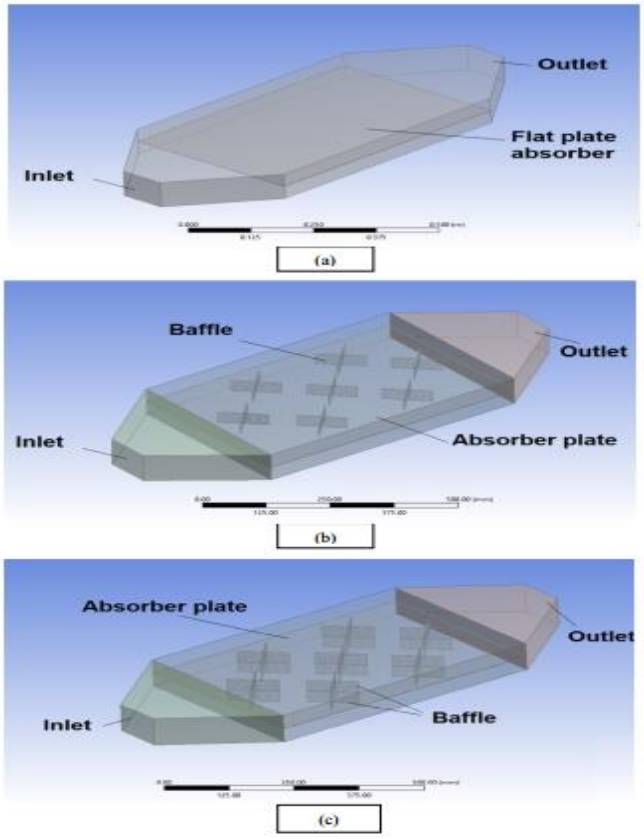

Figure I.35 Geometry of the studied SACs: a) case of PPSC, b) case of PPSCB, c) case of PPSCDB.

Figure I.36 Experimental setup [14].

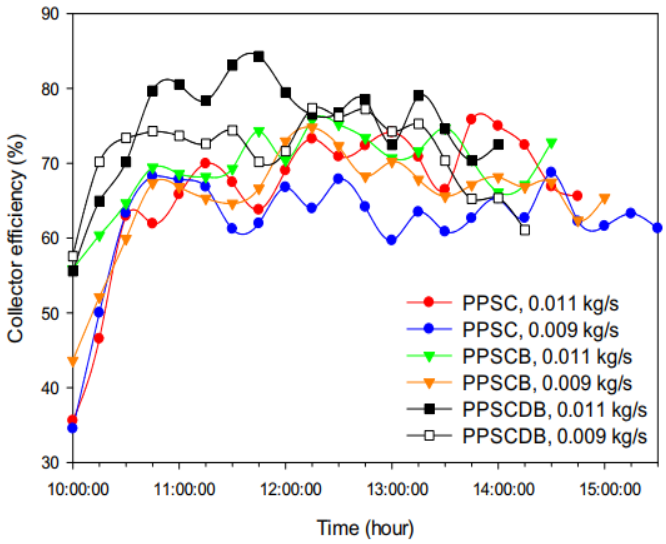

Figure I.37 Variation of thermal efficiency of SAC in terms of time [14].

Through the numerical analysis, the effect of adding perforated plus-shaped baffles on thermal transfer was known in the three types studied, Fig I.38 is an example of this effect in PPSCDB baffles.

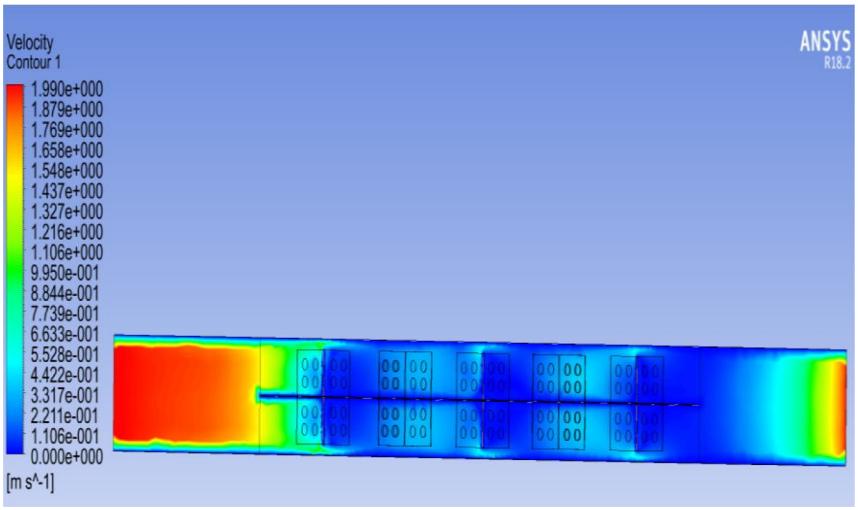

Figure I.38 The temperature distribution in air domain of SAC [14].

Finally, a comparison between the experimental and the numerical analysis of the absorber plate's normal (smooth plate) temperature values, which show that the results are close, where the highest, value of deviation between the two is 9.5% (Fig I.39).

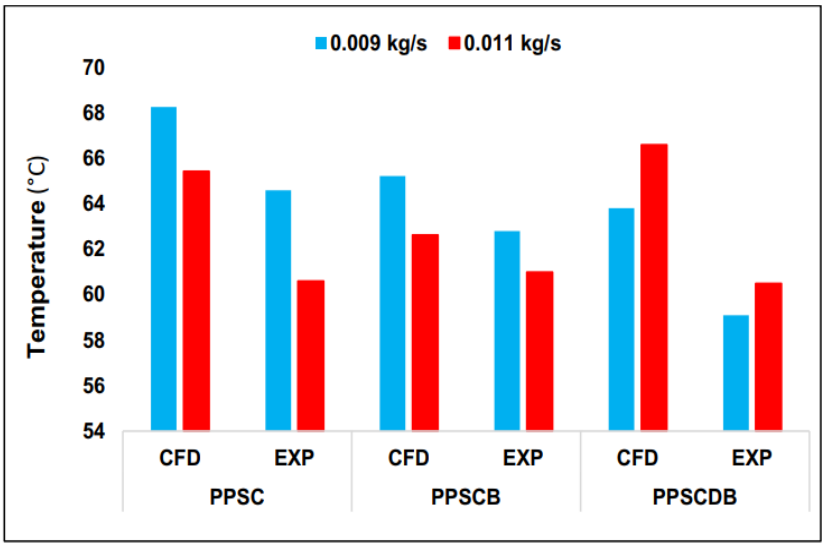

Figure I.39 Absorber plate temperature [14].

Youcef-Ali [39] did an experimentally studied of a SAC; where they added offset rectangular plate baffles, oriented parallel to the airflow, this research was conducted for two types of transparent cover; triple glazing, and double glazing (Fig I.40).

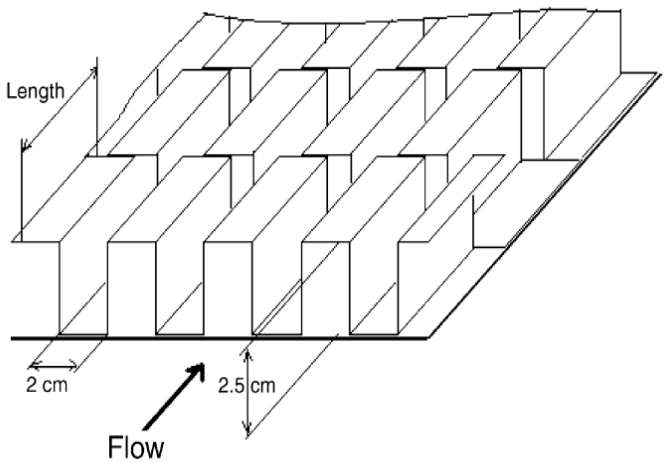

Figure I.40 Offset plate fin absorber plate [39].

This study showed that the triple glazing reduces the heat energy loss more than the double glazing, also adding the offset fins leads to an increase in heat transfer between the air stream and the absorber plate, and that reduces the loss of heat energy. The thermal performance of the triple glazing is better than the double glazing, where gives in the case of offset fins collector, but the amount of radiation decreased for the triple glazing (Fig I.41).

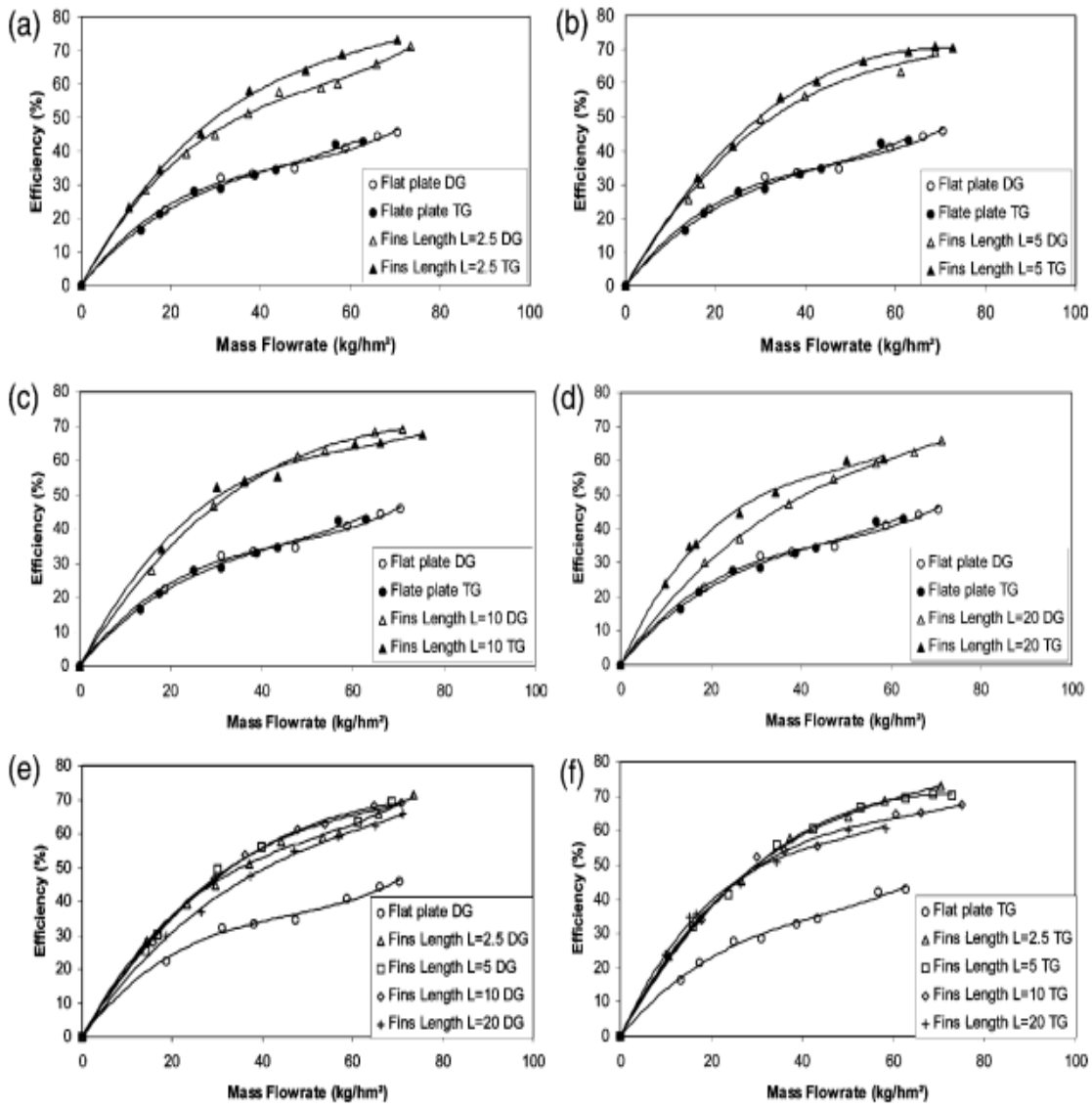

Figure I.41 Thermal efficiency as a function of mass flow rates: G (kg/hm^2), a: offset plate baffles, L = 2:5 cm; b: offset plate baffles, L = 5 cm; c: offset plate baffles, L = 10 cm; d: offset plate baffles, L =20 cm; e: double glazing, f: triple glazing [39].

I.5 Effect of the baffles on flow and thermal fields

Ameur et al., [11] performed a numerical simulation of a SAC with inclination baffles (Fig I.42), and note the flow and thermal field's heat exchange.

The results indicated that the greater heat transfer areas are the near of walls zones; also the study showed that the straight baffles produce the largest recirculation zones compared with the inclined baffle. The opposite direction of the inclined baffle is the best heat transfer (Fig I.43).

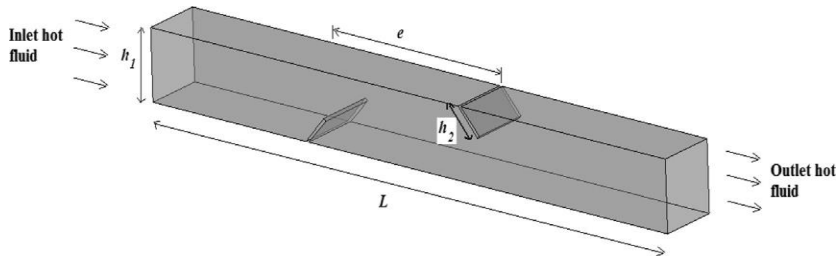

Figure I.42 Geometry of the computational domain [11].

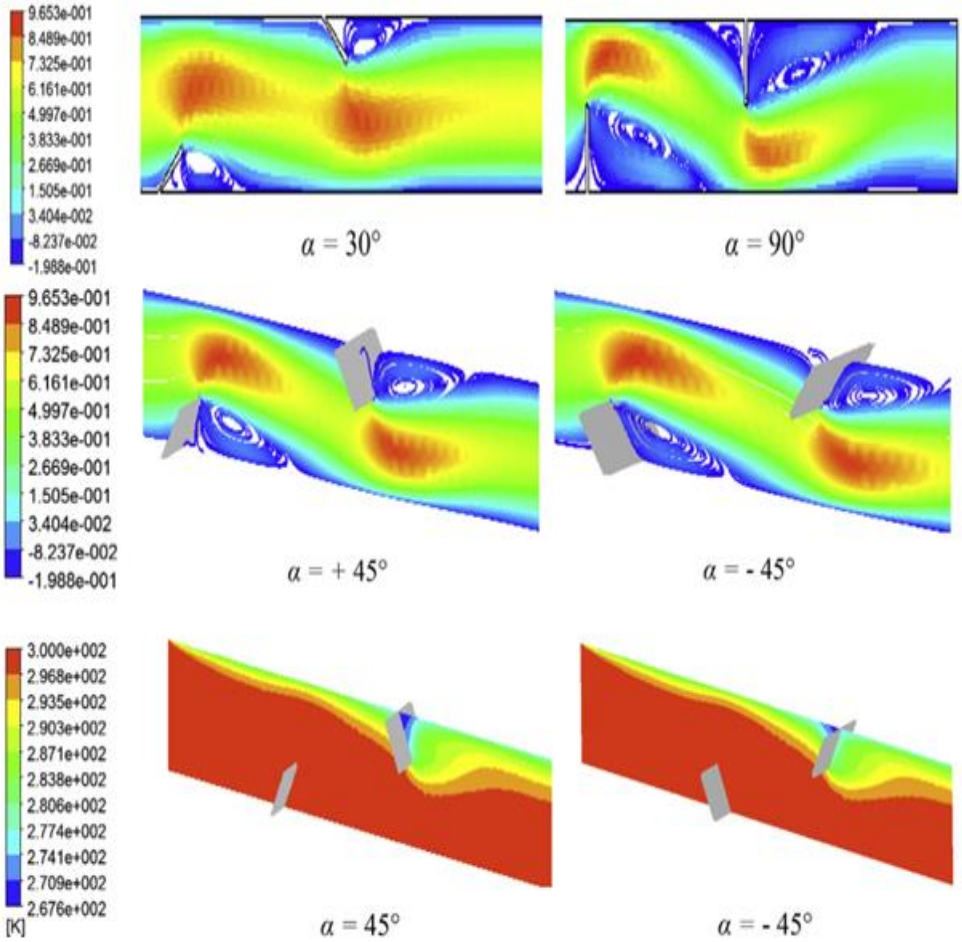

Figure I.43 Thermal fields for Re =100 [11].

Aouissi et al [8] did an experimental and numerical study of heat transfer by forced convection inside a channel containing the baffles of a solar collector. The study chose the shape of the baffles as an important factor to improve heat exchange, which has a rectangular shape and is transversal with air flowing at an angle of inclination β = 90 degrees. The study was conducted at different mass flow rates and different times of the day, to find out the effect of these conditions on the convective heat transfer from the absorber plate to the air through the channel of the collector.

I.6 Influence of the absorber geometry

Mahboub et al. [40] had been created a design that features a slightly curved channel with a smooth flow and a convex-shaped absorber plate (Fig I.44). A prototype of a SAC with a collector area of 1.28 square meters was constructed and tested in summer conditions in Biskra, Algeria. The performance of the heater was measured based on its thermal and effective efficiency using different mass flow rates. Results show that the overall efficiency of this SAC is significantly better compared to the efficiency range of conventional flat plate heaters with a smooth surface; that was previously reported in the literature for similar operating conditions.

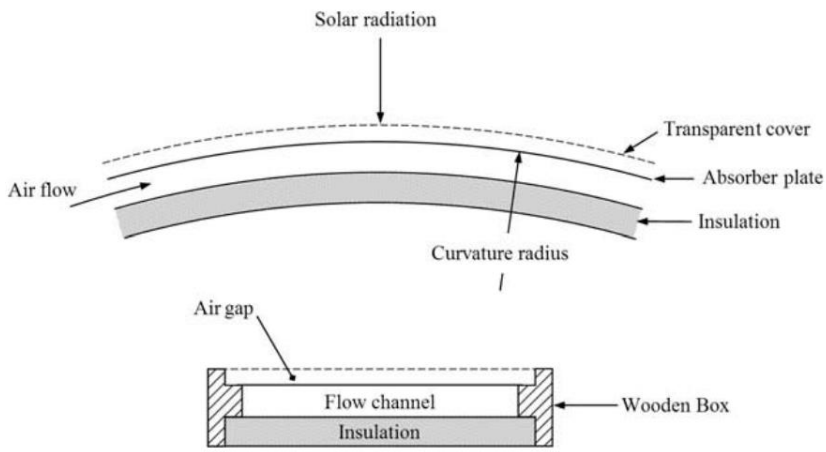

Figure I.44 A cross-section of the curved solar air collector [40].

Ural et al., [41] showed an experimental study on a novel SAC (cross-flow heat exchanger) design that incorporates a textile fabric (Fig I.45). The study involved a comparison between the performance of this new collector, and that of a flat plate SAC, where in the new design, the airflow passes through a textile fabric. The experiments were conducted under identical conditions, and in the same environment for both SACs.

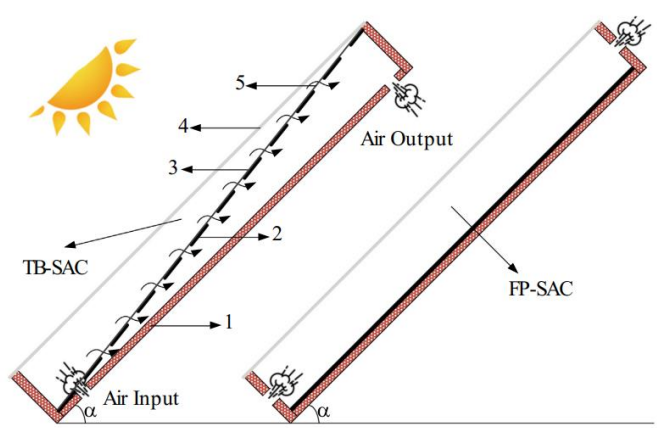

Figure I.45 Schematic view of the textile-based SAC, and the smooth plate SAC (FP-SAC). 1: SAC outer body, 2: Textile fabric support, 3:Textile fabric, 4:Transparent top cover, 5:Air inlet-outlet to the textile fabric [41].

The results of this experimental study showed that the oblique position of textile fabrics gives better performance (energy) (Fig I.46), it has also been noted that this new collector increased the pressure losses but the energy destruction of this collector stays less than the flat plate one, this is because of the outlet air temperature is bigger compared to the other.

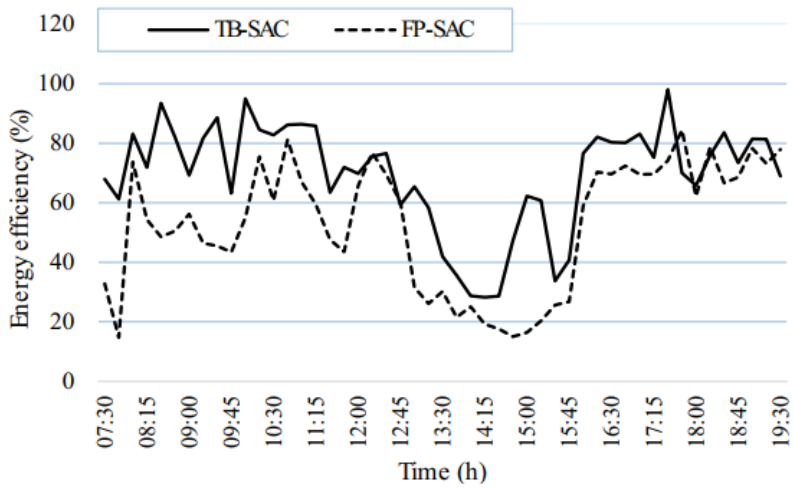

Figure I.46 Change in the energy efficiency of the TB-SAC and FP-SAC [41].

Fiuk et al., [42] carried out an experimental study on SACs with two forms of wavelike absorber surfaces in the natural convection regime. The experiment was conducted under artificial radiation conditions (Fig I.47). The SAC's absorber consisted of three aluminum panels with wavelike shapes, where the situation of these forms is a different figure.

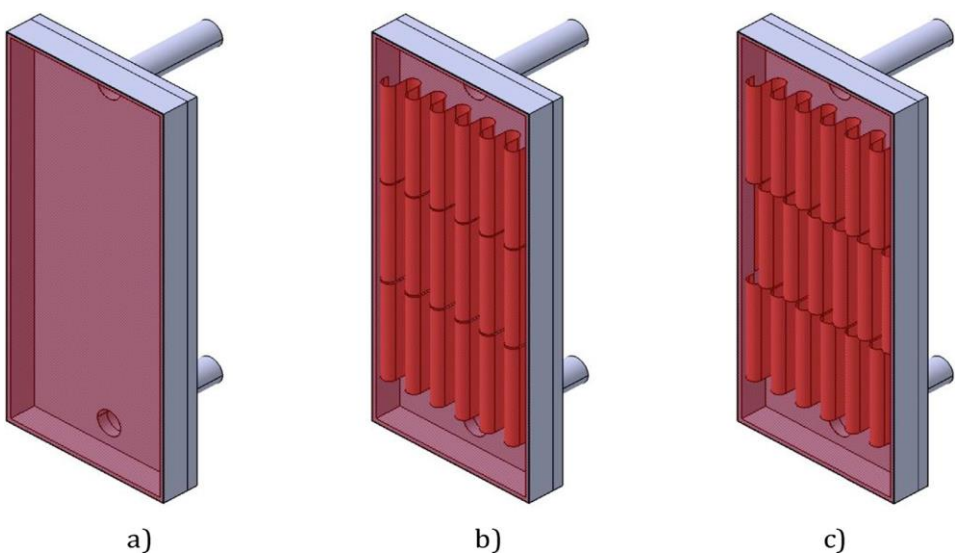

Figure I47. Visualization of tested SACs; (a) "Flat Baseline" design; (b) first novel design "Wave-shaped Type I"; (c) second novel design "Wave-shaped Type II [42].

The results of this work confirmed that the SAC with wavelike baffles Type I has a good thermal performances than Type II (Fig I.48).

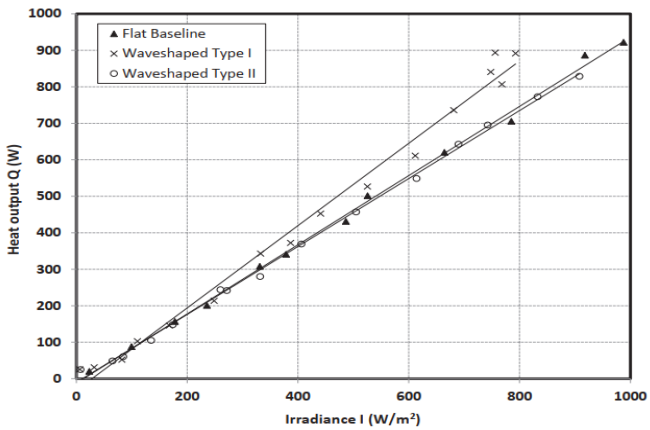

Figure I.48 Collector heat output, Q, vs. irradiance I[42]**.**

Also, the study showed that wave-shaped Type I has the larger thermal efficiency for higher thermal rise values (T_{out} - T_{amb})/I (Fig I.49).

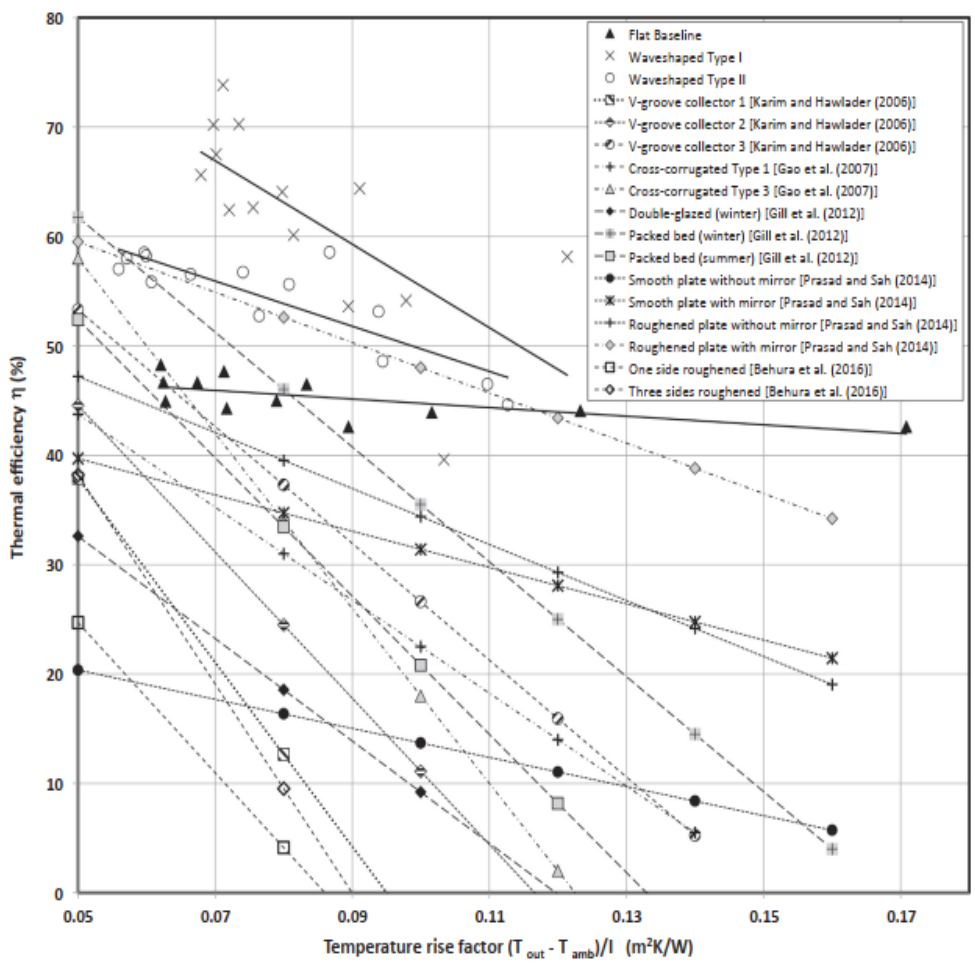

Figure I.49 Comparison of the thermal efficiency η, of SACs versus the temperature rise (Tout - Tamb)/I [42].

I.7 Influence of passage geometry of SACs with baffles

Double-pass air collectors can be classified according to the direction of flow. Several researchers have carried out theoretical studies aimed to improve the thermal performance of double-pass air SACs using different techniques: increasing the heat exchange surface by using baffles, using porous media, and using corrugated absorber plates [43].

Yeh et al., [44] presented a theoretical analysis for a Solar Air Collector (SAC) that uses rectangular baffle shapes for internal-recycle operation. The channel containing the SAC's absorber plate has a width B, length L, and height H. To enhance the SAC's performance, an insulated plate is installed in the duct, dividing the channel into two sub-channels with equal dimensions, namely sub-channels 1 and 2. To promote fluid circulation, a pump is installed to recycle the fluid's movement inside the channel, moving it from the exit of sub-channel 1 to the entrance of sub-channel 2, as shown in Fig I.50.

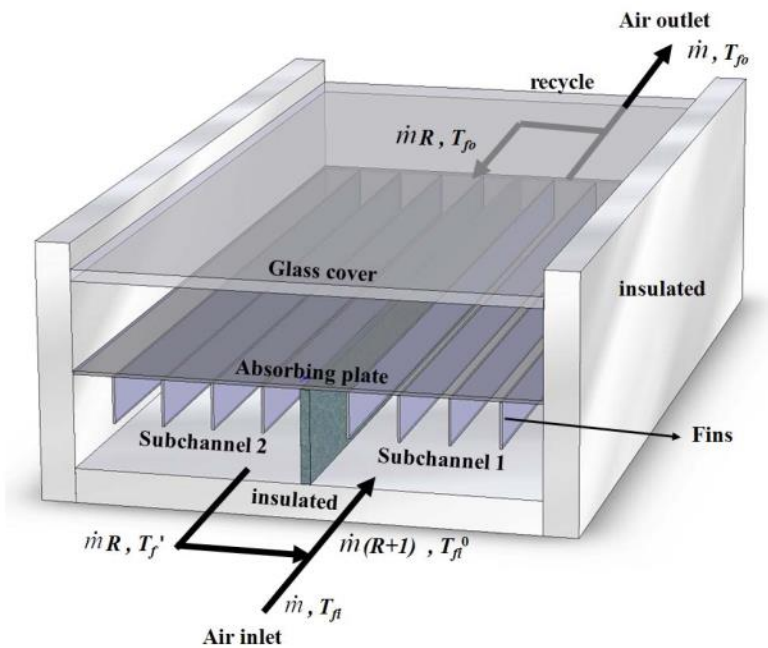

Figure I.50 Downward-type SAC, with an internal recycle and baffles attached [44].

The study report revealed that the recycling operation resulted a better thermal efficiency of the collector with two sub-channels, in both cases, with and without fins.

The SAC efficiency *E* depends on the mass flow rates (Fig I.51), and the reflux ratio, where the collector efficiency increases with the increase in the reflux ratio R for small flow rate values because of the increase in the fluid velocity also causes of decrease in the driving force for thermal energy transmission due to the remixing at the inlet Table I.4.

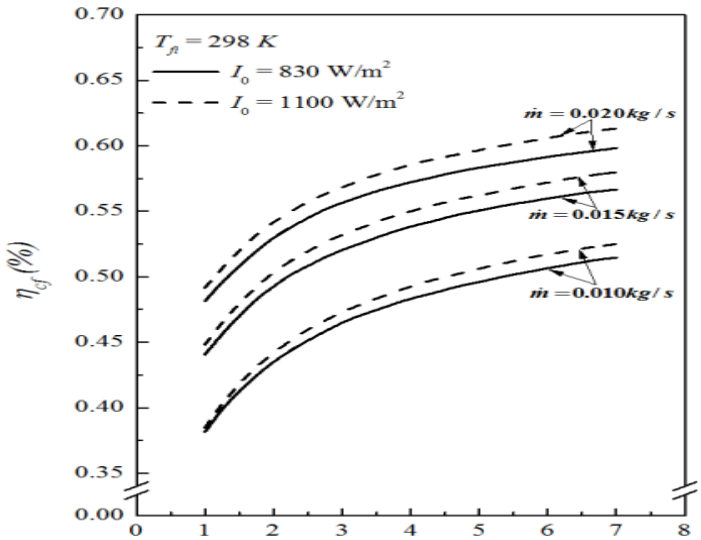

Figure I.51 Collector efficiency (T_{fi} =298K) [44].

Table I.4 Further enhancement of performance for: (a) I_0 =830 W/m^2.

T $_f$(K)	*m* (Kg/s)	*E (%)*			
		R=1	***R=3***	***R=5***	***R=7***
288	0.01	49.27	22.73	20.33	12.58
	0.015	48.84	21.53	14.72	11.15
	0.02	48.12	20.41	13.46	10.85
293	0.01	50.78	23.04	16.97	13.45
	0.015	50.22	22.47	15.55	11.93
	0.02	49.82	21.41	14.39	10.76
298	0.01	52.17	24.69	17.82	14.25
	0.015	51.68	23.99	16.41	12.74
	0.02	51.24	22.33	15.23	11.58

Naphon et al [45] presented a numerical study of the heat transfer performances, the mathematical model used to study the effects of mass flow rates on the performance of SACs with double pass and single pass (Fig I.52).

The models were solved using the explicit finite difference method, and it was observed that employing the double pass yielded superior results compared to the single pass, within the identical range of operating and design parameters (Fig I.53).

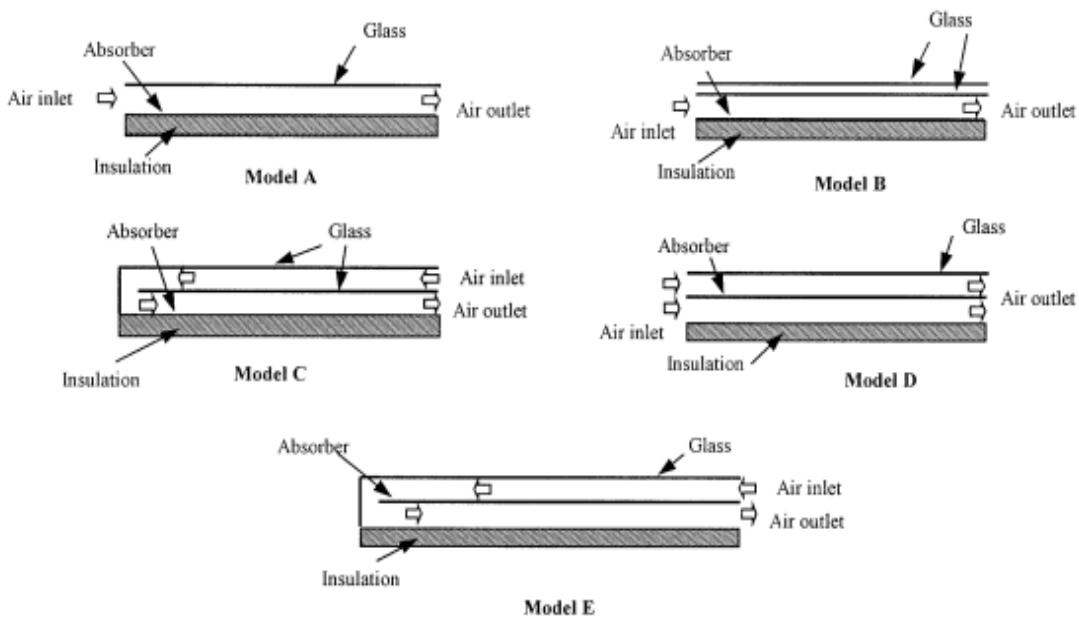

Figure I.52 Schematic diagram of SAC [45].

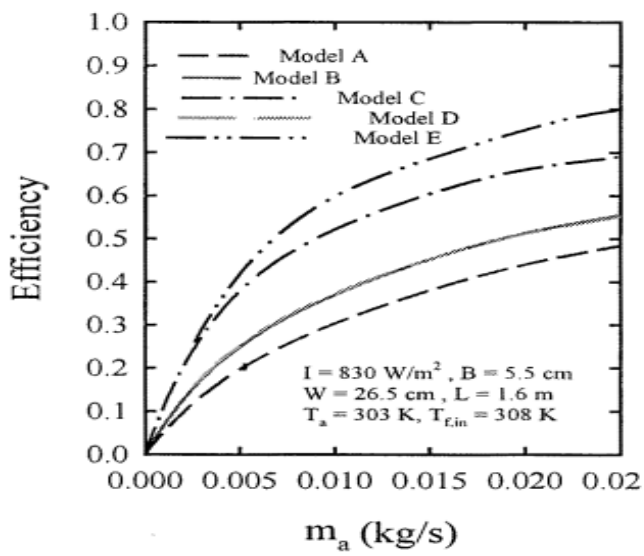

Figure I.53 Efficiency of solar air heater obtained from each model[45].

Sopian et al [46] did an experimental study of a double-pass SAC with porous media inside the duct under the absorber plate (between the absorber plate and the insulation), as shown in Fig I.54. The study enabled a significant relationship between the collector design and the operating conditions.

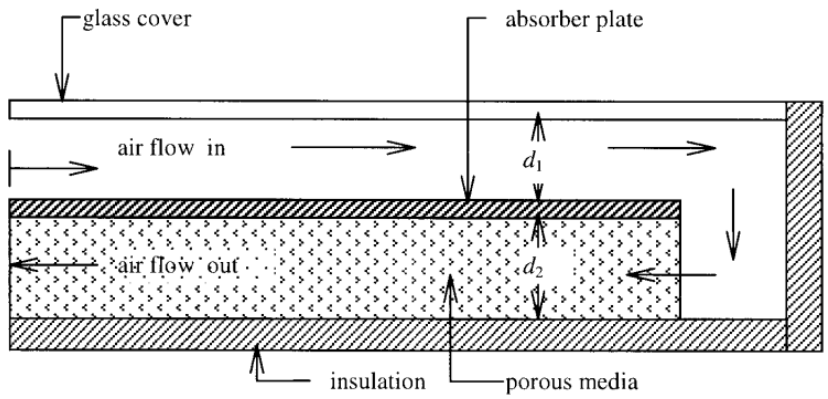

Figure I.54 A diagram illustrating a SAC with a double-pass configuration is shown, where the second channel incorporates porous media. [46].

The research was about the influence of the height of the upper and lower canals, mass flow rates, the effects of solar radiation (Fig I.55), and the temperature rises on the thermal efficiency of this SAC with, and without porous media. The addition of porous media increases the heat transfer area, where leads increase in the temperature of the outlet, which causes to improvement in the thermal efficiency, this kind of collector is considered better than its counterpart single-pass in thermal performance.

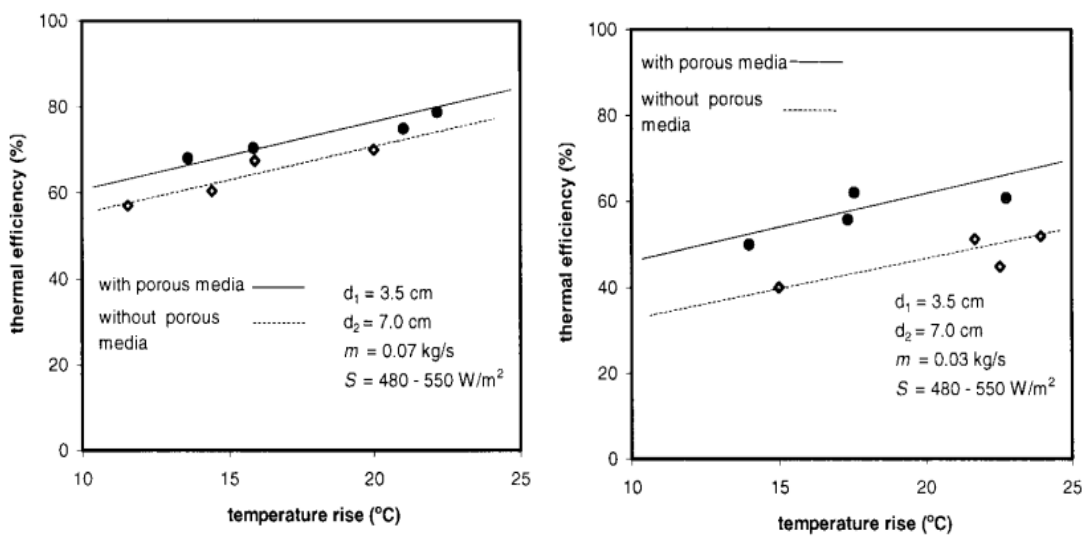

Figure I.55 The thermal efficiency of the double-pass SAC relation to the temperature rise, revealing its impact on the system's performance. [46].

El-Sebaii et al., [47] conducted an experimental and numerical study on a double-pass SAC with tow cases; flat, and V-corrugated absorber plate as we see in Fig I.56, 57 . The study involved comparing the theoretical results with the experimental investigation results. In this

work the outlet temperature, overall heat losses, and output power were compared between the smooth plate SAC and V-corrugated of absorber.

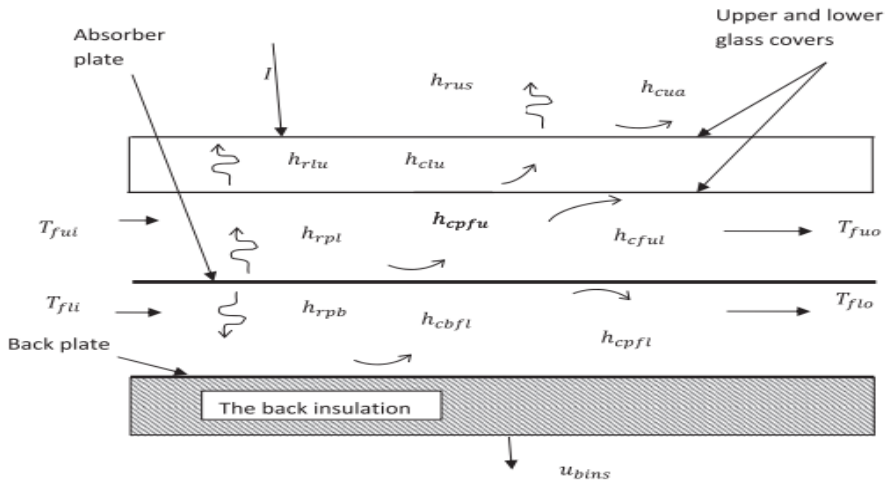

Figure I.56 Double pass flat plate SAC (DPFPSAH) [47].

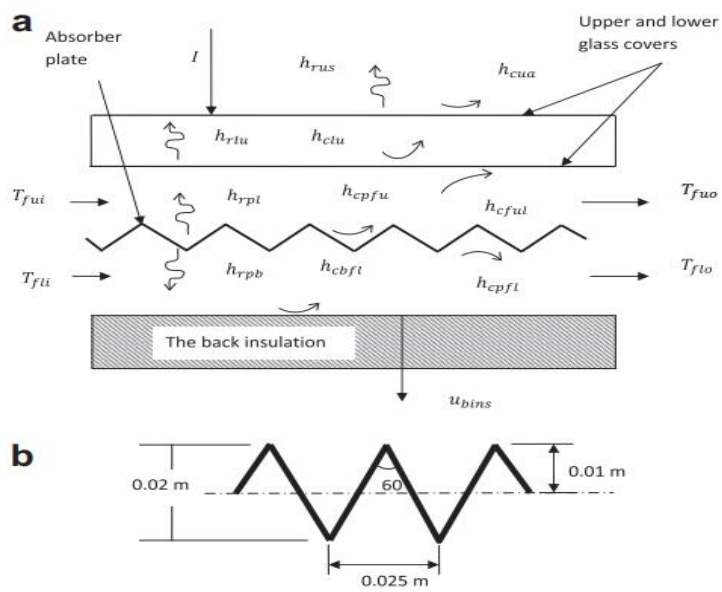

Figure I.57 (a) double pass v-corrugated plate SAC, abbreviated as DPVCPSAH. (b) A section of the v-corrugated absorber plate [47].

Fig I.58 presented the effect of these actions where indicated that the double-pass SAC with V-corrugated absorber plate is better than the collector with flat plate absorber in the thermal efficiency, and the outlet air temperature, also the study showed that the thermal efficiency increase with increasing the mass follow rates.

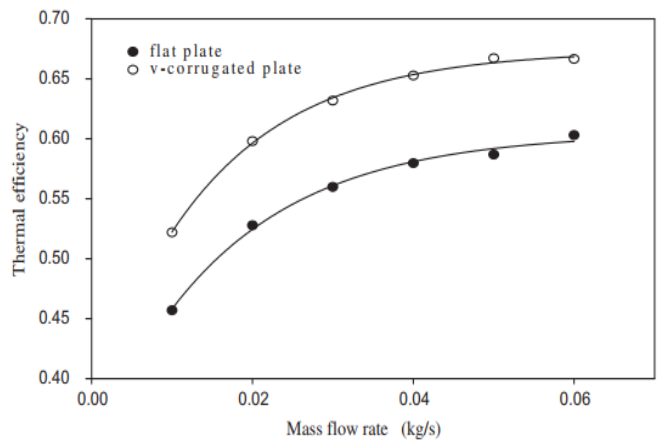

Figure I.58 The effect of flow rates on the thermal efficiency of the double pass flat (DPFPSAH), and v-corrugated (DPVCPSAH) plate SAC [47].

Thakur et al., [48] also changed the shape of the absorber plate through numerical work, where they studied the effect of the new shape on the thermal and hydraulic performance.

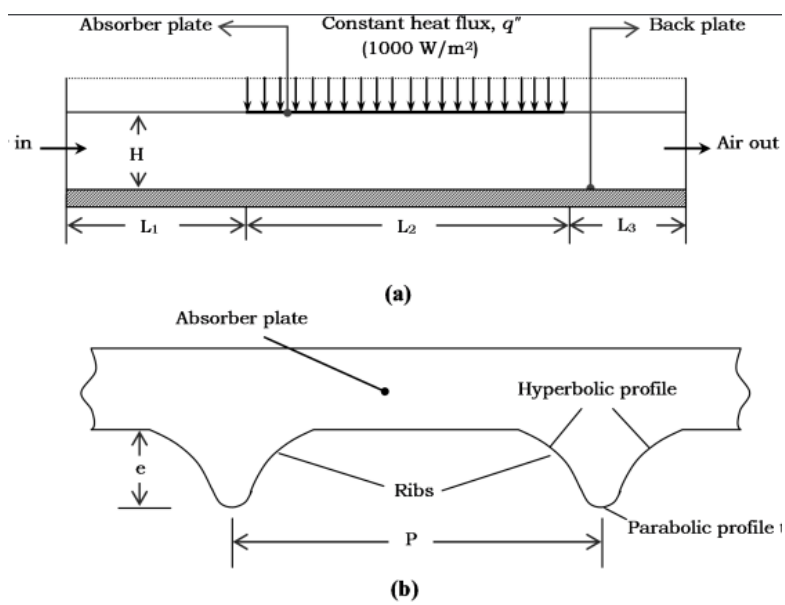

.**Figure I.59** The geometry of the new absorber plate.

Hernández et al., [49] carried out a theoretical and experimental studies on a double-pass SAC with a porous matrix placed in the second channel (between the absorber plate and insulation, to enhance thermal transfer between the absorber plate and air (see Fig I.60). The study involved developing a system of time-dependent equations using balanced energy equations in a separate volume, these equations were solved using the Gauss-Sidel method.

The relative error was relatively small between theoretical results and measured results, for the output temperature was 3% , the digital simulation showed that the internal heat

distribution of the SAC with the porous matrix is better than the SAC without the porous matrix, because this technology increases the thermal transfer between the air and the absorber plate, also the results showed that in the same operating conditions the thermal efficiency of SAC with the porous matrix is 20% larger than the same collector without porous matrix for the porosity of the porous matrix ε = 90%.

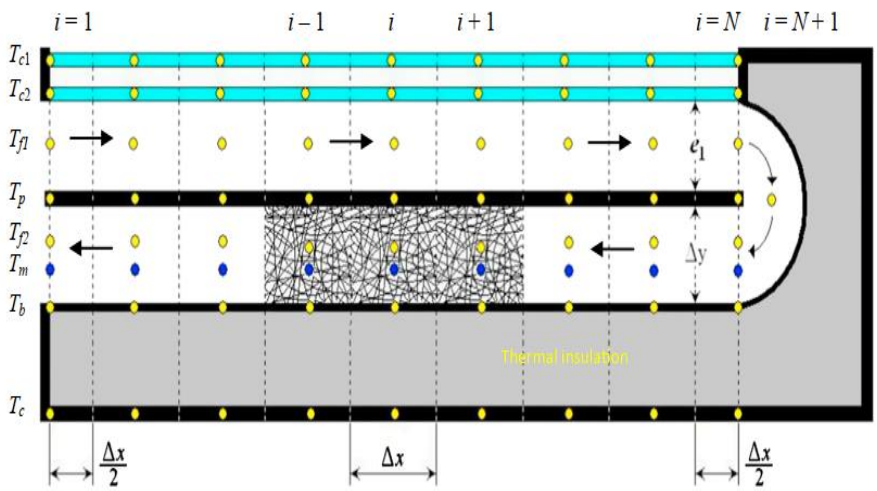

Figure I.60 Discretization scheme of the calculation domain [49].

Jha et al., [50] et al did a theoretical study of a double pass SAC for house air conditioning applications, which predicts a temperature rise of 3° to 7° based on a mathematical model of parallel mode heat transfer. In the same objective of the study, which is to improve the heat transfer between the air and the absorber plate, Tyagi et al., [51] experimentally studied the passage of the air above and below the absorber plate, where they got a significant thermal improvement through the duplication of the channel, as shown in Fig I.61.

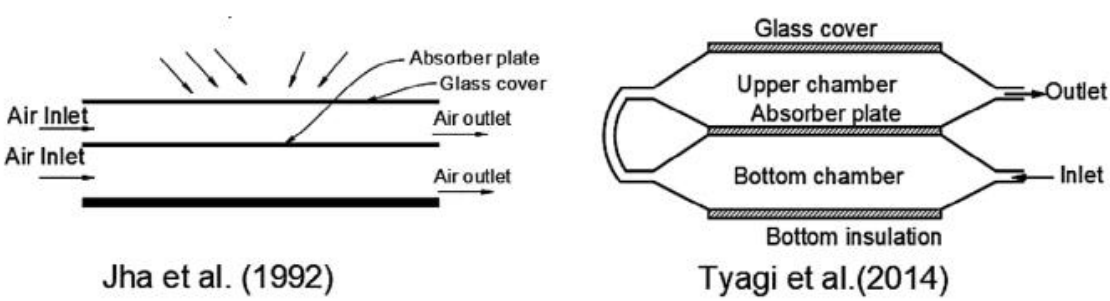

Figure I.61 Jha et al and Tyagi et al ducts [34, 50, 51].

Ho et al., [52] did an experimental and theoretical study, this work presented a study of a SAC with divided its channel into two sections, the two sub channels are with fins, and these fins installed by baffles have been created external recycling. This research aims to increase the thermal transfer between the air and the absorber plate, by using the technique of recycling (Fig

I.62). The theoretical and experimental results for this collector are compared with the results of a single-pass SAC without recycling. A significant improvement in thermal transfer due to the addition of baffles and fins, where the study suggested good operating conditions for these kind of collectors, and the technique of external recycling to improve the collector efficiency.

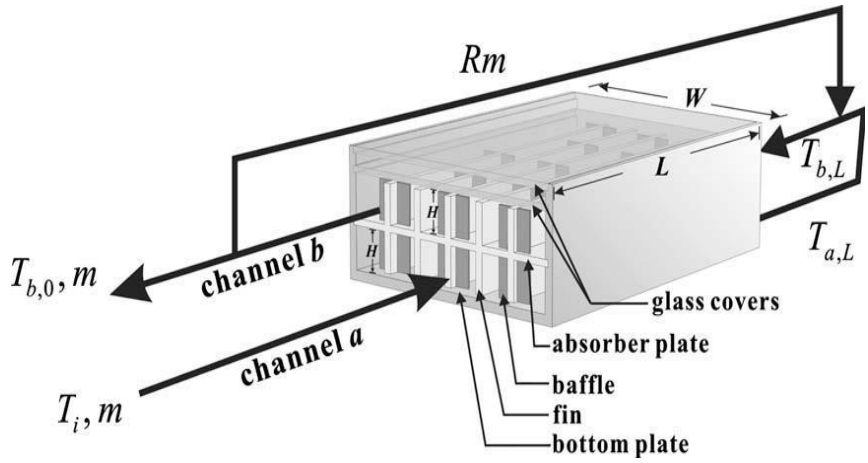

Figure I.62 baffled SAC with internal obstacles attached, and external recycle [52].

I.8 Conclusion

The findings of this chapter indicate that a majority of the researchers in the field of solar energy have focused their studies on SACs that are equipped with baffles. These collectors are designed to utilize air as the fluid medium, and the primary aim of the researchers has been to improve the thermal and hydraulic efficiency of the collectors.

To achieve this goal, the researchers have conducted experiments to modify various aspects of the SAC, including its geometrical characteristics, operating conditions, and the type of channels used. The geometrical modifications have included changes to the number, shapes, and positions of baffles, which play a crucial role in improving the performance of the collector.

Overall, the results of these studies have shown that there is still significant room for improvement in the design of SACs with baffles, and researchers are constantly working to find new ways to optimize their performance. By doing so, they aim to make solar energy an even more viable source of renewable energy and contribute to the global effort towards a greener future.

Chapter II

II. Experimental study of the SAC with baffles

II.1 Introduction

In this section of the study, an experimental investigation was carried out to analyze the performance of the SAC in detail. While many previous researchers have focused only on the thermal aspect of the collector, this study took a more comprehensive approach by considering both the thermal and hydraulic performances.

The series of experiments were conducted at Biskra University, Algeria, and involved a thorough analysis of the components of the SAC, both with and without baffles. The technical specifications, geographical location, and working mechanism of the collector were studied in detail, providing a clear understanding of how the collector functions.

In addition to studying the collector itself, the study also examined the instruments used to measure the various properties of the SAC. These measuring devices were available in the technological laboratory, and all the parts of the collector were locally manufactured. This comprehensive investigation aimed to gain a better understanding of the functioning of the SAC and to identify areas where improvements could be made.

II.2 The global solar irradiation

Through meticulous experimental measurements of solar radiation data across all months, we conducted a comprehensive analysis using an analytical approach. The primary objective of this analysis was to establish a mathematical equation that captures the relationship between each month and the angle of solar altitude while considering relevant constants and global solar radiation. This endeavour aimed to deepen our understanding of the intricate patterns and influential factors that shape solar radiation throughout the year, encompassing the distinct seasons of winter, summer, spring, and autumn.

By scrutinizing the collected data and employing rigorous analytical techniques, we sought to uncover the underlying relationships and dependencies between solar radiation, the angle of solar altitude, and the varying characteristics exhibited by each month.

The insights gained from this analysis enable us to discern the specific influences and patterns associated with each season. We can better comprehend how factors such as the Earth's tilt, solar declination, atmospheric conditions, and other variables impact the amount and distribution of solar radiation during winter, summer, spring, and autumn.

The establishment of the mathematical equation linking the months, solar altitude angles, constants, and global solar radiation provides a valuable tool for future research and practical applications. It facilitates accurate predictions and assessments of solar radiation levels throughout the year, enabling informed decision-making in various fields such as renewable energy planning, agriculture, and climate studies[53].

II.2.1 Geographic site

Biskra is positioned at the southern slope of the Aurès massif and is located at the convergence point of two valleys trailing the massif, at the same time, abundant water and fertile soil resources have supported agricultural activities. The city of Biskra spans an area of 21,671.2 km^2 and shares borders with Batna to the north, Msila to the northwest, Khenchela to the northeast, El Oued to the south, and Djelfa to the southwest. Biskra is geographically situated at 34°48' north latitude and 05°44' east longitude Fig II.1 [54].

Figure II.1. Location of the experimental setup in the map (Biskra)

II.2.2 Model of the global solar irradiation

After analyzing the measured results, it was converted into a mathematical model in terms of many characteristics. Finally, we get the non-linear mathematical model that simulates the experimental results, which gives the following:

$$Ray(h)_{\text{horizontal}} = a + \frac{b-a}{\left(1+10^{(c-h)\times d}\right)} \qquad \text{II.1}$$

Where a, b, c, d are constant changes by months, and h is the height sun (The angle between the astronomical horizon and the axis connecting the observed point to the sun). Table 1, 2 shows the change of constants in terms of the change in months.

Table II.1 The constants of the model of global solar irradiation, according to the month from January to June.

Months	January	February	March	April	May	June
a	-3.3205	-5.280	-7.227	-12.30	-18.208	-20.357
b	701.329	820.10	886.46	962.43	986.38	965.33
c	0.36153	0.4317	0.5336	0.614	0.6310	0.6398
d	3.299	2.6913	2.3220	1.994	1.8791	1.8473
R^2	0.9843	0.9717	0.9840	0.9906	0.9970	0.9875

Table II.2 The constants of the model of global solar irradiation, according to the month from July to December.

Months	July	August	September	October	November	December
a	-19.21	-11.446	-9.58401	-6.2274	-3.709	-2.666
b	961.035	858.94	908.052	821.72	692.83	597.57
c	0.62617	0.6108	0.54844	0.4586	0.38247	0.34569
d	1.87613	2.0273	2.20218	2.6067	3.19469	3.61849
R^2	0.9938	0.9924	0.99725	0.9967	0.99334	0.99822

II.2.2.1 ***Variable equations a, b, c, and d***

In the first observation of the constant of the (a) variation with low values by a signal (-), draw the illustration curves against the evolution of the solar radiation. The constant (a) again it's depending on the months of the year when in the month selected values with different, trying to create a mathematical model to predict the constant (a) as a function of the month of the year,

$$a = Y_0 + H \times \exp\left(-0.5\left(\frac{M - M_c}{\omega_1}\right)^2\right) \qquad (M < M_c)$$

$$a = Y_0 + H \times \exp\left(-0.5\left(\frac{M - M_c}{\omega_2}\right)^2\right) \qquad (M \geq M_c) \qquad \text{II.2}$$

Equation (2), shows the variation of (a) as a function of the month of the year with two different ways to calculate or different conditions such as when the $M < M_c$, and $M > M_c$, which depending on confined in the constant ω1, and ω2, see Tab.3.

Table II.3 The constants of the model of equation (2)

Adj. R-Square	Y_0	M_c	H	ω_1	ω_2
0.97348	-3.17265 ± 0.707	5.92 ± 0.22477	-17.249 ± 0.86548	1.74025 ± 0.22324	2.03371 ± 0.23729

$$b = h_0 + \kappa_1 \times \left(\sin\left(\frac{\pi(M - N_c)}{\varepsilon}\right)\right)^2 \qquad \text{II.3}$$

The constant (b), too depends on the month of the year, for this point trying to predict the mathematical model as a function of the month, the illustration curve estimate to sinusoidal function see Eq.(3) and Tab.4.

Table II.4 The constants of the model of equation (3)

Adj. R-Square	h_0	N_c	ε	κ_1
0.93394	-418039.86541	-308.86107	629.5827	419014.40835

$$c = c_0 + \sigma \times \exp\left(\frac{(M - P_c)^2}{2 \times n^2}\right) \qquad \text{II.4}$$

Table II.5 The constants of the model of equation (4)

Adj. R-Square	c_0	P_c	n	σ
0.97618	0.13079	6.16691	4.17233	0.5211

$$d = d_0 + \lambda \times \sin^2\left(\frac{M - F_c}{\rho}\right) \qquad \text{II.5}$$

Table II.6 The constants of the model of equation (5)

Adj. R-Square	d_0	F_c	ρ	λ
0.99046	1.808	6.128	250.879	347.127

Constants (c) and (d) it's the last terms of eq.1, the evolution estimate with two functions first exponential, see eq.4 and the second sinusoidal square see Eq.5. The adjustment residual square gives a good approximation between the two equation, which means the constants estimated the basic values.

II.2.3 The ultimate mathematical model of solar radiation

After completing the variable constants tables (a, b, c, d), We substitute these variables into the final mathematical model for all months, which takes the following form:

$$Ray(h)_{\text{horizontal}} = Y_0 + H \times \exp\left(-0.5\left(\frac{M - M_c}{\omega_1}\right)^2\right) + \frac{h_0 + \kappa_1 \times \left(\sin\left(\frac{\pi(M - N_c)}{\varepsilon}\right)\right)^2 - Y_0 + H \times \exp\left(-0.5\left(\frac{M - M_c}{\omega_1}\right)^2\right)}{\left(1 + 10^{\left(c_0 + \sigma \times \exp\left(\frac{(M - P_c)^2}{2 \times n^2}\right) - h\right) \times d_0 + \lambda \times \sin^2\left(\frac{M - F_c}{\rho}\right)}\right)}; \quad (M < M_c) \qquad \text{II.6}$$

$$Ray(h)_{\text{horizontal}} = Y_0 + H \times \exp\left(-0.5\left(\frac{M - M_c}{\omega_2}\right)^2\right) + \frac{h_0 + \kappa_1 \times \left(\sin\left(\frac{\pi(M - N_c)}{\varepsilon}\right)\right)^2 - Y_0 + H \times \exp\left(-0.5\left(\frac{M - M_c}{\omega_2}\right)^2\right)}{\left(1 + 10^{\left(c_0 + \sigma \times \exp\left(\frac{(M - P_c)^2}{2 \times n^2}\right) - h\right) \times d_0 + \lambda \times \sin^2\left(\frac{M - F_c}{\rho}\right)}\right)}; \quad (M \geq M_c) \qquad \text{II.7}$$

II.3 Experimental design

In this work, a single-channel SAC was tested, as shown in Fig II.2, with an inclination angle of 38 degrees. The experiments were carried out near the mechanical engineering experimental hall at the Biskra University, Algeria, located in the northeast of the Algerian Sahara. The site has coordinates of 34'.84° longitude, 5'.75° latitude, and an elevation of 108 meters above sea level. The aim of the study was to investigate the effects of the number, angles of inclination, and positioning of rectangular baffles on the SAC's performance. The rectangular baffles were positioned at an angle of inclination 135°, and two other cases, case M and case H[55]). The study focused on investigating an incompressible fluid stream (air) flowing through a rectangular channel of the SAC, as illustrated in Fig II.3, 4. The experiment took under natural atmospheric conditions, utilizing various measurement devices accessible in the laboratory. Key parameters measured during the experiment included inlet and outlet temperatures, mass flow rates, and absorber temperature. To capture data from different regions of the collector's surface, five collectors were employed, as depicted in Fig II.5. Additionally, the temperature of the bottom plate was measured at five points aligned parallel to the absorber plate, as shown in Fig II.5. [13].

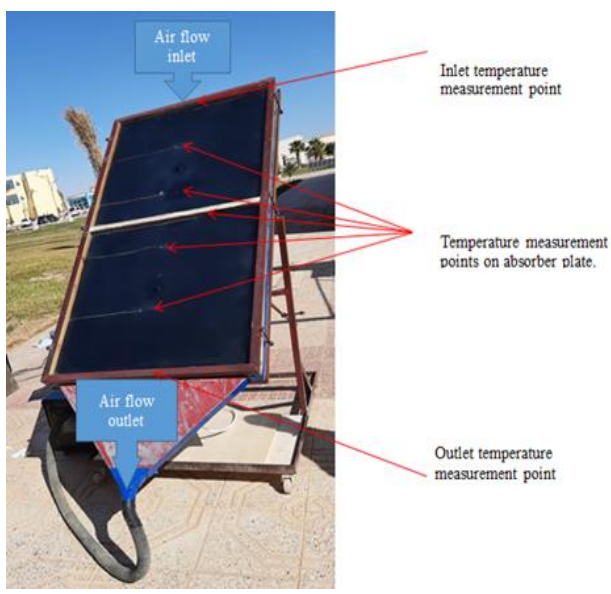

Figure II.2 The solar air collector.

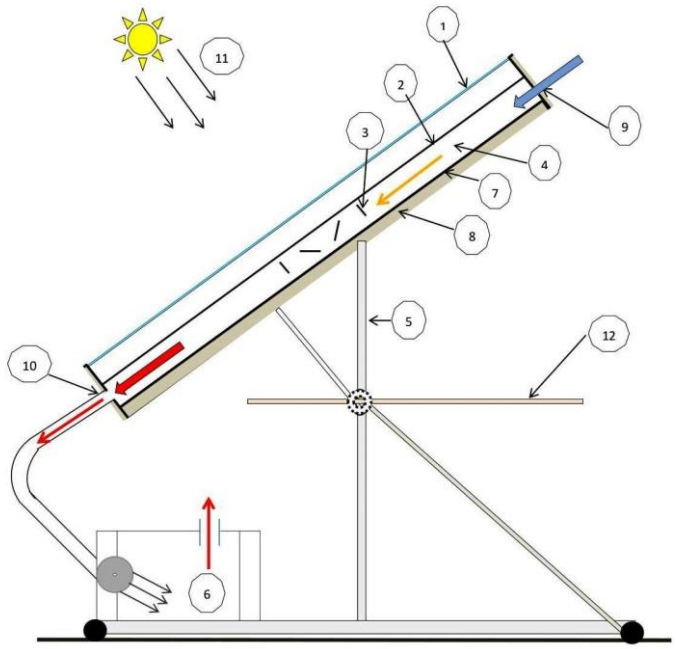

Figure II.3 Schematic diagram of our SAC, (1: transparent cover, 2: absorber plate, 3: baffles, 4: air duct, 5 iron support, 6: aspirator, 7: bottom plate, 8: insulation, 9: inlet airflow, 10: outlet airflow, 11 solar radiation, 12: tool table).

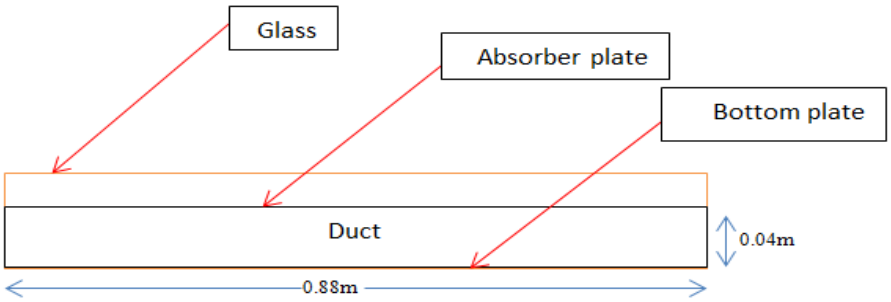

Figure II.4 Cross-section of the smooth plate SAC.

The Solar Air Collector (SAC) in this study was well insulated thermally. The SAC used in this study consisted of multiple layers for protection, including a 2.2 mm galvanic layer, 40 mm polystyrene layer, and 4 mm wood layer. To ensure insulation, wood was used for the sides, and a transparent glass cover was placed on top. The channel was enclosed at the bottom by a galvanic plate and at the top by a galvanic heat absorber coated with a non-reflective layer to minimize radiation. The dimensions of the SAC employed in this investigation are provided in Table II.7.

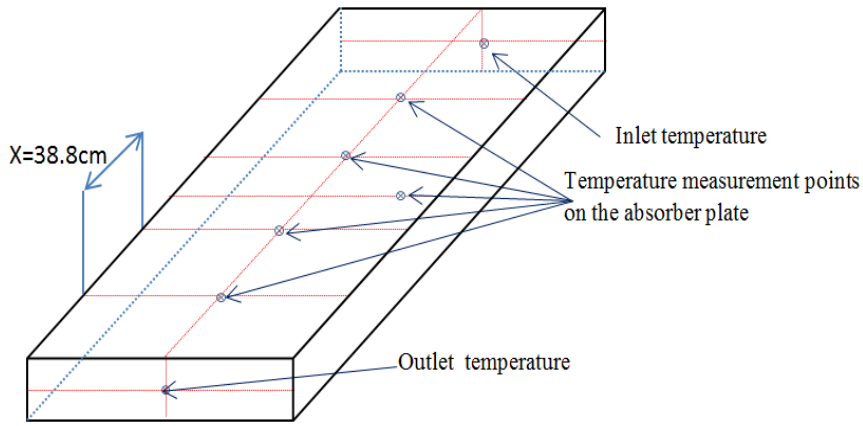

Figure II.5 Temperature measurement points.

Table II.7 the dimensions of the SAC's elements.

The elements	Length (m)	Width (m)	Thickness (mm)
Transparent cover	1.88	0.88	**3**
Absorber	1.88	0.88	**0.8**
Polystyrene	2	1	**40**
Baffles	0.88	0.02	**0.8**

Table III.8 provides a summary of all thermo-physical properties of the materials used, the table also includes essential parameters such as thermal conductivity, specific heat, and density.

Table II.8 Thermo-physical characteristics of the elements.

Materials	Density(ρ) [kg/m^3]	Specific heat (C_P)[J/kg.K]	Thermal conductivity (λ) [W/m.K]
Glass	1.2	1500	**1.5**
Galvanized steel	7800	473	**45**
Polystyrene	16	1670	**0.037**
Wood	1500	1200	**0.15**
Air	1.167	1006	**0.0262**

II.3.1 Technical characteristics of the uses baffles

In this work, the baffles used were produced locally at the technological laboratory of Biskra University, as shown in Fig II.6. They were rectangular shaped galvanic plates that measured 20 mm wide and 880 mm long. These plates were fixed to wooden borders, leaving two spaces below and above the baffles for air to flow through, as depicted in Fig II.7.

Figure II.6 The rectangular shape of the baffles.

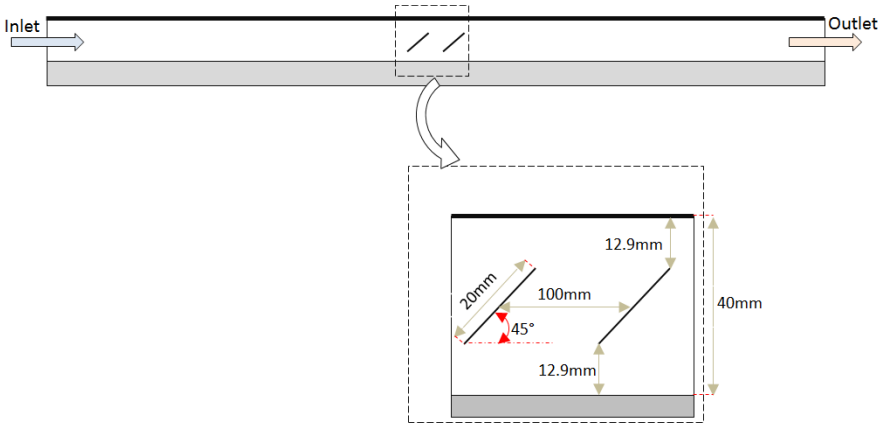

Figure II.7 Cross section of the channel showing the position of baffles.

II.3.2 Uses devises

In this work, several modern digital devices were used to measure all quantities and move the air inside the channel. Fig II. 8 shows the various devices employed.

Figure II.8 Used devices, Thermocouple, Aspirator Pyranometer, and airflow pressure device.

II.3.2.1 ***Pyranometer***

Was utilized to measure the solar radiation [W/m^2]; where the portable type was used.

II.3.2.2 ***Thermocouple***

A temperature measurement device was utilized to monitor the temperature at different locations within the collector. The device employed a conveyor thread, comprising a pickup fixed on the target area for measurement and a socket directly connected to the thermocouple. This setup allowed for accurate temperature readings. The readings were easily obtained from the display screen.

II.3.2.3 ***Aspirator***

To facilitate the airflow within the channel, a mechanism was employed to move the air from the entrance to the exit. The mass flow rate was regulated by a flow-adjusting device directly connected to the aspirator, enabling precise control over the airflow.

II.3.3 Uncertainty of the parameters

To measure the temperature at various points of the SAC, a Thermocouple (K-type) device was used Fig II. 8 which has four sockets and uncertainty in measurements $E_{\Delta T}$=±0.2°C, Pyranometer (L2-4890.20) with uncertainty $E_{\Delta I}$=±1W/m^2, also, a flow adjusting device connected directly to the Aspirator was used in order to know the value of the flow, and from it, we can calculate the velocity. In all manual measurements, the reading is done after a while from the initial display of the screen, to prove the value and be more accurate. A mathematical model was planned by Kline et al [56]. The expression for uncertainty for every parameter X as a function of partial parameters y1, y2,.., yn is given by:

$$\omega_x = \left[\left(\frac{\partial X}{\partial y_1} \omega_{Y1} \right)^2 + \left(\frac{\partial X}{\partial y_2} \omega_{Y2} \right)^2 + \ldots + \left(\frac{\partial X}{\partial y_n} \omega_{Yn} \right)^2 \right]^{1/2} \qquad \textbf{II.8.}$$

Table II.9 The uncertainty of the parameters

Device	*Type name*	*Unity*	*Value*
Pyranometer	L2-4890.20	W/m^2	±1W/m^2
Thermocouple	K-Type	C°	±0.1C°
Pressure	Airflow DM 3	Pa	±1Pa
Thermal efficiency	Calculated	/	±0.032
Absorber dimensions	Calculated	m	±0.001m

II.4 Experimentally studied cases

The study conducted measurements for the cases with an angle of inclination B=135° in April, with measurements taken every half hour between 8 am and 4 pm. The measurements obtained included mass flow rates, temperature at five points of the absorber, and bottom plate, as well as inlet and outlet temperatures and solar radiation. Through an experimental work

presented by Chabane et al [57], where it conducted on the placement of rectangular baffles with a 90° angle of inclination inside a channel. The study revealed that mode 2 outperformed modes 1 and 3, when six baffles were placed in the center of the channel. Based on this finding, the middle area was selected for further investigation, along with the baffles that had an inclination angle of 135°. After analyzing the research conducted by Menasria et al., [58] it was determined that the angle of inclination of 135° for the baffles results in less pressure drop for the air passing through. As a result, the middle section of the duct was chosen for a thorough investigation, building upon the findings from prior research. Two obstacles were placed in the center of the duct, and four baffles were added to each case, as depicted in Fig II.10. These scenarios were examined across three mass flow rates, with one flow per day.

During this phase of the experimental investigation, a total of six cases were examined over a period of 18 days. These cases featured identical tilt angles but varied in terms of the number of baffles employed. Measurements were taken for both pressure and temperature differences at specific points within the system. Three different air flow rates were considered: m=0.014 kg/s, m=0.024 kg/s and m=0.032 kg/s for each respective position. For the *B*=135° angle, a total of five cases were studied, in addition to a reference case, resulting in a total of six cases analyzed for this configuration.

The cases studied are as follows:

- Smooth plat case: SAC without baffles.
- Model I (2M135): SAC with 2 baffles in the middle, with an angle of inclination of 135°.
- Model II (6M135): SAC with6 baffles in the middle, with an angle of inclination of 135°.
- Model III (10M135): SAC with10 baffles in the middle, with an angle of inclination of 135°.
- Model IV (14M135): SAC with14 baffles in the middle, with an angle of inclination of 135°.
- Model V (18M135): SAC with18 baffles distributed across all channels with angle of inclination 135°, between each obstacle and the second 10 cm.

The second part of the experimental investigation is studying case M, and case H, where the angles of baffles inclination are 90°, 45°,135°,90°, and 90°,180°,180°,90°, respectively Fig II.9, 11, these experiments were undergone in the natural conditions of this region on the following days: 30/11/2021 and 01/12/2021, where the weather was clear with no wind; the average solar radiation at that time was I=876W/m^2. In the testing case used for comparison, there are four baffles in the middle with different angles of inclination; the various characteristics were then measured under changing operating conditions. The series of measurements was done from 11:30 am to 02:00 pm- where the solar radiation is the highest and almost constant. Each

quarter of an hour, measurements were recorded, ending up with eleven (11) measured cases whose mass flow rate ranged from m=0.011Kg/s to m=0.068Kg/s.

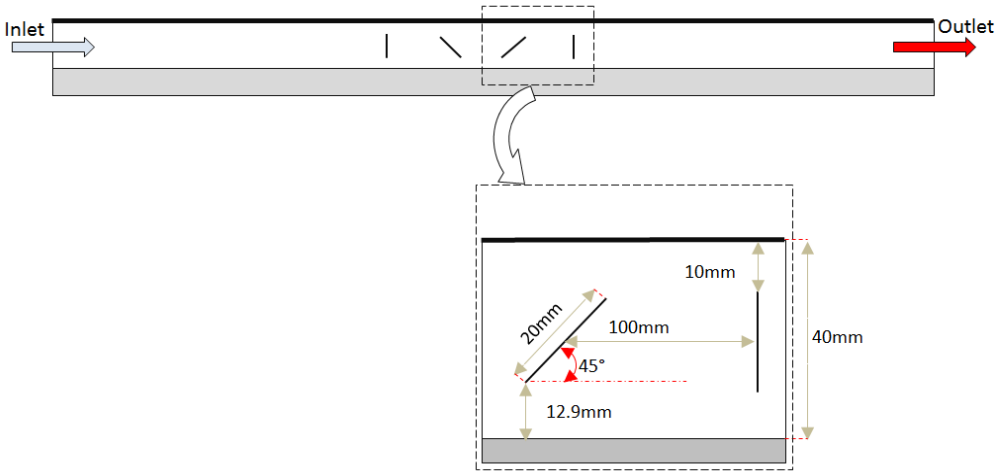

Figure II.9 Dimensions of baffles inside the channel of M cases.

The purpose of conducting these experiments was to enhance the technical efficiency of the SAC by introducing baffles at various positions to generate turbulent flow. This approach aimed to improve the collector's thermal performance while also considering its hydraulic aspect.

Figure II.10 Different cases of the position baffles β =135°.

Figure II.11 Cases M and H

The results of this section present the found and their interpretation after a series of experimental tests. The focus is on efficiency, and fluid outlet temperature to understand the impact of adding baffles with different cases on the hydraulic and thermal performance of SACs.

II.5 Conclusion

This study presents an experimental investigation conducted to examine the heat transfer mechanism within a SAC (Solar Air Collector) channel. The research focused on five distinct cases of β=135°; each featuring varying numbers of baffles while maintaining a consistent angle of inclination, in addition of the two cases M and H. The investigation encompassed both hydraulic and thermal aspects, encompassing parameters such as pressure drop, heat transfer coefficient, thermal efficiency, and other relevant results. The design and installation of the experimental setup took place in the technological lobby of the University of Biskra, utilizing dimensions previously explored and documented in the literature.

Chapter III

III. Numerical study

III.1 Introduction

In this chapter, the numerical results were analyzed, using CFD investigation (Fluent 18.1 software), this part of the study consists of three steps, many cases were examined for the number and position of baffles (6 b, 10 b, 14 b, 18 b, case M, case H) with a fixed inclination angle of 135° for the first four cases in the Reynolds range from Re=5038 to Re=10635, and with another angles and positions for the rest, H (β= 90°, β= 180°, β= 180°, β= 90°), M (β= 90°, β= 135°, β= 45°, β= 90°). This phase of the research involved the utilization of Computational Fluid Dynamics (CFD) using Ansys Fluent 18.1. The RNG k-ε turbulence model was selected due to its ability to produce results that closely aligned with the standard correlations of Dittus-Boelter and Modified Blasius when compared to other models. To validate the accuracy of the CFD simulation, it was compared against the findings from the experimental investigation, taking into account the influence of meshing. This comprehensive analysis ensured the reliability and validity of the CFD simulation results.

III.2 Modeling

The purpose of this study is to comprehensively evaluate the performances of SACs by considering both the hydraulic and thermal aspects. To achieve this goal, the study utilizes both dimensional and no-dimensional parameters to quantify the performance of the collector. One of the most important non-dimensional parameters used in this study is the Reynolds number, which provides a measure of the fluid flow characteristics in the collector.

The Reynolds number (Re) is calculated using the formula (III.1), and helps to analyze the flow regime of the fluid, whether it is laminar or turbulent, and the influence of various parameters such as fluid velocity, density, and viscosity on the flow. This information is crucial in determining the efficiency of the collector, as the flow regime can have a significant impact on the thermal and hydraulic performances of the collector.

$$\boldsymbol{Re = \frac{UD_H}{\vartheta}} \qquad \text{III. 1}$$

Where D_H, U, and ϑ are the hydraulic diameter of the channel, the velocity, and kinematic viscosity, respectively.

$$\boldsymbol{D_H = \frac{4A}{P}} \qquad \text{III. 2}$$

The heat transfer coefficient is given by the following relationship:

$$\boldsymbol{h = \frac{Q}{S(T_\omega - T_b)}} \qquad \text{III. 3}$$

Where the heat energy flux:

$$\boldsymbol{Q = \dot{m}\, C_P (T_{out} - T_{in})} \qquad \text{III. 4}$$

S is the passing section, $\dot{m}$ mass flow rate, C_p specific heat, T_{in} and T_{out} are the inlet and the outlet temperature, T_w, T_b absorber plate, and bulk temperatures.

The local heat transfer coefficient given by the following:

$$\boldsymbol{h_x = \frac{Q}{S(T_{w,x} T_{b,x})}} \qquad \text{III. 5}$$

The local Nusselt also as follows:

$$\boldsymbol{Nu_x = \frac{h_x D_H}{\lambda}} \qquad \text{III. 6}$$

The average Nusselt number can be expressed as follows, where λ represents the thermal conductivity (Equation III.7)

$$\boldsymbol{Nu = \frac{1}{S} \int Nu_x dx} \qquad \text{III. 7}$$

The friction factor is a fundamental parameter that is related to the hydraulic performance of fluid systems. It is affected by several parameters, including the Reynolds number, surface roughness, and flow rate. Understanding the relationship between these parameters and the friction factor is essential for designing and optimizing fluid systems for various applications, its relationship is as follows:

$$\boldsymbol{f = \frac{(\Delta P/L) D_H}{2\rho U^2}} \qquad \text{III. 8}$$

Where L and ρ are the duct length, and the density respectively.

There is a parameter that the Thermo-hydraulic side combines at the same time for different heat transfer channels with obstacles, suggested by R. L. WEBB [59] in 1972 where the thermo-hydraulic performance factor (THPF) defined by the ratio of thermal and fluid dynamic performance [58], Its equation is given as follows:

$$\text{THPF} = (Nu/Nu_0)/(f/f_0)^{1/3} \qquad \text{III.9}$$

Where Nu and Nu_0, are the Nusselt number collector with, and without baffles respectively.

Governing equations

We have airflow Newtonian, incompressible inside a 2D duct using CFD Ansys Fluent 18.1, governed by Navier-Stockes equations, continuity equation, and the energy equation. These equations are given as follows:

Continuity equation:

$$\frac{\partial}{\partial x_i}(\rho u_i) = 0 \qquad \text{III.10}$$

Momentum equations:

$$\frac{\partial}{\partial x_j}(\rho u_i u_j) = \frac{\partial P}{\partial x_i} + \frac{\partial}{\partial x_j}\left[\mu\left(\frac{\partial u_i}{\partial x_j} + \frac{\partial u_j}{\partial x_i}\right) + \left(-\rho\overline{u_i' u_j'}\right)\right] \qquad \text{III. 11}$$

Energy equation:

$$\frac{\partial}{\partial x_i}(\rho u_i T) = \frac{\partial}{\partial x_i}\left((\Gamma + \Gamma_t)\frac{\partial T}{\partial x_j}\right) \qquad \text{III. 12}$$

Where:

$-\rho\overline{u_i' u_j'}$ Tensor of Reynolds stresses, μ turbulent viscosity coefficient, Γ, and Γ_t the molecular thermal diffusivity, and the turbulent thermal diffusivity respectively, u velocity of x and y, T, P and ρ are the average temperature, average pressure and average density respectively.

III.2.1 Model selected

In the CFD study, RNG k-ε model was chosen to simulate the heat transfer in the flow equations, this model consists of kinetic energy transfer equations κ and its dissipation rate ε, and their expression is given as follows:

$$\frac{\partial}{\partial x_i}(\rho k u_i) = \frac{\partial}{\partial x_j}\left[\left(\mu + \frac{\mu_t}{\sigma_k}\right)\frac{\partial k}{\partial x_j}\right] + G_K + G_b + \rho\varepsilon \qquad \text{III.13}$$

For the reason of buoyant shear layers for which the main flow direction is perpendicular to the gravitational vector, it can be written as follows:

$$\frac{\partial}{\partial x_i}(\rho k u_i) = \frac{\partial}{\partial x_j}\left[\left(\mu + \frac{\mu_t}{\sigma_\varepsilon}\right)\frac{\partial \varepsilon}{\partial x_j}\right] + (C_{1\varepsilon}G_K - C_{2\varepsilon}^{*}\rho\varepsilon)\frac{\varepsilon}{k} \qquad \text{III. 14}$$

$C_{2\varepsilon}^{*}$, G_K, G_b given as follows:

$$C_{2\varepsilon}^{*} = C_{2\varepsilon} + \frac{C_\mu \eta^3(1 - \eta/\eta_0)}{1 + \beta\eta^3} \qquad \text{III. 15}$$

The production of turbulence kinetic energy:

$$\boldsymbol{G_K} = -\rho\overline{\boldsymbol{u_i'u_j'}}\frac{\partial \boldsymbol{u_j}}{\partial \boldsymbol{x_i}} \qquad \text{III.16}$$

The generation of turbulence kinetic energy:

$$\boldsymbol{G_b} = \beta \boldsymbol{g_i}\, \Gamma_{\boldsymbol{t}} \frac{\partial \boldsymbol{T}}{\partial \boldsymbol{x_j}} \qquad \text{III. 17}$$

Where $C_{1\varepsilon}$ and $C_{2\varepsilon}$ are the closure coefficients, σ effective Prandtl number, T, P and ρ are the average temperature, average pressure, and average density respectively.

III.3 CFD set-up

Following the experimental investigation, the design stage was carried out using Ansys Fluent 18.1. This involved three primary stages: creating the geometrical model using Ansys Fluent Design Modeller (DM), meshing the model with the same software, and specifying the boundary conditions and turbulence model. The air was considered a Newtonian fluid, with fixed properties. The SIMPLE algorithm (Patankar et al [60]) was utilized to obtain the pressure and velocity fields. The equations for conservation of energy, continuity, and momentum were solved iteratively until convergence was reached, with a monitor value of 10^{-6} for the energy equation and 10^{-3} for the remaining equations (continuity, x-y velocity, K, and epsilon). The three key elements of the digital stage are elaborated upon below Fig III.1.

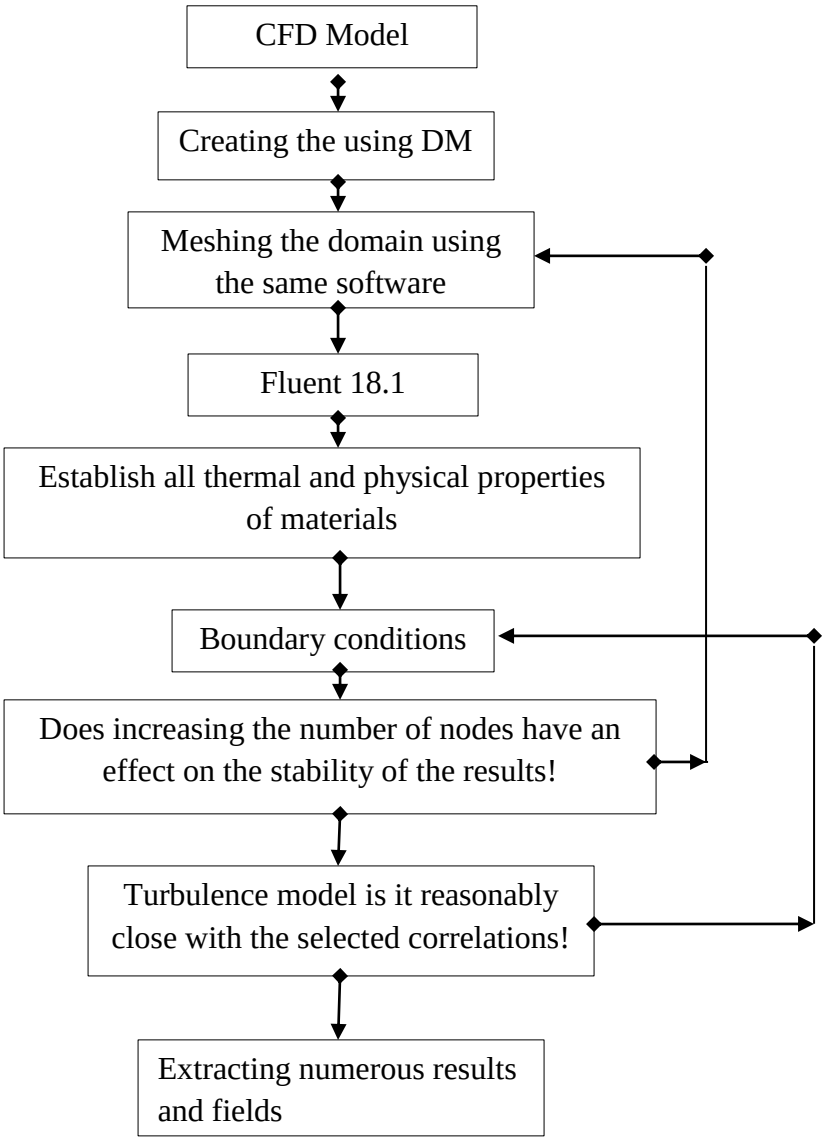

Figure III.1 CFD analysis diagram.

III.3.1 Creation of the CFD geometry

Using Ansys Fluent 18.1, part of the Design Modeler (DM), a numerical model of our SAC was formed. The dimensions of the collector, including the air duct and baffles, were based on the actual SAC used in the experiment. Initially, a model of the SAC without any baffles was created, followed by a model with two baffles for validation with the experimental investigation. Two baffles were then added from both sides until the duct was completely filled, resulting in a total of four cases, in addition to the reference case of smooth plate. Fig III.2 shows longitudinal sections of the SAC duct with baffles for all cases, with a fixed distance of 10 cm between each two baffles. The cases are labeled from the first case (18b) to the fourth case with six baffles (6b), respectively.

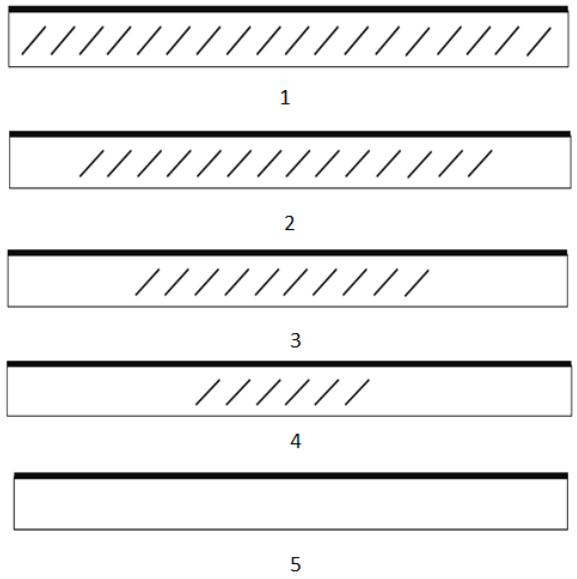

Figure III.2 Studied models.

III.3.2 Meshing the CFD geometry

To create a comprehensive two-dimensional model of the SAC, Ansys Workbench 18.1 software was employed. The model was meshed using the 2D structured mesh quadrilateral cells type method, chosen for its enhanced accuracy and reduced computational time in solving the equations. To ensure a high-quality mesh throughout the model, size function proximity and curvature were employed, enabling optimal division regardless of the geometrical shape of the areas. The mesh was further refined by incorporating high smoothing quality and fine relevance center settings, resulting in improved meshing quality.

Continuous updates and improvements were made to the mesh by reducing the maximum face size while considering the overall number of elements. The objective was to achieve a balance between maximizing the quantity of elements and minimizing their count, a parameter controlled by approaching value constancy as outlined in Table III.1.

To evaluate the effectiveness of the meshing approach, a specific test scenario was conducted. The test involved the mass flow rate $\dot{m}$=0.024 kg/s at 13:00 on May 17, 2021. The absorber temperature was set at T=363.94 K, while the inlet temperature was maintained at T=315.6 K. This analysis aimed to ensure accurate and reliable results by validating the meshing strategy under specific operating conditions.

The effect of the number of nodes was also studied on another case, which is case M, which showed almost the same effect as the previous case

Table III.1 Meshing effect.

Nodes	Elements	Sum Temperture	Exp Temperture	x%
24292	25075	336.85	339.4	0.751326
41391	40274	337.38	339.4	0.595168
60398	58953	337.58	339.4	0.53624
111851	109754	337.74	339.4	0.489098
158960	156466	337.78	339.4	0.68359

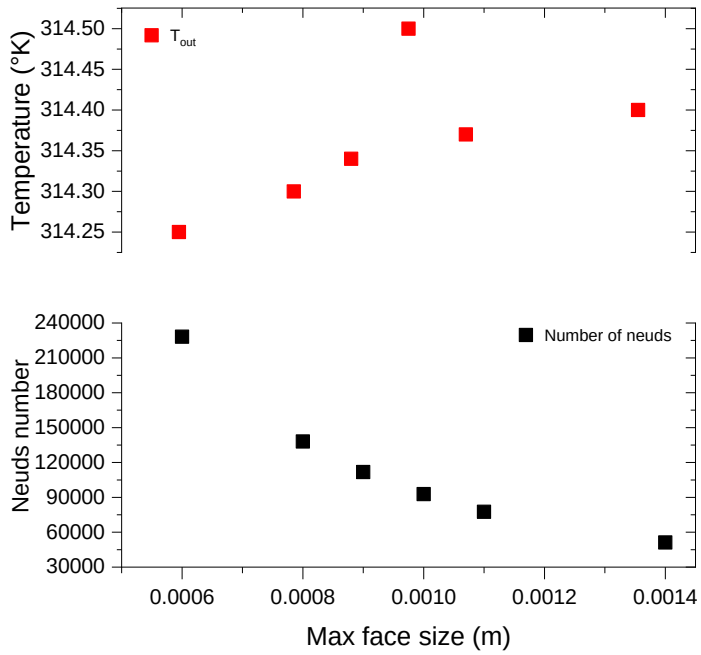

Figure III.3 The effect of the number of nodes in Mode M at m=0.032Kg/s, I=911W/m^2, and T_{out}=316.9k.

The method of meshing was done using size function proximity and curvature; this is to divide all areas homogeneously, regardless of their geometrical form, using smoothing high quality. The number of nodes was maintained using the max face size dimension since their number affects the study results. This characteristic must be taken into account, and this is represented in Fig III.3, where the increase in the number of nodes over the outlet temperature was studied in the experimental M case- at m=0.032Kg/s, I=911W/m^2, and T_{out}=316.9k. It was noted that there is a slight change in temperature by increasing the number of nodes, but it is nearly negligible. The division was chosen when the number of nodes is within NON =110958 nodes. This is due to the accuracy of the results and the extracted fields.

The Y-plus (Y+) value is important in CFD simulations because it determines the distance between the first node of the mesh layer and the wall. This distance is crucial in accurately capturing the behaviour of the fluid flow near the wall, where the velocity gradient is high. Y-

plus is defined as the ratio between the distance of the first node to the wall and the viscous length scale, which is calculated as the ratio between the dynamic viscosity of the fluid and the wall shear stress.

To ensure accurate simulation results, it is recommended to maintain a Y-plus value close to one, which means that the first node of the mesh layer should be close to the wall. The growth rate of Y-plus should also be limited to a value of 1.2 or less to ensure that the mesh is fine enough to capture the fluid flow behaviour near the wall. (Fig III.4, 5) [6].

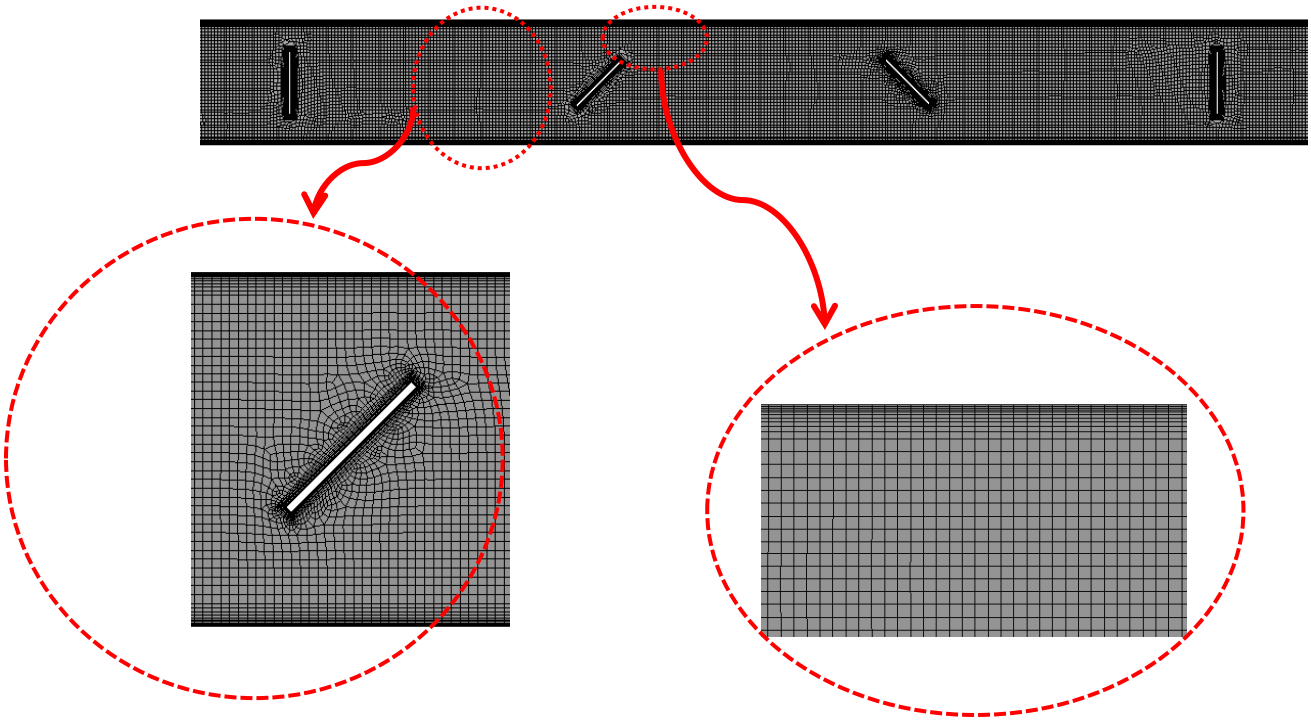

Figure III.4 Meshing the system into contract taking into account Y^+.

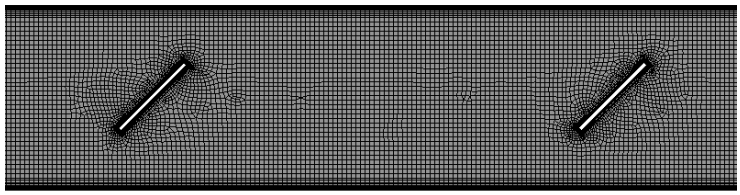

(a)

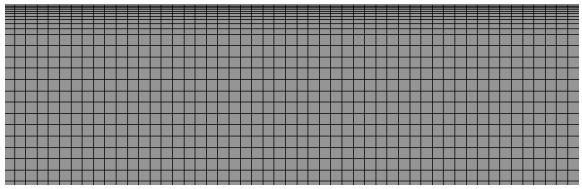

(b)

Figure III.5 Computational grid, a: channel with baffles, b: near of the wall.

III.3.3 Turbulence models

Using the baffles in the SAC was aimed to increase the heat transfer from the absorber plate to the air by inducing turbulence in the flow. To evaluate the performance of the baffles, multiple numerical models were used. In a study by Menasria et al.[58] four classic k-ε models were tested using semi-empirical correlations of Gnielinski and Petukhov [61] (Cengel). The model selection was based on a comparison of the numerical results obtained with each model to previous experimental results. The CFD results of Friction Coefficient and Nusselt Number for different k-ε turbulence models were compared with Modified Blasius, and Dittus-Boelter correlations as proposed by Fox, McDonald et al. [62]

$$\boldsymbol{Nu = 0.023Re^{0.8}Pr^{0.4}} \qquad \text{III. 18}$$

$$\boldsymbol{f = 0.791Re^{-0.25}} \qquad \text{III. 19}$$

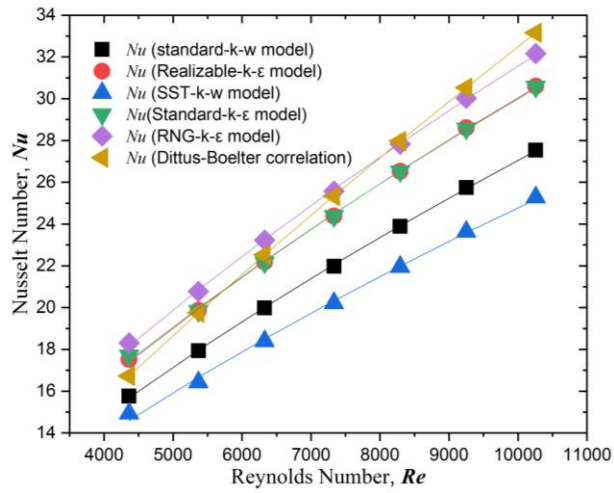

Figure III.6 Predicted values of Nusselt Number for different k-ε, and k- ω turbulence models with Dittus-Boelter correlation.

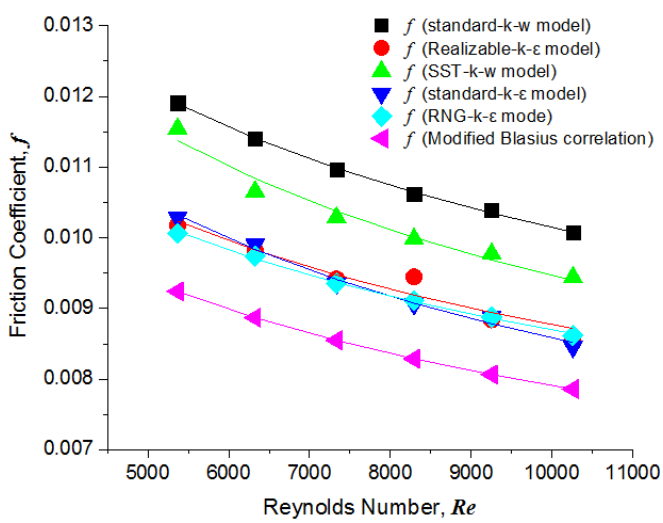

Figure III.7 Predicted values of Friction Coefficient for different k-ε, and k-w turbulence models with Modified Blasius correlation.

The numerical study aimed to investigate the characteristics of turbulent flow in a duct containing baffles. Multiple turbulence models were assessed to identify the most appropriate model for this specific flow scenario. The evaluated turbulence models included standard k-ε, RNG k-ε, realizable k-ε, standard-k-ω, and SST-k-ω. These models were tested and their results were compared with established correlations available in the literature to assess their accuracy.

In order to evaluate the performance of the turbulence models, the study extracted the Nusselt number (*Nu*) and the Friction Coefficient (*f*) for various Reynolds numbers. These values were then compared with the Modified Blasius and Dittus-Boelter correlations, which are well-established references in the field. By comparing the numerical results with these correlations, the study aimed to determine the reliability and suitability of the turbulence models in accurately predicting the heat transfer characteristics and frictional losses in the duct with baffles.

The RNG k-ε turbulence model was selected for this study due to its capability to account for streamlined curvatures at low Reynolds numbers, as mentioned in Duffie and Beckman's work from 1980 [63], it takes into consideration the effects of streamlined curvatures at relatively small Reynolds numbers, as discussed by Menasri et al.[58] The study observed that in a smooth channel, as the Reynolds number increased, there was a corresponding increase in the Nusselt number (Fig III.6). Additionally, it was noted that with increasing Reynolds number, the coefficient of friction decreased (Fig III.7). The results indicated that the RNG k-ε model aligned well with the Dittus-Boelter correlation and provided the closest approximation to the Friction Coefficient compared to the other models when considering the same number of cells on a smooth plate.

Moreover, there was consistency between the realizable k-ε and standard-k-ε models in both sets of results. The CFD results demonstrated a strong correlation between the RNG k-ε model and both the Dittus-Boelter and Modified Blasius correlations. These findings, coupled with previous research by Karmare et al.[64]; Yadav et al [65]; and Jin et al [66], who also utilized the RNG k-ε model in the context of SACs, led to the selection of the RNG k-ε model for the current study.

III.4 Validation

In the evaluation process, all boundary conditions were based on the experiment Table III.2. A consistent temperature was maintained at the absorber plate and bottom plate in all tests as shown in Fig III.8. Similarly, the mass flow rate, inlet temperature, hydraulic diameter, and turbulent intensity were all held constant. The turbulent intensity was varied between 5.020 and 5.963, as specified: (Safer et al [67] Menasria et al [58])

$$I=0.16(Re)^{-1/8} \qquad \text{III.20}$$

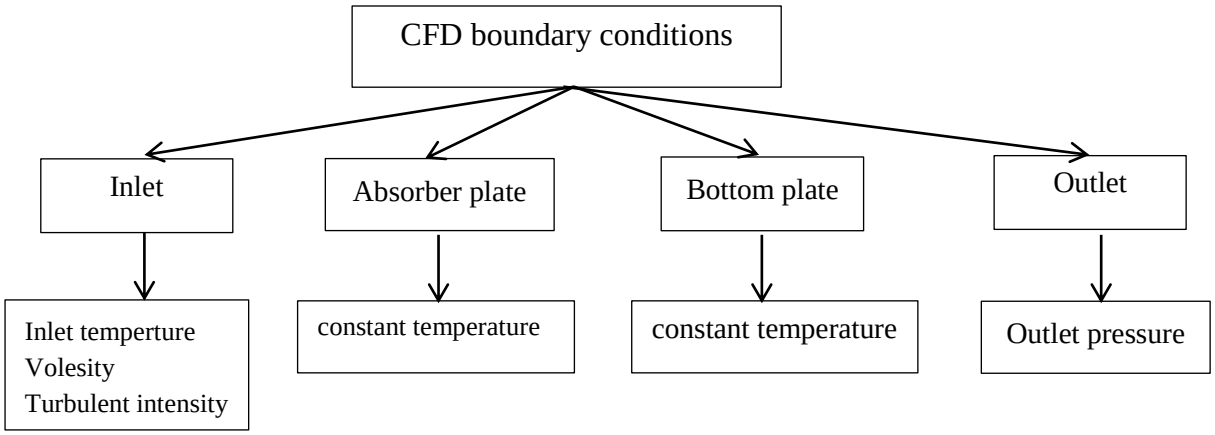

Figure III.8 CFD boundary conditions.

Table III.2 Boundary conditions.

Absorber plate	constant temperature
Inlet	temperature inlet, mass flow rate
Bottom plate	constant temperature

In the case of the empirical comparison of the SAC with two baffles placed in the middle of the channel, and for Reynolds numbers ranging from Re=2687 to Re=3844, all properties of air and the components of the collector were considered to be constant. The validation process involved comparing the outlet temperature obtained from the experiment with that obtained from the CFD analysis for two different cases. The objective was to assess the accuracy and validity of the numerical model.

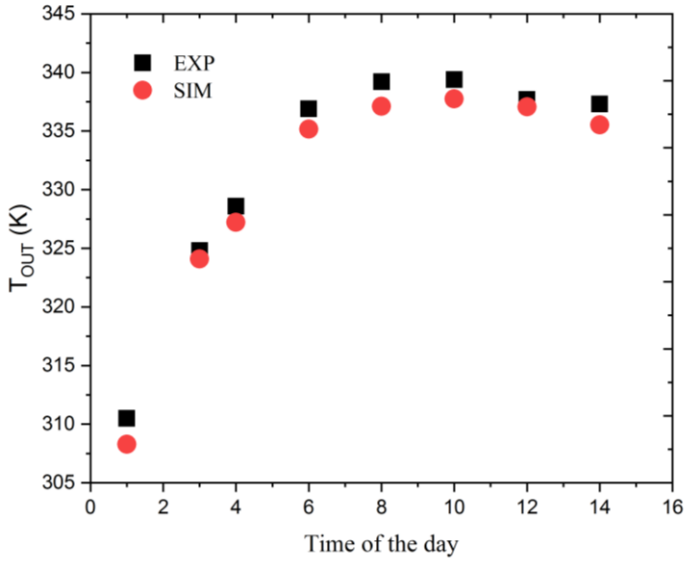

Figure III.9 Outlet temperature as a function of hours of the day for mass flow rate m=0.024kg/s.

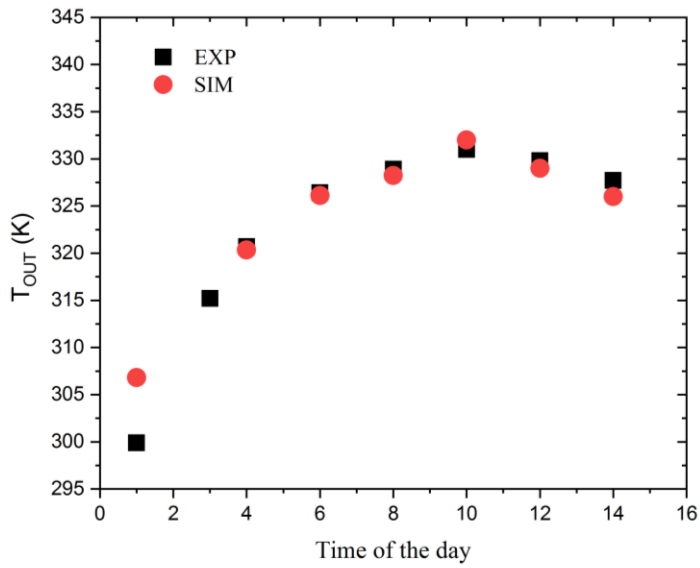

Figure III.10 Outlet temperature as a function of hours of the day for mass flow rate m=0.032 kg/s.

The CFD analysis and experimental results indicated excellent agreement for different hours of the day, with varying values of solar radiation and mass flow rates. In this study, all controllable parameters were varied as shown in Fig III.9, 10, and that to verify the accuracy of the CFD model. The differences between the experimental and simulation models are attributed to various factors, including measurement errors of experimental devices, thermal insulation, and other sources of error. Based on these comparison results, the numerical model's validity has been confirmed, demonstrating its potential for use in other modes. To confirm the validity of the simulation in other models, a comparison was also made in cases M and H in another parallel study that we mention with the previous one Fig III.11.

Through the curves Fig III.12, we note that as the mass flow rates increase, the outlet temperature decreases in both cases. The results are very close between both the numerical and experimental sides, which ultimately show the effectiveness of the CFD model. There is a small percentage of difference that does not exceed one per cent. The latter is due to several reasons, the most important of which are thermal insulation and measurement uncertainty.

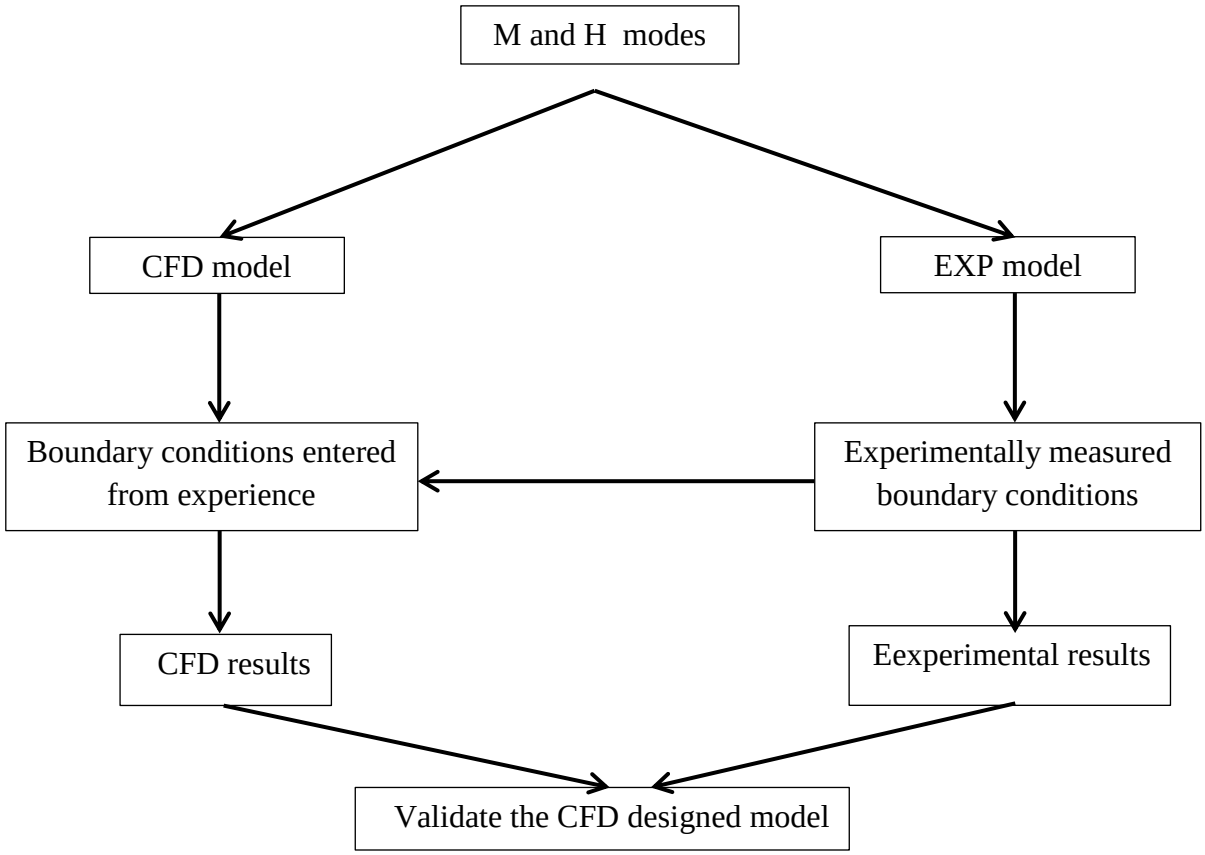

Figure III.11 Methodology of validation diagram (M and H cases).

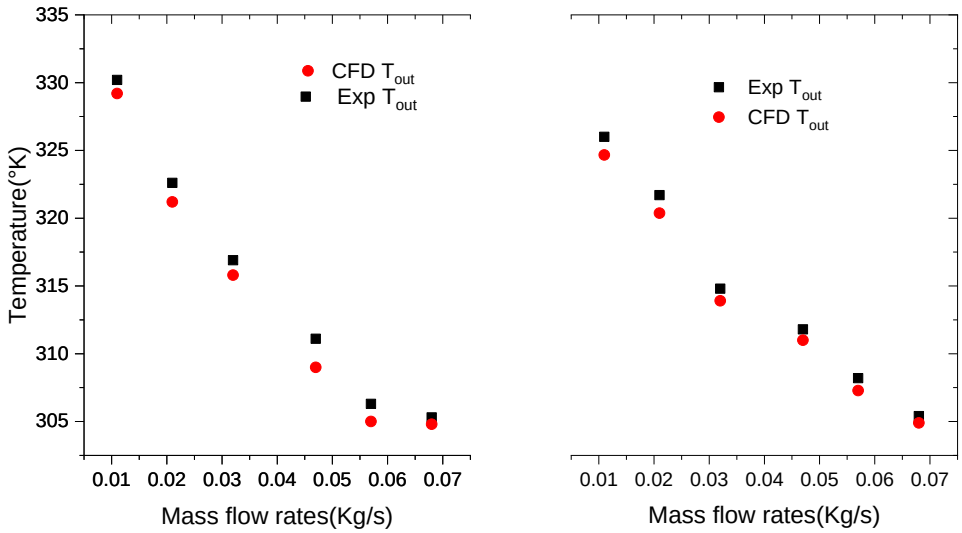

Figure III.12 Numerically and experimentally outlet temperature in terms of mass flow rates for the two cases M and H respectively.

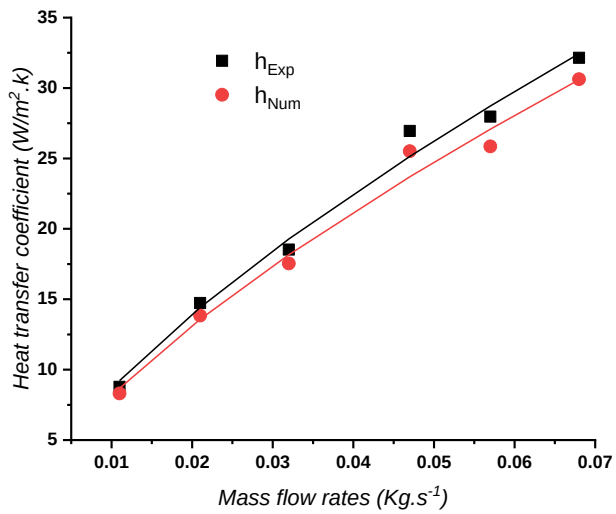

Figure III.13 Heat transfer coefficient as a function of mass flow rates for H case.

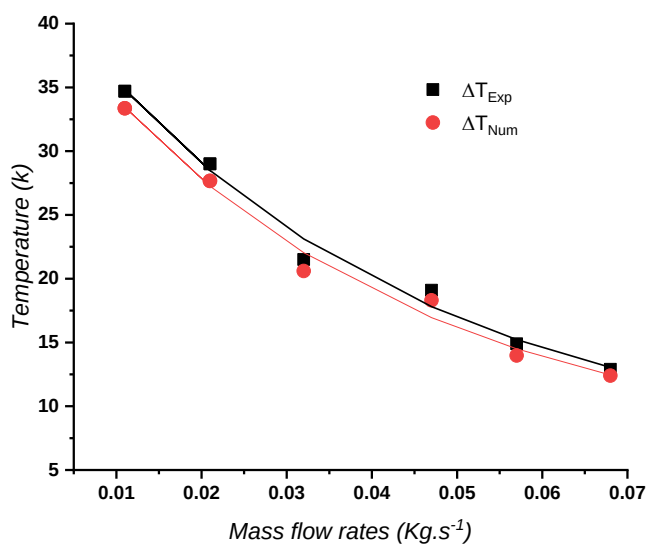

Figure III.14 Variation of Temperature difference as a function of mass flow rates.

Fig III.13 illustrates the variation of the heat transfer coefficient as a function of mass flow rates, for both the experimental and numerical investigations inside the SAC's duct. It can be observed that there is a remarkable level of agreement between the experimental results and the CFD results, thereby confirming the validity of the designed model. Additionally, as the mass flow rates increases, the heat transfer coefficient also increases, which implies a corresponding increase in heat transfer. This observation is consistent with the results obtained from the heat absorber plate. The highest heat transfer coefficient value was attained in the experimental investigation at h=32.14W/m^2.k for a mass flow rate of m=0.068Kg/s. In the case of CFD, at the same mass flow rate, the heat transfer coefficient was h=30.62W/m^2.k.

Moving on to another important finding, we examine the temperature difference between the outlet and inlet as a function of mass flow rate obtained through both CFD analysis and experimental investigation as depicted in Fig III.14. This curve further affirms the validity of the numerical model by demonstrating the convergence between the experimental and numerical values. As the temperature of the absorber plate decreases, the temperature difference reaches its peak value of ΔT=34.7°C for a mass flow rate of m=0.011Kg/s in the experimental investigation, and ΔT=33.36°C in the CFD investigation.

III.5 Conclusion

This chapter of the study relied on numerical and experimental procedures, the aim of which was to ensure the validity of the model of CFD. The effect of the number of nodes on the numerical results was also studied, and the appropriate number was chosen for this study. Through the experimental and numerical work, we find that the numerical model is effective and valid for all positions and angles of the obstacles inside the channel with its various numbers.

Chapter IV

IV. Results and discussion

IV.1 Introduction

After a thorough investigation that involved conducting experiments and validating the numerical model, it was time to discuss the results of the study. This chapter focuses on the analysis of the computational fluid dynamics (CFD) results obtained from the simulations, and the experimental results. The CFD results provide a detailed insight into the thermal and hydraulic performance of the SAC, and the numerical model was validated to ensure its accuracy and reliability. The results of the numerical investigation were carefully analyzed to understand the fluid flow behavior, and heat transfer characteristics of the collector, providing valuable information about its performance.

This chapter represents an important stage in the study, as it provides an in-depth examination of the results and helps to understand the behavior of the SAC. The discussion of results provides a foundation for further improvement and optimization of the design, leading to more efficient and effective solar energy systems.

IV.2 Experimental results

IV.2.1 Discuss and compare results of radiation

Through the initial observation of measured solar radiation and the derived mathematical model, it has been determined that the change in solar radiation follows a parabolic pattern. The peak solar radiation occurs consistently at 13:00 hours throughout all seasons. Furthermore, it has been observed that the highest levels of solar radiation occur during the summer and spring seasons.

Figs IV.1, IV.2, IV.3, and IV.4, illustrate the variations in global solar irradiation throughout the day, as measured across the horizontal area. The values of solar radiation increase from sunrise, reaching their maximum at midday, and subsequently decrease until sunset in the evening. This trend is observed consistently across all months.

Furthermore, both the prediction model and measurement investigations confirm that the global solar radiation remains below a maximum value of 1000 W/m² (denoted as I). The simulated mathematical model of the experimental results closely aligns with the actual experimental data, demonstrating a high degree of agreement. The minimal difference between them is so insignificant that it can be safely disregarded. This indicates the reliability and accuracy of the obtained model. Consequently, researchers can confidently utilize this model as a benchmark for comparing and validating results from other studies in the literature. Its robustness and consistency make it a valuable tool for further research and analysis in the field of solar radiation.

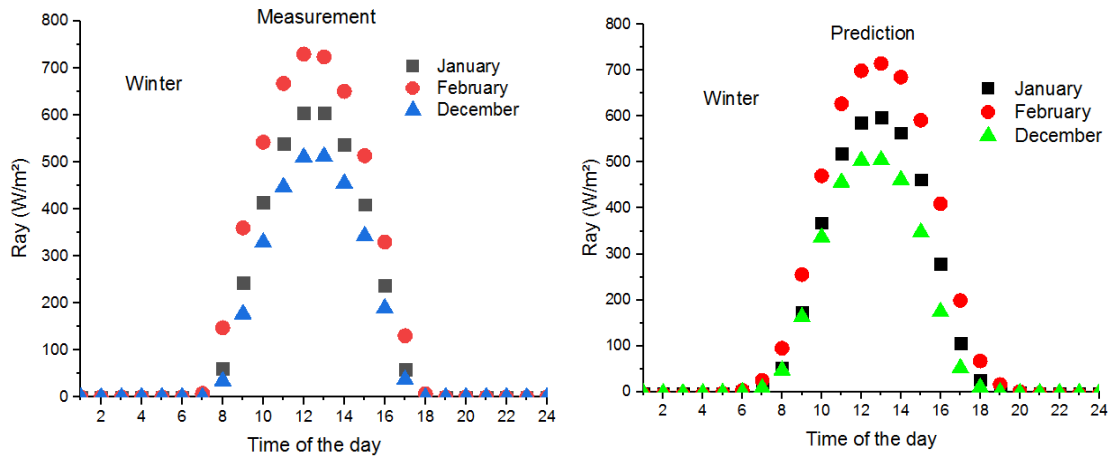

Figure IV.1 Global solar irradiation, according to the season of the winter between measurement, and prediction model.

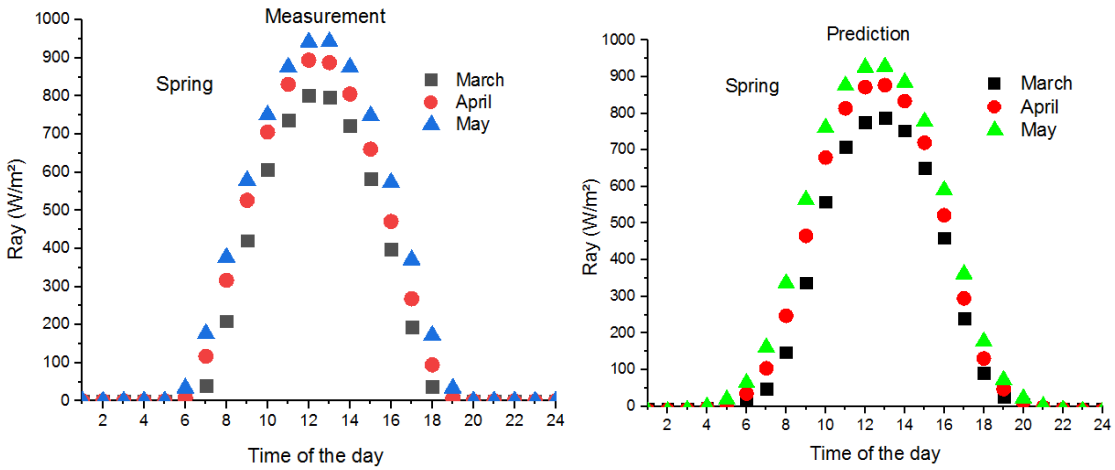

Figure IV. 2 Global solar irradiation, according to the season of the spring between measurement, and prediction model.

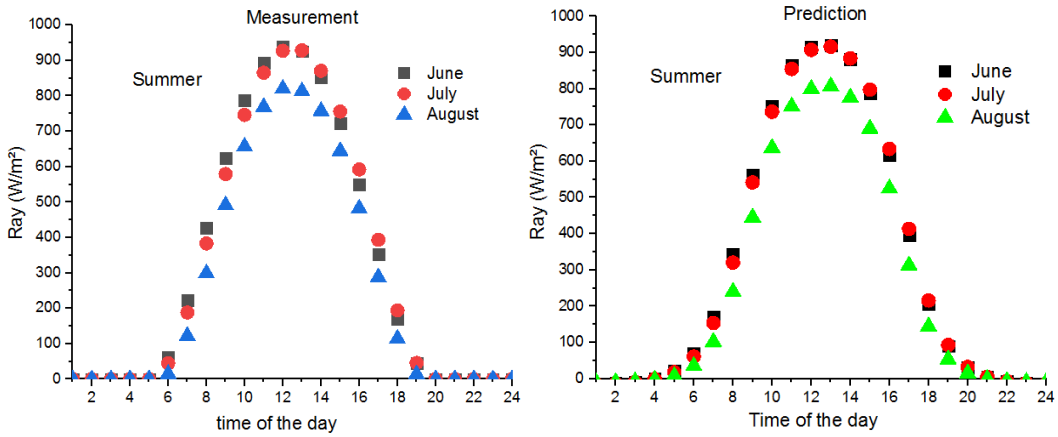

Figure IV.3 Global solar irradiation, according to the season of the summer between measurement, and prediction model.

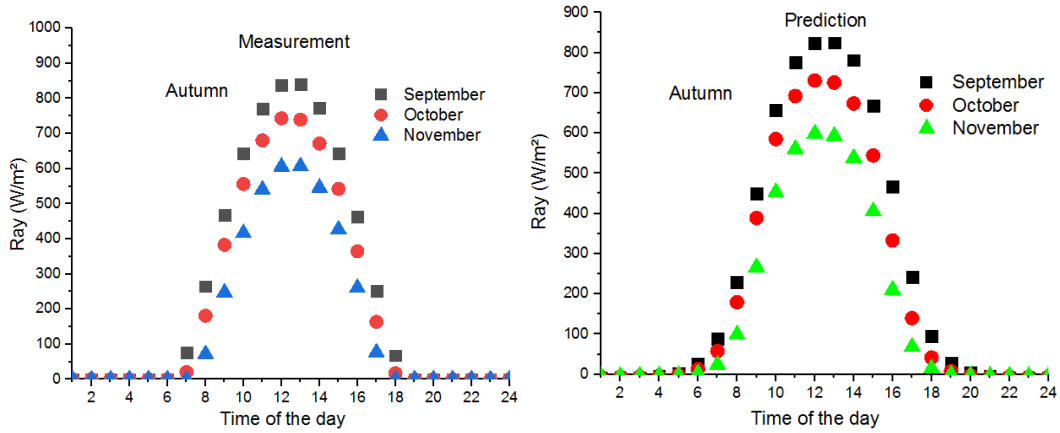

Figure IV.4 Global solar irradiation, according to the season of the autumn between measurement, and prediction model.

IV.2.2 Analytical view of the change in solar radiation throughout the year

Fig IV.5 represents the culmination of our previous analyses, incorporating both the mathematical model and the results of the experimental investigation conducted across all months. In this comprehensive representation, the remarkable agreement between the model and the experimental measurements becomes evident.

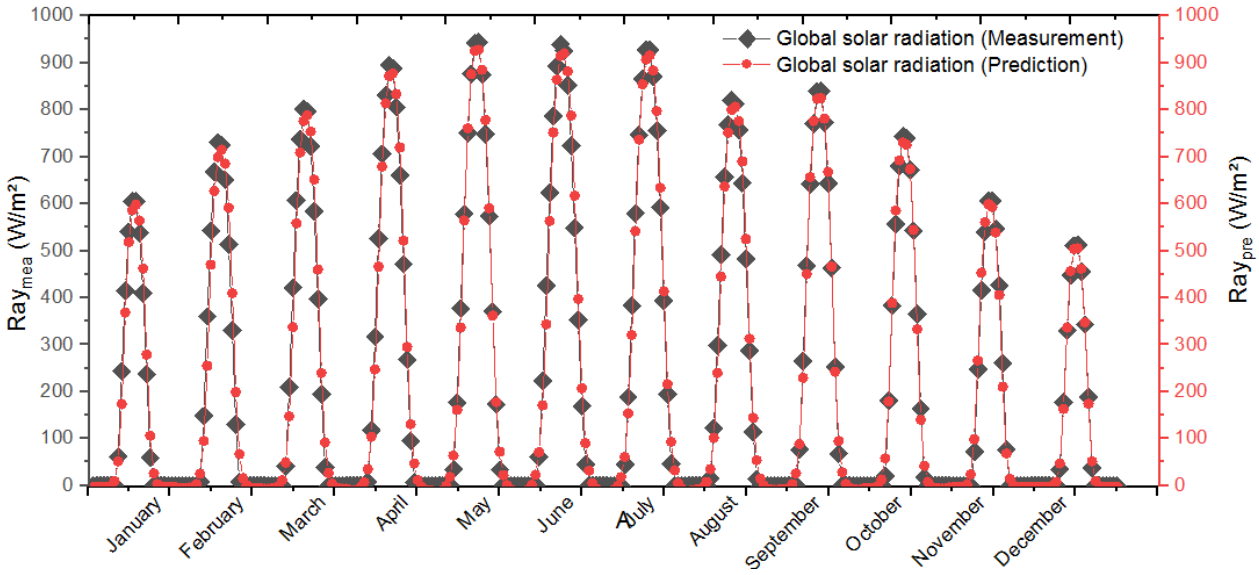

Figure IV.5 Global solar irradiation, and prediction model, according to all the seasons.

Upon examining the data, it is observed that the months of May and June exhibit the highest values of solar radiation. These months experience peak levels of solar energy, resulting in intense radiation. On the other hand, the lowest values of solar radiation are recorded in December, characterized by reduced solar exposure due to shorter daylight hours and lower solar angles.

The graphical depiction in Fig IV.5 not only showcases the consistency and reliability of the developed model but also provides a comprehensive overview of the seasonal variations in solar radiation. This information is invaluable for understanding the temporal patterns of solar energy availability and its potential impact on various applications and systems.

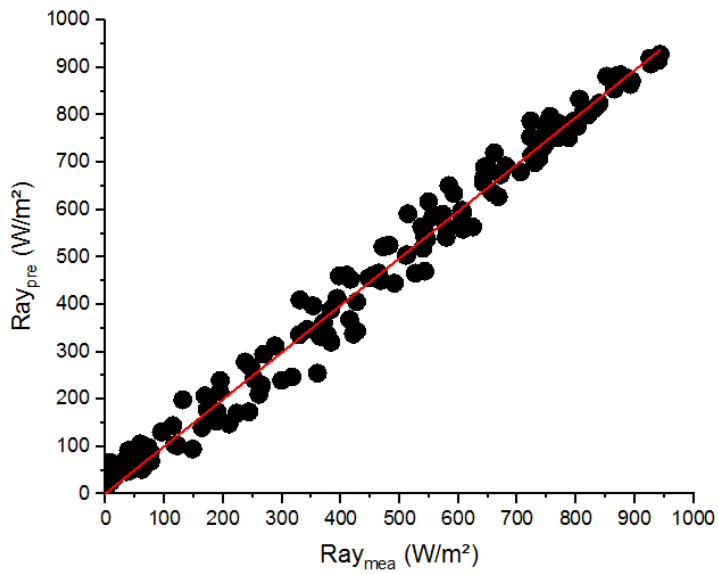

Figure IV.6 Global solar radiation of measurements in terms of global solar radiation prediction.

In Fig IV.6, the mathematical model is presented, with the model's points displayed on the Y axis and the corresponding measured results on the X axis. This analysis reveals that the asymptotic model closely resembles a linear model that adheres to the modified form of y = a.x. notably, the constant 'a' is nearly equal to one, emphasizing the effectiveness of the derived mathematical model. The alignment between the model points and the measured results further supports the reliability and accuracy of the mathematical model. The linear relationship observed indicates a strong correlation between the predicted values and the actual measurements, reinforcing the validity of the model. This analysis through Fig IV.5 underscores the utility of the obtained mathematical model in predicting and understanding the relationship between variables. Researchers can confidently utilize this model to make accurate projections and draw meaningful conclusions in their studies.

In the last Figure (Fig IV.7), we depict the variation of constants throughout the months by presenting them as curves. This graphical representation provides a clearer and more comprehensive view of the obtained mathematical model. By observing the curves, we can discern any patterns or trends in the behavior of the constants over time. This information allows us to gain deeper insights into the underlying dynamics of the system and how they evolve on a monthly basis.

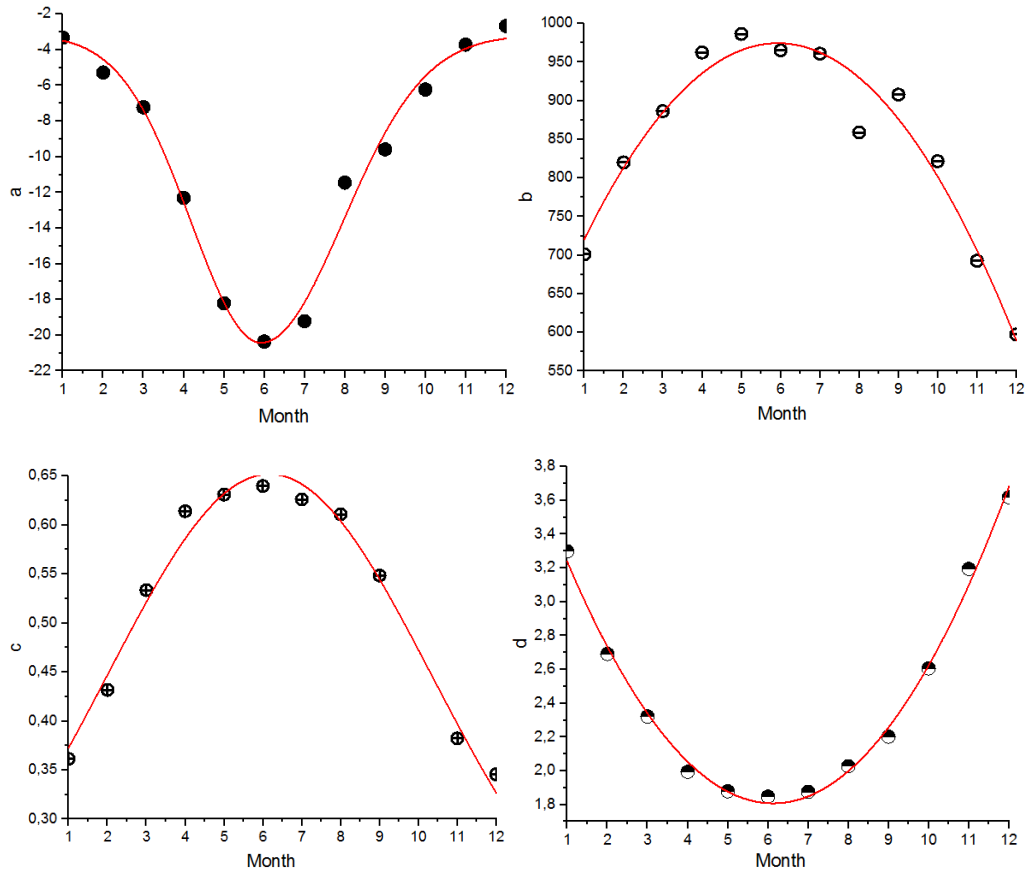

Figure IV.7 The constants a, b, c, and d in every month.

Through this comprehensive study, its outputs can be summarized in a detailed text; a mathematical model for global solar radiation has been developed, taking into account various temporal and spatial characteristics such as a, b, c, d, and h on a horizontal surface. This model specifically applies to the city of Biskra and has been carefully validated against real measurements of solar radiation to ensure its accuracy and effectiveness. By examining the graph representing the solar radiation data and the corresponding predictions from the model, it becomes evident that they closely align with each other. The patterns and fluctuations in solar radiation throughout the specified days exhibit a consistent agreement between the measurements and the model's projections. This congruence between the observed and predicted values provides strong evidence supporting the validity and reliability of the developed mathematical model. Such confirmation of the model's accuracy reinforces its utility for various applications, including solar energy planning, resource management, and the design of solar-based systems in the region. Researchers and practitioners can confidently rely on this model for making informed decisions and conducting further analyses related to solar radiation in Biskra.

IV.2.3 Thermal performances

IV.2.3.1 ***Bottom and absorber plates temperature***

The first curve Fig IV.8, presented the temperature of the absorber plate as a function of the length, in the different mass flows.

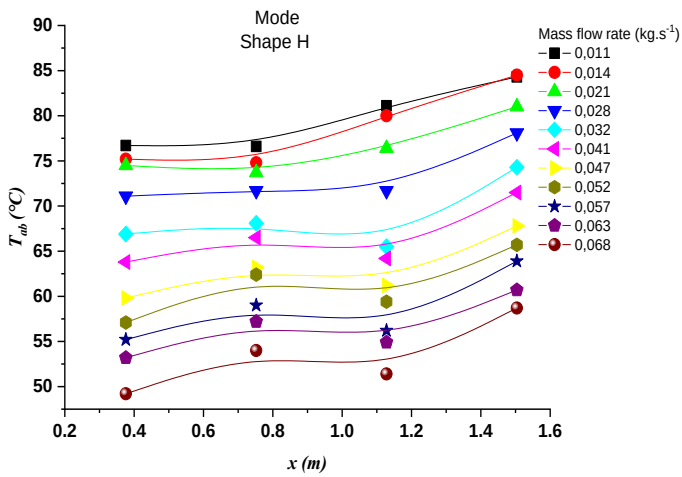

Figure IV.8 Temperature of the absorber plate as a function of the length, in the different mass flow rates.

Upon observing the temperature curves, it became apparent that all curves exhibited a similar trend of temperature rising from the inlet to the outlet of the plate. The maximum temperature values were recorded at the final measurement point, located at the length of x=1.50m. Furthermore, it was noted that an increase in mass flow led to a decrease in the average temperature of the absorber plate, indicating an increase in heat transfer from the plate to the air.

The placement of baffles had a noticeable effect on heat transfer within the collector, particularly on the absorber plate temperature. In the middle region of the collector, where the four baffles were positioned between x = 0.752m to x = 1.128m, the temperature of the absorber plate exhibited a decrease. This can be attributed to the creation of turbulent flow in that area and the disruption of dead thermal layers near the walls.

The temperature of the bottom plate, as depicted in Fig IV.9, exhibited a similar trend to that of the absorber plate. This can be attributed to the plate's thermal resistance against the convective heat transfer from the air.

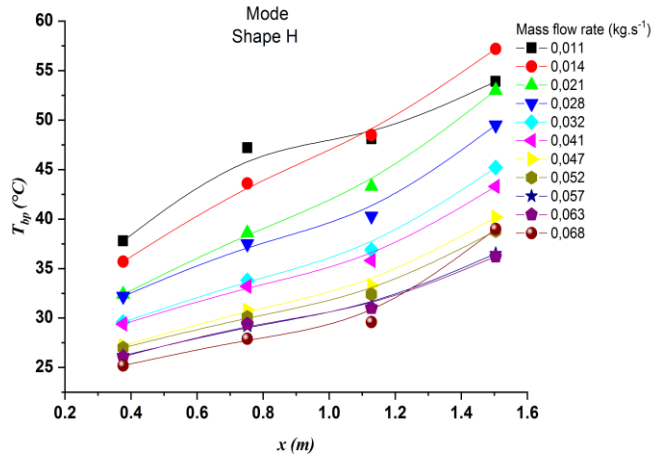

Figure IV.9 Temperature of the bottom plate as a function of its length for different mass flows.

The highest temperature value was recorded at x=1.5, consistent with the absorber plate. Among the various mass flow rates, the highest temperature value was observed in the lowest flow rate of m=0.011 kg/s[55]

IV.2.3.1 ***Inlet and outlet temperature***

The results of the experimental tests are presented in Fig IV.10, which displays the temperature difference between the inlet and outlet of the SAC over the course of a day for three different mass flow rates: m = 0.014 kg/s, m=0.023kg/s, and m=0.032 kg/s. It is observed that the time of day has a significant effect on the performances of the SAC, with the maximum temperature difference occurring at noon. Furthermore, the heat difference values are dependent on the mass flow rate, as they increase with an increase in flow. The highest heat difference was recorded in Case V, with a maximum value of ΔT= 35.3°C for a flow rate of m=0.024 kg /s at 11:30, while the lowest values were observed in the smooth plate case, with a heat difference of ΔT= in the case of m=0.032 Kg/s.

The number of baffles also plays a crucial role in determining the temperature difference, with an increase in baffles leading to a corresponding increase in the temperature difference due to the turbulence generated by the obstacles, which in turn enhances the heat transfer process. However, there are some exceptions such as case II at m=0.024 kg/s and m=0.032kg/s where the value of solar radiation is weak due to weather disturbances. In general, the temperature difference increases with the number of baffles and the decrease in flow rate.

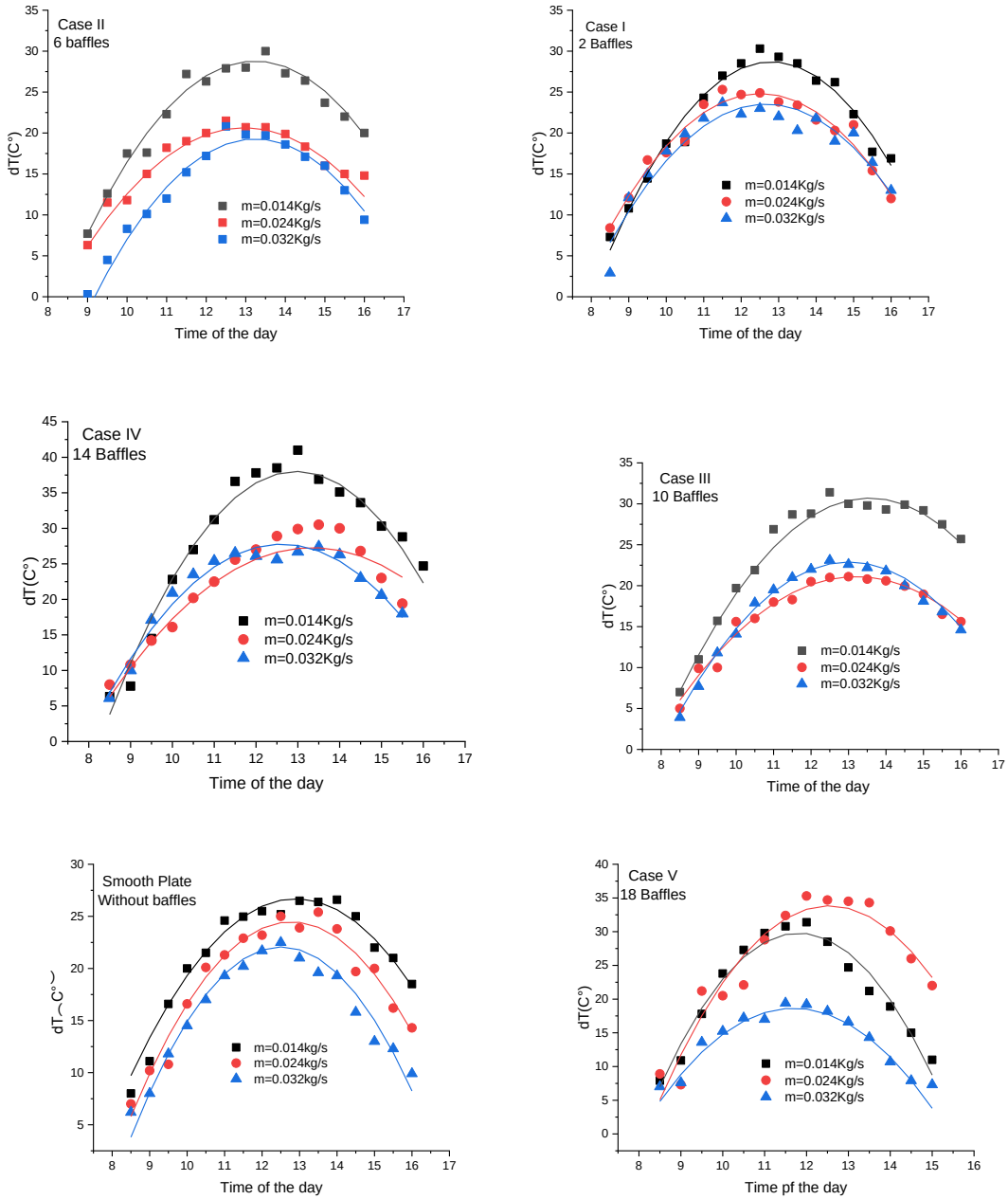

Figure IV.10 Temperature difference as a function of hours of the day, at different mass flows for all cases.

IV.2.3.2 *Local temperature and Nusselt numbers*

The local temperature and local Nusselt number are important parameters studied in the field of forced convection heat transfer. In this study, the local temperature and Nusselt number were analyzed at four different zones (1, 2, 3, and 4) of the channel, as shown in Fig IV.11. The results of this analysis were then compared at different mass flow rates, as depicted in Fig IV.12, 13.

From the results, it was observed that the temperature increased as the air moved forward through the d, with all the maximum values being recorded in zone 4. On the other hand, the local Nusselt number showed an opposite trend to the temperature, being greater at the beginning of the duct (L=0.375m), and decreasing as the air advanced forward. The highest value of the local Nusselt number was recorded at 13:30, and *Nu*=61.92, m=0.032kg/s. These observations were found to be consistent across all the different hours of the day shown in Fig IV.13, indicating that the heat transfer increased as the air moved towards the outlet. The reason behind this can be attributed to the difference in temperature between the air and the absorber plate, which gradually decreased as the air moved forward. This decrease in temperature difference caused a decrease in the heat transfer, which in turn led to a direct effect on the local heat transfer coefficient. It was also found that the highest temperature values were noted at a mass flow of m=0.014kg/s, where the heat transfer was less than the rest of the flows. The maximum value of T_{Local}=54.16°C was recorded at 13:30 and L=1.5m. These results highlight the importance of considering both the local temperature and Nusselt number when analyzing the performance of a forced convection heat transfer system. The results obtained from the experiments show that heat transfer increases as the air moves towards the outlet, which is consistent with the observations made at all times of the day. This increase in heat transfer can be explained by the difference in temperature between the air and the absorber plate, which is significant at the beginning of the channel and begins to decrease as the air advances forward. Due to this decrease in heat transfer, the local heat transfer coefficient is directly affected by the temperature difference mentioned above. It is worth noting that the highest temperature of air values were recorded at a mass flow rate of m=0.014kg/s, which is the flow rate where heat transfer was the least effective compared to the other flow rates. Moreover, the maximum temperature value of T_{Local}=54.16°C was recorded at 13:30 and L=1.5m. These findings provide important insights into the design and optimization of SACs, particularly in terms of selecting the appropriate mass flow rate to achieve optimal heat transfer performance.

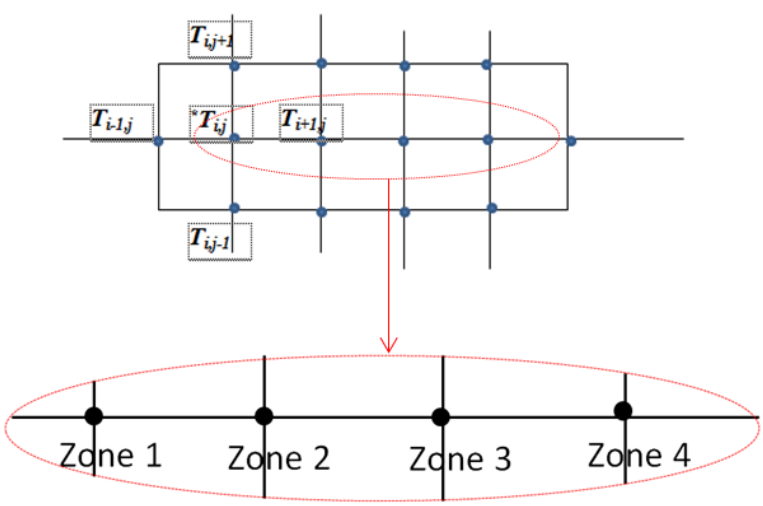

Figure IV.11 Discretization of zones.

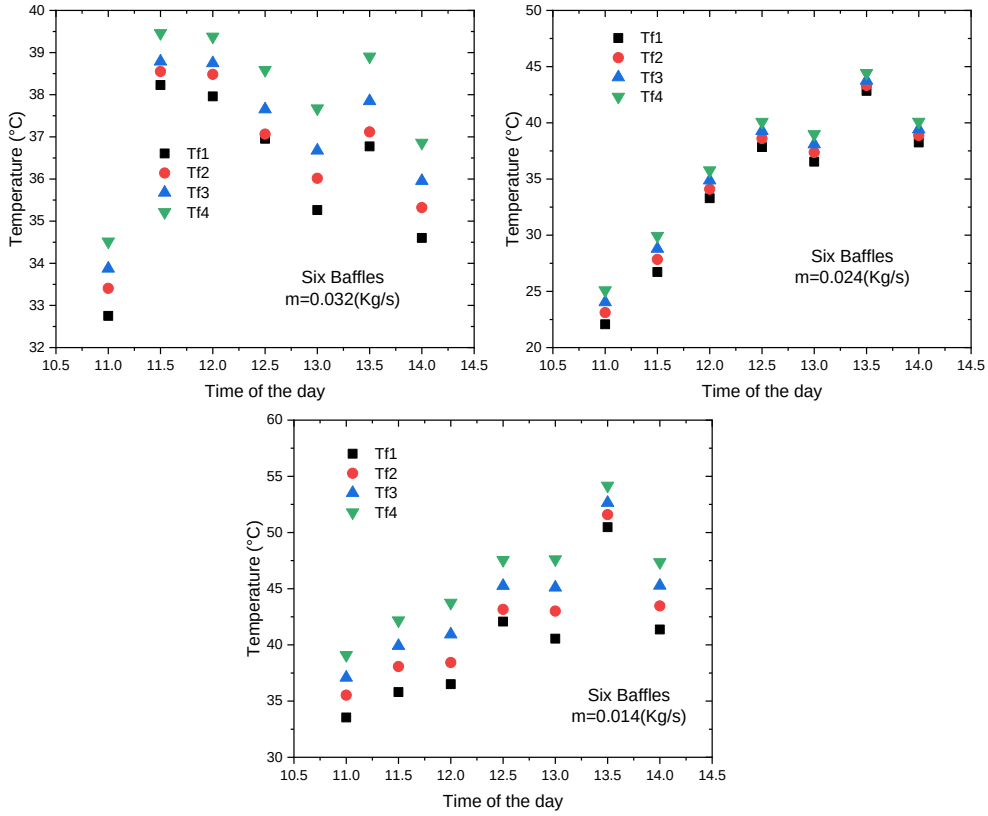

Figure IV.12 The local temperature of air as a function of hours of the day, at different mass flows.

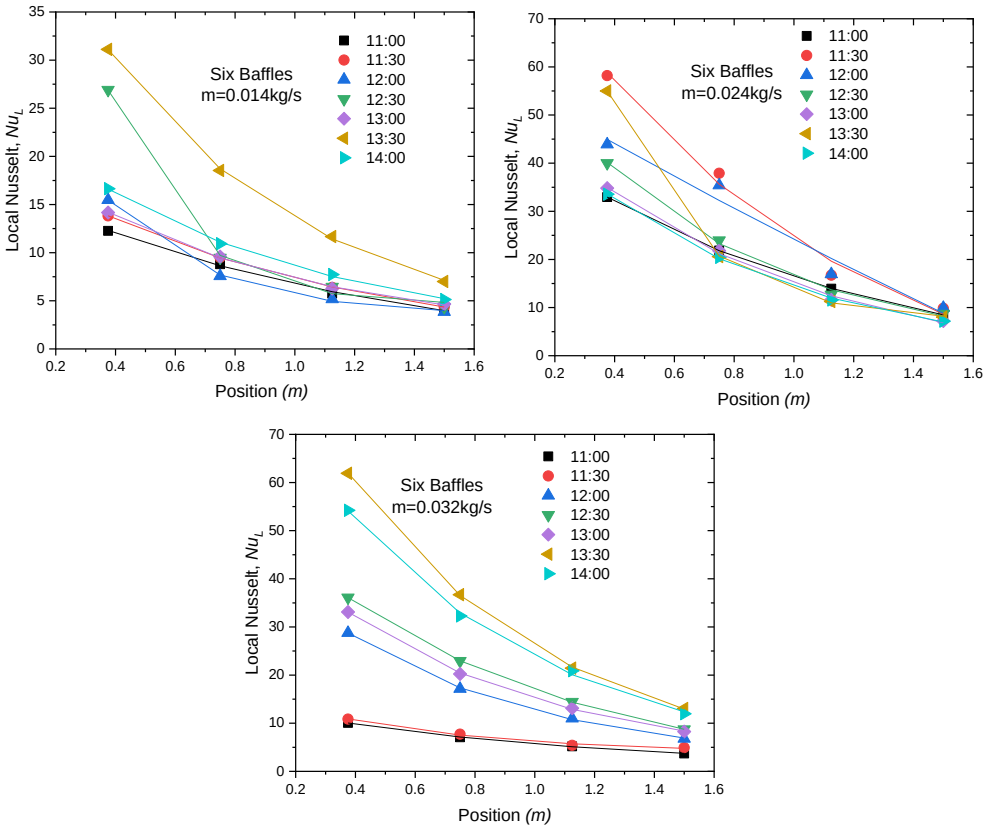

Figure IV.13 The local Nusselt numbers as a function of hours of the day, at different flows.

IV.2.3.3 ***Heat transfer coefficient***

Fig IV.14 illustrates the variation of the heat transfer coefficient over the course of a day, considering the three different mass flow rates. The graph reveals that the heat transfer coefficient starts with relatively lower values during the early morning and late afternoon. However, during the midday period, the values significantly increase, reaching their peak. Notably, the highest heat transfer coefficients were observed for mass flow rates of m=0.032 kg/s and m=0.024 kg/s in both cases IV and V. At specific time points, namely 12:30 and 13:30, the maximum heat transfer coefficients were recorded, measuring h=15.84 W/m²K and h=17.46 W/m²K, respectively. These findings highlight the influence of mass flow rates and time of day on the heat transfer performance of the system.

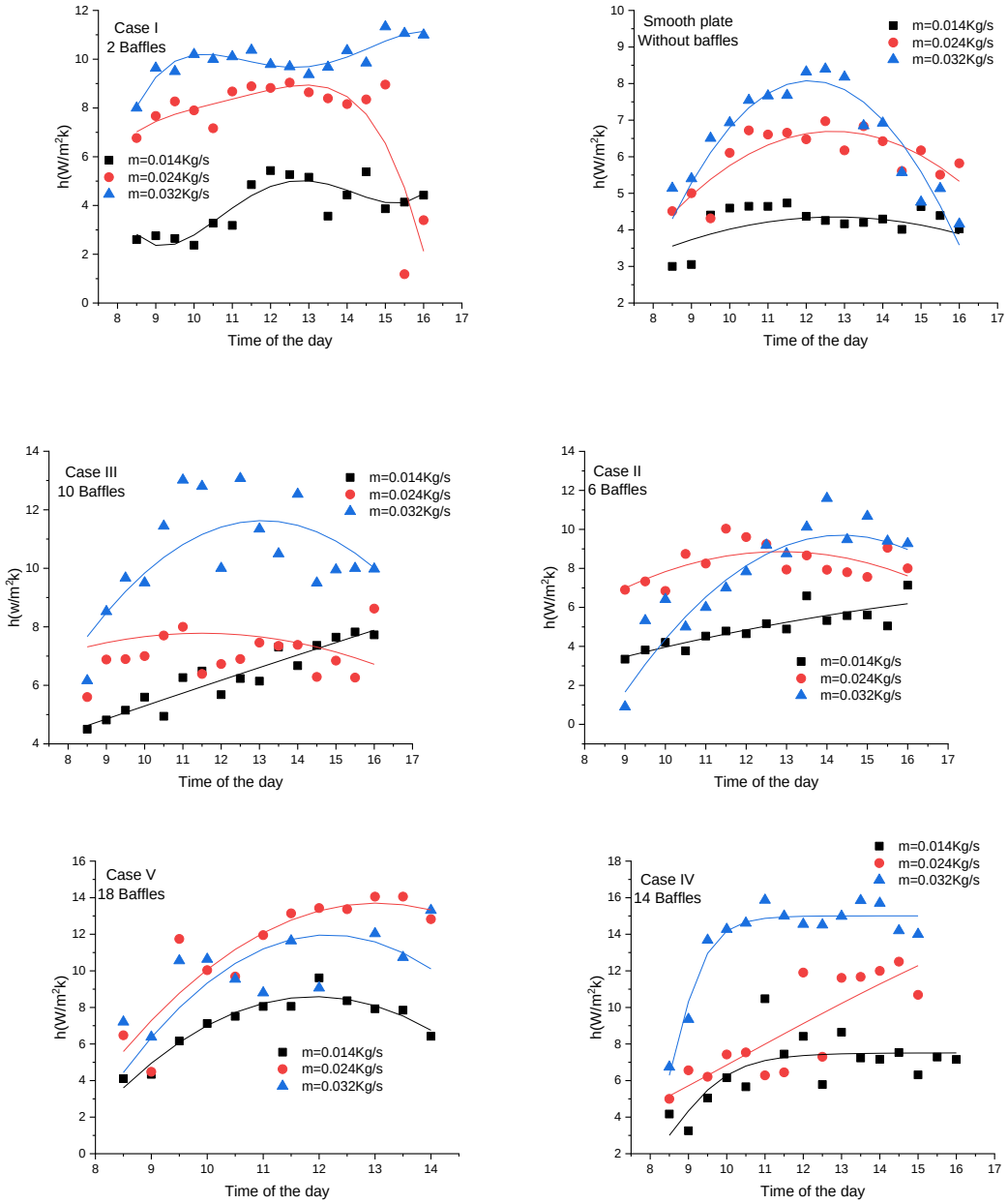

Figure IV14. The heat transfer coefficient as a function of hours of the day at different flows in all cases.

IV.2.3.4 ***Pressure drop***

The effect of two parameters on the hydraulic performance of the studied situations was investigated: the angle of inclination of the collector and the number of baffles, this property was studied by changing the angle of inclination of the collector from β=0° to β=55. Fig IV.15 illustrates the results of changing these parameters while also varying the mass flow rates. The pressure drop, which is a crucial characteristic in this study, showed a small effect due to the angle of inclination of the collector. This is because the pressure drop is primarily influenced by

the flow rather than gravity. On the other hand, the number of baffles had a noticeable impact on hydraulic performance. The increase in the number of baffles led to an increase in pressure drop, as bottlenecks were created by the baffles. Similarly, an increase in mass flow rates resulted in an increase in pressure drop. These observations suggest that hydraulic performance is affected by the number of baffles and the flow rate. The highest pressure drop value was recorded in case V, where ΔP reached 15.2Pa at a mass flow rate of m=0.075kg/s.

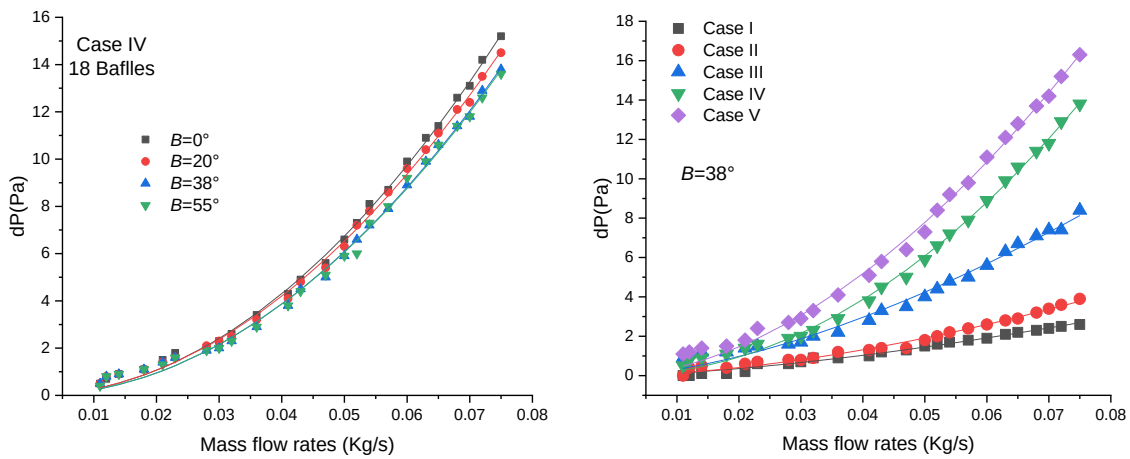

Figure IV.15 The pressure drop as a function of mass flow rates and different angles of inclination.

IV.2.3.5 ***Thermal efficiency***

In this section, we will discuss and focus on thermal efficiency of the collector. Fig IV.16 shows the variations in thermal efficiency at three different mass flow rates throughout the day, specifically from 11:00 to 14:00 when solar radiation was at its highest. All cases with different baffle configurations used in the experimental investigation were considered. The results indicate that thermal efficiency increases with an increase in mass flow rates. This is due to an increase in heat transfer between the absorber plate and the air, as observed in the previous results where the temperature of the absorber plate decreased. It is noteworthy that all cases reached their maximum thermal efficiency at the flow rate of m=0.032kg/s.

Thermal efficiency is a crucial characteristic that has been studied for the cases of obstacles; the two cases 14M134, and 18M135 were found to have the highest thermal efficiency. The best case was 18M135, which reached a maximum value of 0.73 at 12:30 and mass flow m=0.032kg/s. This is attributed to the increase in air turbulence intensity inside the channel caused by the baffles. The more baffles there are, the higher the rate of turbulence intensity, which breaks the dead thermal layers close to the walls and enhances the thermal energy transfer process. On the other hand, the reference case (smooth plate case) recorded the lowest values of thermal efficiency, especially at mass flow m=0.014kg/s. In summary, the process of improving heat transfer and enhancing thermal performance in general can be achieved by increasing the number of baffles, mass flow, or solar radiation.

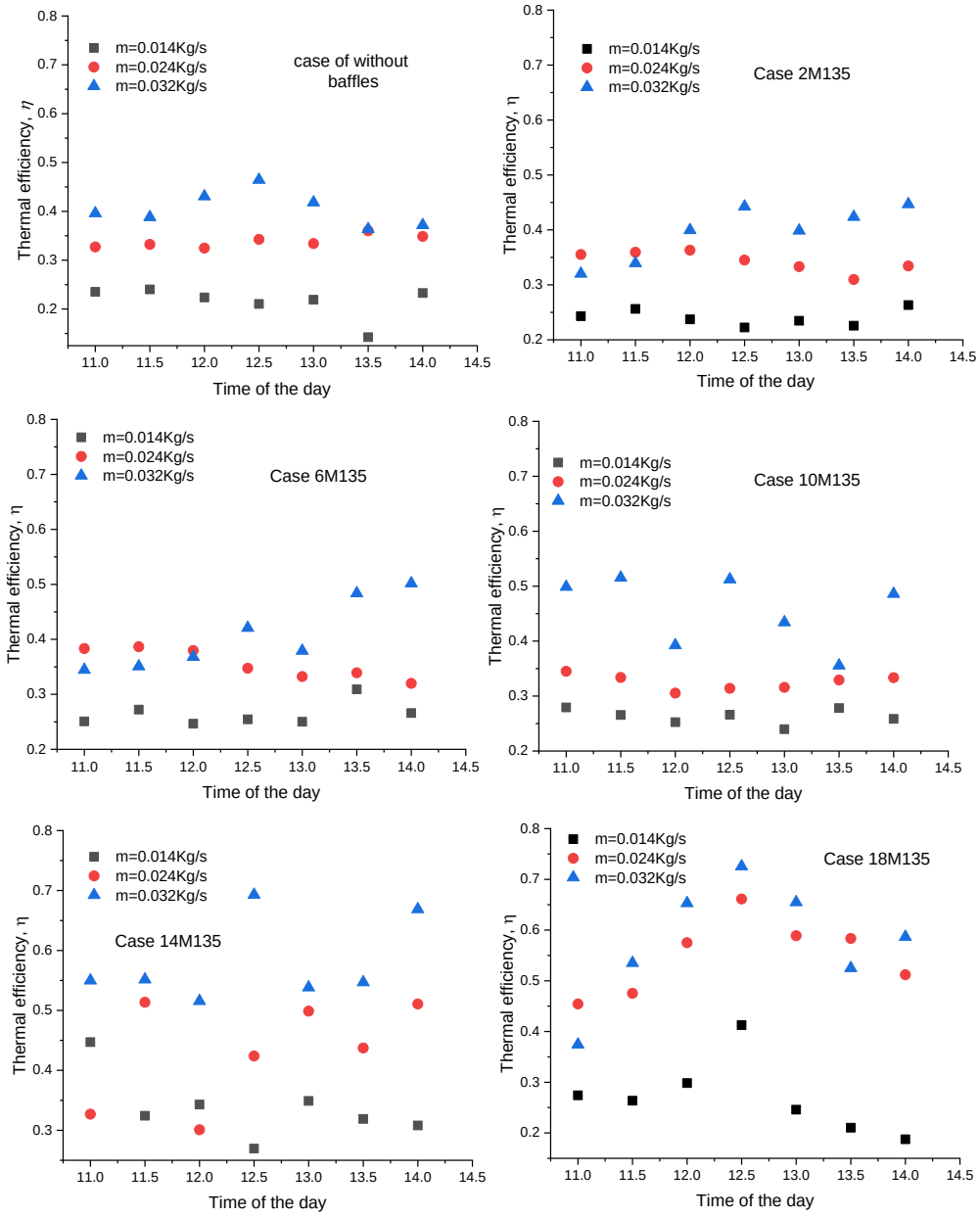

Figure IV16. The thermal efficiency as a function of hours of the day at different flows for all cases

IV.3 The first part of the numerical study

The purpose of the first section of the numerical study was to examine the impact of an increase in the number of baffles at an angle of inclination of 135 degrees. The study consisted of five cases in total, including a reference case, which served as a baseline for comparison. The reference case was initiated from the middle, and then the number of obstacles gradually increased from both ends. The four additional cases were designed to test the effects of increasing the number of obstacles on various parameters, such as velocity, pressure, and turbulence intensity. The results of this section of the study were crucial in understanding how

changes in the number and placement of obstacles can affect fluid flow dynamics. The criteria that have been used in this study are based on a thorough review of the literature and a consideration of the findings of many previous studies. These criteria have been carefully selected and refined to ensure that they are relevant, reliable, and valid indicators of the phenomenon under investigation. The criteria have been widely used and widely accepted in the field and are considered to be the most appropriate for this study. By relying on these established criteria, the results of this study can be compared to those of other studies and can be considered part of the larger body of knowledge in this area. Furthermore, the use of well-established criteria adds to the robustness and credibility of the findings [68-70].

IV.3.1 Evaluation of the Nusselt number

In Fig IV.17, we observe the variation of the average Nusselt number as a function of Reynolds number for all studied cases and the smooth plate reference case. As Reynolds number increases, the Nusselt number also increases for all cases, and the Nusselt number is higher than the reference case (without baffles) for all studied cases. The case with 18 baffles exhibited the highest Nusselt values (Nu=49.40 at Re=10257), while the case with 6 baffles had the lowest values (Nu=21.92 at Re=4362). This indicates that the addition of baffles and an increase in mass flow rate significantly increase the Nusselt number. This is primarily due to the mixing of air between the baffles, which leads to the cracking of thermal layers, and especially near the absorber wall.

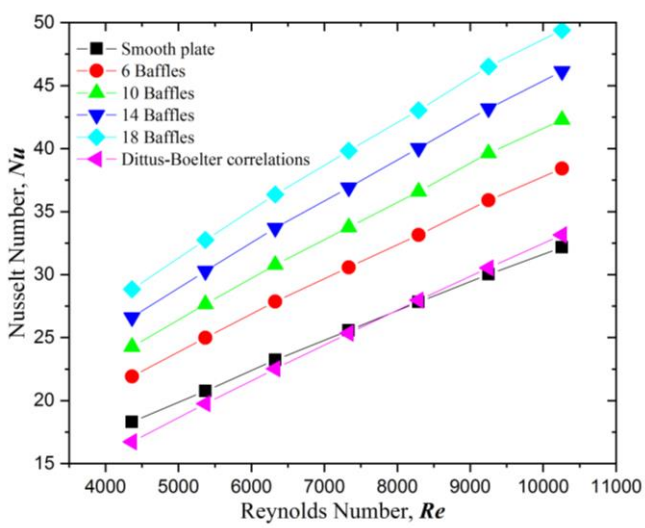

Figure IV.17 Nusselt number in terms of Reynolds number for all cases.

IV.3.2 Pressure drop

Fig IV.18 shows the change in pressure drop as a function of Reynolds number. Based on the curves, the reference case is observed to have the lowest pressure drop among all the cases analyzed, with the minimum recorded value being ΔP=0.62 Pa at the Reynolds number of Re=4362. However, the presence of 18 baffles inside the channel leads to a significant increase in

pressure drop, as it reaches its highest value of ΔP=78.9 Pa at the Reynolds number of Re=10257. This increase in pressure drop results from the baffles obstructing the airflow, leading to a rise in the resistance to fluid flow. Despite the improvement in heat transfer, this increase in pressure drop has a negative impact on the performance of the collector.

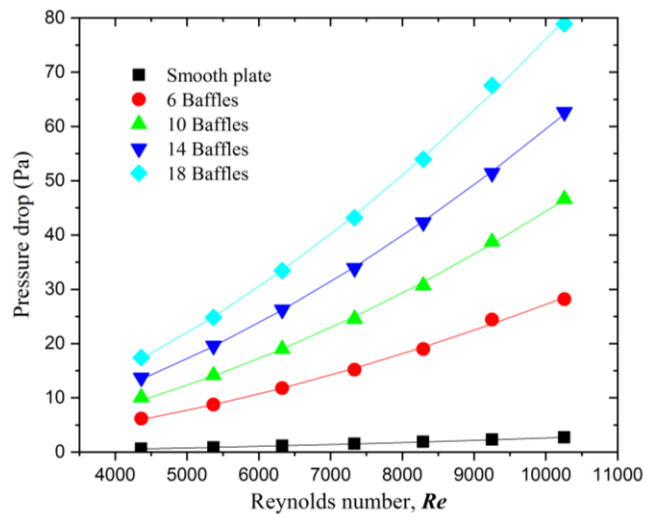

Figure IV.18 Pressure drop as a function of Reynolds number for all cases.

IV.3.3 Evaluation of the heat transfer coefficient

The heat transfer coefficient is a crucial parameter that defines the efficiency of the studied model. It represents the amount of heat transferred per unit area per unit time per unit temperature difference, and is widely used to evaluate the thermal performance of various systems. Hence, a comprehensive understanding of the heat transfer coefficient is essential to optimize the design of the studied model and ensure optimal heat transfer performance.

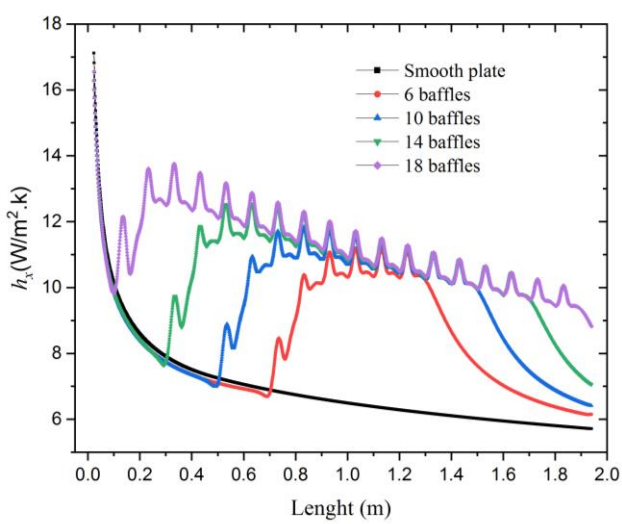

Figure IV.19 The local heat transfer coefficient as a function of the lenght channel at Re=5368.

Fig IV.19 presents the variation of the local heat transfer coefficient through forced convection along the channel, encompassing all modes, including the reference case. The primary objective of this study is to comprehend the underlying mechanism responsible for the impact of baffles on heat transfer from the absorber plate to the surrounding air. The depicted curve illustrates a consistent decrease in the heat transfer coefficient for all cases, with a subsequent increase occurring at the first baffle position until reaching a specific limit. Beyond this limit, the heat transfer coefficient gradually declines. These observations align with the findings reported by Tao et al The effect of baffles becomes evident at each peak in the curve, with the number of peaks corresponding to the number of baffles, as documented by Lee et al.[71] in 2001 (Figs IV.20, 21). The increase in the transmission coefficient is attributed to the air mixing and alteration of its flow path towards the absorber plate, effectively disrupting the stagnant thermal boundary layers at each baffle level. Notably, an increase in the Reynolds number has been observed to result in an augmented heat transfer coefficient across all cases. To specifically explore the impact of the Reynolds number, eighteen baffles (18b) were selected, while the remaining cases underwent similar variations in accordance with the changes in the Reynolds number.

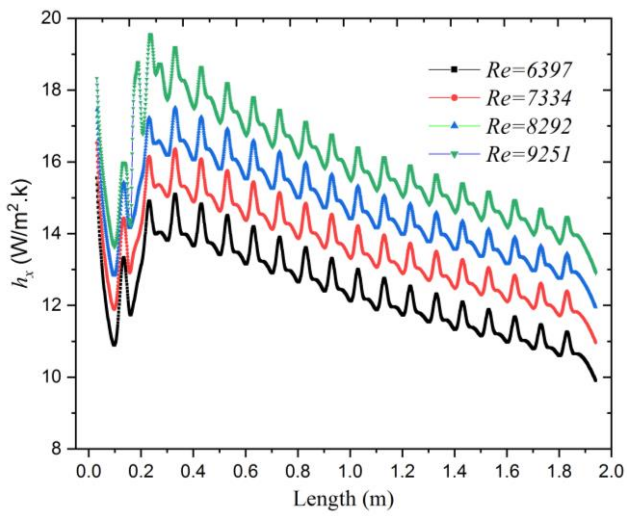

Figure IV.20 The local heat transfer coefficient as a function of the length of channel for the case of 18 baffles at different Reynolds numbers.

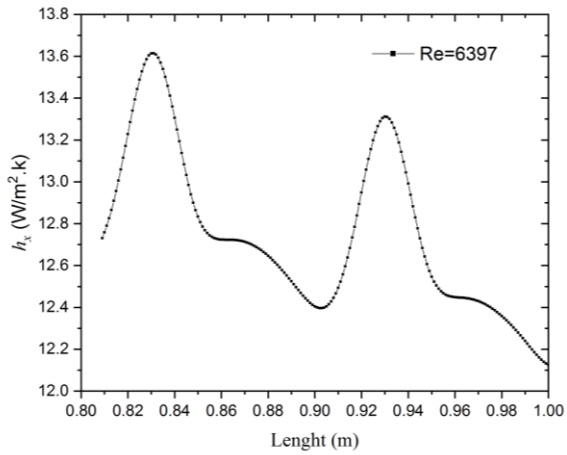

Figure IV.21 local heat transfer coefficient as a function of the lenght (18 baffles case).

IV.3.4 Evaluation of the friction factor

It is important to consider both heat transfer and pumping power when improving SACs. In order to evaluate pumping power, the friction factor was calculated and compared for each case to the reference case (without baffles). Fig IV.22 shows the friction factor ratios f/f_0 as a function of Reynolds number (Re) for all studied cases. It was observed that the friction factor increased slightly with an increase in Reynolds number for all cases. Moreover, it was found that the number of baffles has a significant impact on the friction factor, where an increase in the number of baffles leads to an increase in the friction factor. The increase in the friction factor ratio was almost the same between all cases, with the highest value observed in the case of 18 baffles, where f/f_0=28.69 at Re=8292, and the lowest values were recorded in the case of 6 baffles, where the lowest value was f/f_0=9.29 at Re=4362. Therefore, any modification to the SAC design should consider the trade-off between heat transfer enhancement and increased pumping power.

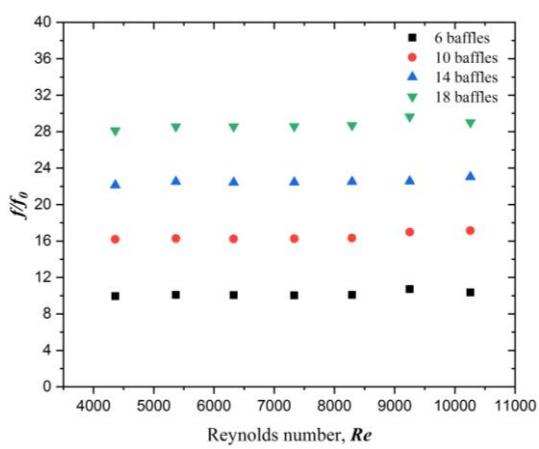

Figure IV.22 The friction factor as a function of Reynolds number in all cases.

IV.3.5 The thermo-hydraulic performance factor (THPF)

Webb, Eckert et al., [59]. have defined a parameter to assess the effectiveness of channels with baffles in different geometric shapes, positions, and numbers. The THPF combines the hydraulic and thermal performance of the collector and provides insight into its thermal efficiency. (Layek et al [72]; Aravindh et al [73]; Menasria et al [58]).

For all cases studied at Reynolds numbers ranging from Re=4362 to Re=10257, the THPF was found to be less than unity (>1). The THPF is determined based on the Nusselt number and friction factor for channels with and without baffles, represented by Nu, f and Nu_0, f_0, respectively. Fig IV.23 illustrates the change in the THPF as a function of the Reynolds number in all cases.

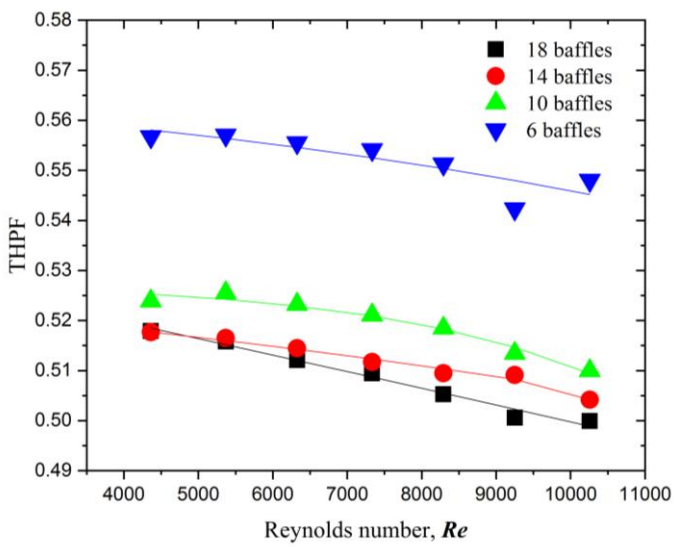

Figure IV.23 The THPF as a function of Reynolds numbers for all cases.

The results showed that the THPF slightly increased in cases with 6 and 10 baffles from Re=4362 to Re=5368, as depicted in Fig IV.23. However, it decreased at higher Reynolds numbers. This finding is consistent with the results of Menasria et al. [58]. The highest THPF values were observed when six baffles were placed in the middle of the duct, where the maximum value of THPF=0.557 was recorded at Re=5368. The study also found a significant difference between the case with 6 baffles and the other three cases, with the lowest value of THPF recorded in the case with 18 baffles (THPF=0.499 at Re=10257). Thus, the economic aspect should be considered when selecting the number of baffles since some cases may have different numbers of baffles but still yield the same THPF. For example, the cases with 18 and 14 baffles have the same THPF at Reynolds numbers from Re=4362 to Re=7334.

Figure IV.24 Velocity path lines between two baffles (18 baffles case at Re=9515).

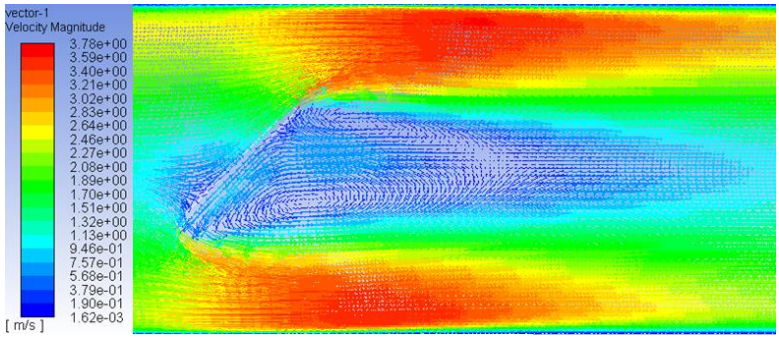

Figure IV.25 Velocity field and the direction of vortices at the level of baffle (18 baffles case at Re=9515).

The shape of the baffles and the channel generates swirls or recirculation regions, as depicted in Fig IV.24. The swirls are composed of two vortices, a primary and a secondary one. The secondary vortex has the same direction as the clockwise turnover, while the primary vortex has the reverse direction. Unlike most studies, there were not many vortices, indicating the airflow's ability to pass through the top and bottom and between baffles. As the Reynolds number and the distance between baffles increased, these vortices grew longer, as confirmed by Menasria, Zedairia et al. [58] Fig IV.25 shows the change in the velocity field, indicating that the areas between baffles act as transit areas. By examining the velocity field, it is noted that there is a cracking of the dead layers in the absorber plate's wall at these areas, which explains the high local heat transfer coefficient at each baffle.

IV.4 The second part of the numerical study

The second part of the numerical study focuses on investigating the influence of the location and angle of inclination of obstacles on the performance of a thermal collector. In this section of the study. Four baffles with different inclination angles were used, with the location and angle of inclination of the obstacles varied from one case to the next. The objective of this part of the study was to determine the optimal arrangement of obstacles in terms of enhancing heat transfer and optimizing thermal performance. This section of the study involved performing a series of simulations using computational fluid dynamics (CFD) techniques to model the fluid flow and heat transfer within the thermal collector. The results of this section of the study will provide valuable information for the design and optimization of thermal collectors and will contribute to the development of more efficient and effective systems for harnessing solar energy.

This part aimed to investigate the impact of different formations of mode H on the airflow and thermal performance of an air duct collector. To achieve this, simulations were conducted using computational fluid dynamics (CFD). The first formation studied was H right, where six baffles were placed on the right-hand side of the air duct, next, the H middle formation was investigated, where six baffles were placed in the middle of the air duct, the third formation studied was H left, where six baffles were placed on the left-hand side of the air duct, Finally, the H all formation was studied, where eighteen baffles were placed all over the air duct (Fig IV.26).

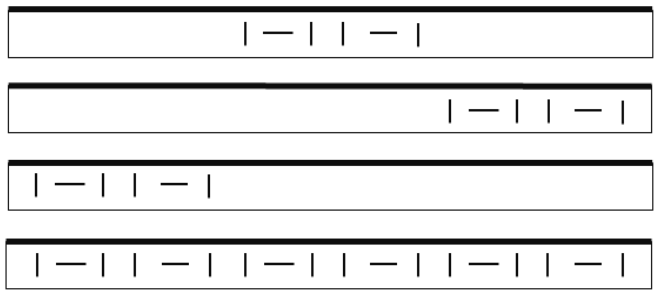

Figure IV.26 The studied modes.

IV.4.1 Evaluation of the Nusselt number

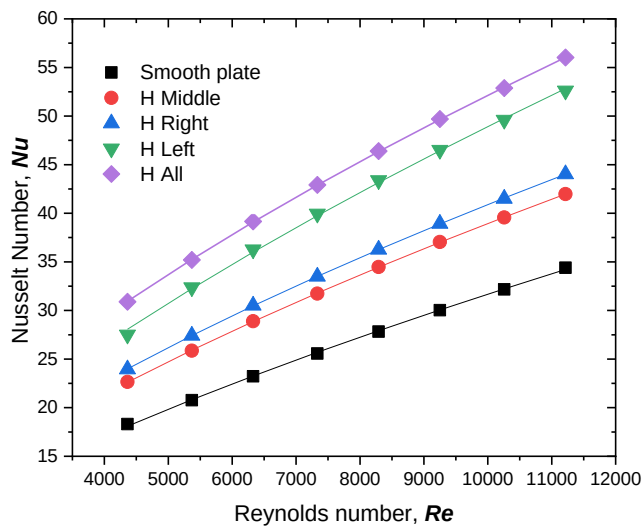

Figure IV.27 Change in Nusselt number in terms of Reynolds number for all cases

Through Fig IV.27, we notice that the number of Nusselt increases with the increase in the Reynolds number in all cases, which indicates an increase in heat transfer inside the collector, the best cases in heat transfer was the case H full then H left, The highest value recorded was in the case of H full, where it was Nu=56.03 at Re=11216, and the lowest value was in the case of the smooth plate (without baffles) where its value was Nu=18.31 at Re=4362.

IV.4.2 Evaluation of the heat transfer coefficient

To understand the mechanism of heat transfer along the channel more in this part of the results we discuss the local heat transfer coefficient in terms of local transfer and also in terms of different Reynolds numbers.

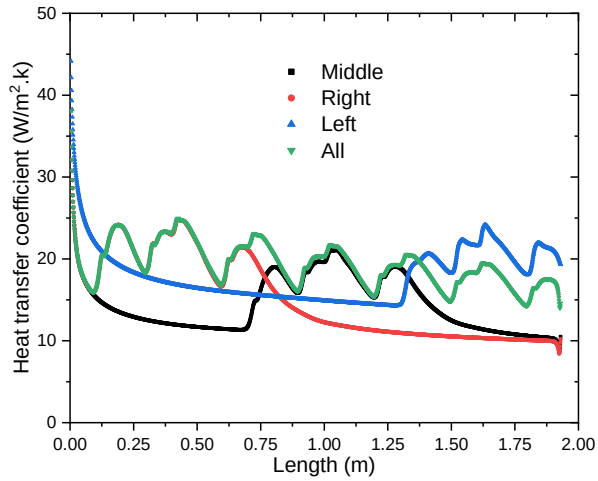

Figure IV.28 Change in the local heat transfer coefficient in terms of the local change for all positions.

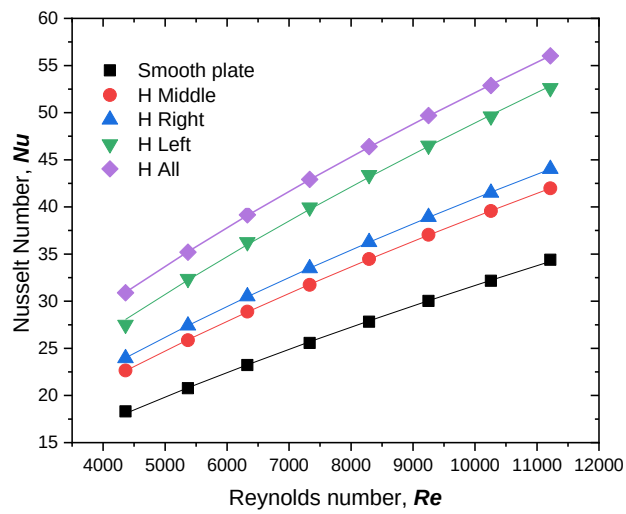

Figure IV.29 Change in Nusselt number in terms of Reynolds number for all cases.

Fig IV.28 represents the local heat transfer coefficient in terms of length in the four cases. We note that the local heat transfer coefficient significantly decreases at the beginning of the channel in all cases due to the difference in temperature between the absorber plate and the incoming air, which was high at the beginning, and with the movement of air inside the channel, this difference begins to decrease due to the acquisition of air and the loss of thermal energy from the absorber plate

Through Fig IV.29, we notice that the number of Nusselt increases with the increase in the Reynolds number in all cases, which indicates an increase in heat transfer inside the collector, the best cases in heat transfer was the case H full then H left, The highest value recorded was in the case of H full, where it was Nu=56.03 at Re=11216, and the lowest value was in the case of the smooth plate (without baffles) where its value was Nu=18.31 at Re=4362.

To understand the mechanism of heat transfer along the channel more in this part of the results we discuss the local heat transfer coefficient in terms of local transfer and also in terms of different Reynolds numbers.

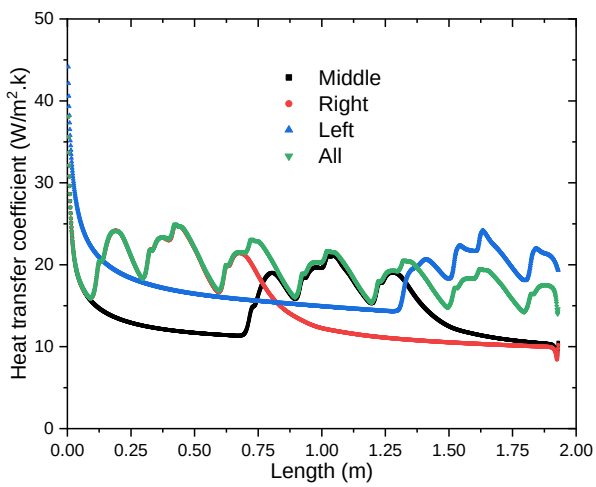

Figure IV.30 Change in the local heat transfer coefficient in terms of the local change for all positions.

Fig IV.30 represents the local heat transfer coefficient in terms of length in the four cases. We note that the local heat transfer coefficient significantly decreases at the beginning of the channel in all cases due to the difference in temperature between the absorber plate and the incoming air, which was high at the beginning, and with the movement of air inside the channel, this difference begins to decrease due to the acquisition of air and the loss of thermal energy from the absorber plate Inside the duct, at every positioning of the baffles, there is a noticeable rise in the value of the local heat transfer coefficient, and this is due to the turbulence caused by these baffles on the airway, whose seeds cause the cracking of the dead thermal layers close to the absorber plate, and then increase the transfer of thermal energy inside the duct at this the level.

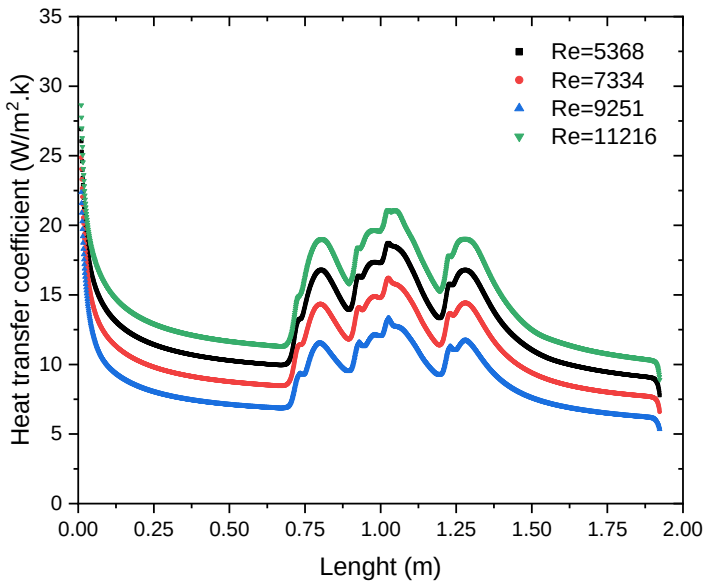

Figure IV.31 Change in the local heat transfer coefficient of the case H middle for different Reynolds numbers.

Furthermore, the effect of increasing the Reynolds number on the heat transfer inside the channel is studied. We notice that every growth in the Reynolds number is accompanied by an expansion in the heat transfer along the air channel Fig IV.31.

IV.4.3 Contours of temperature

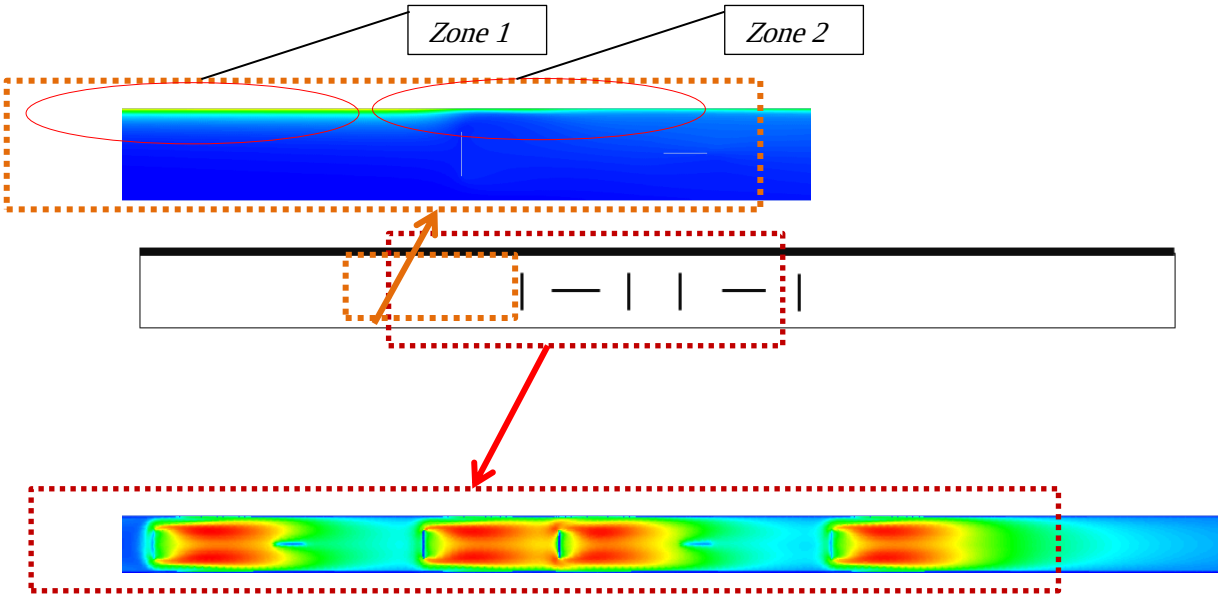

Figure IV.32 Contours of turbulent intensity, mode H middle at Re=10257.

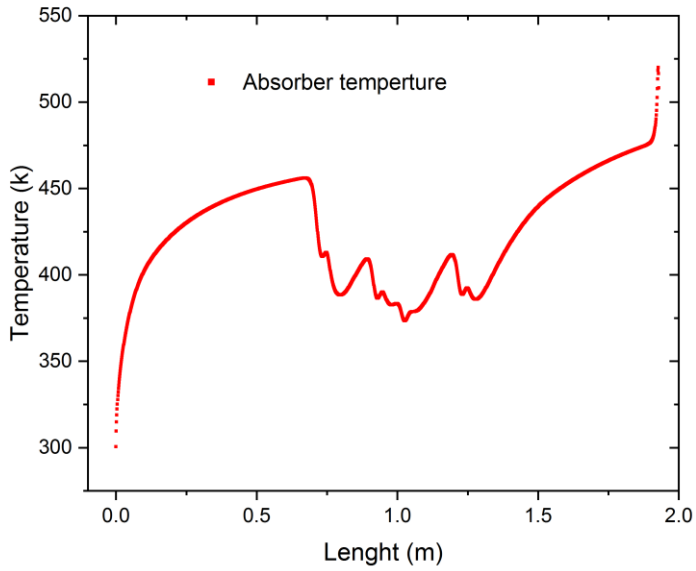

Figure IV.33 Temperature of the absorber plate as a function of channel length.

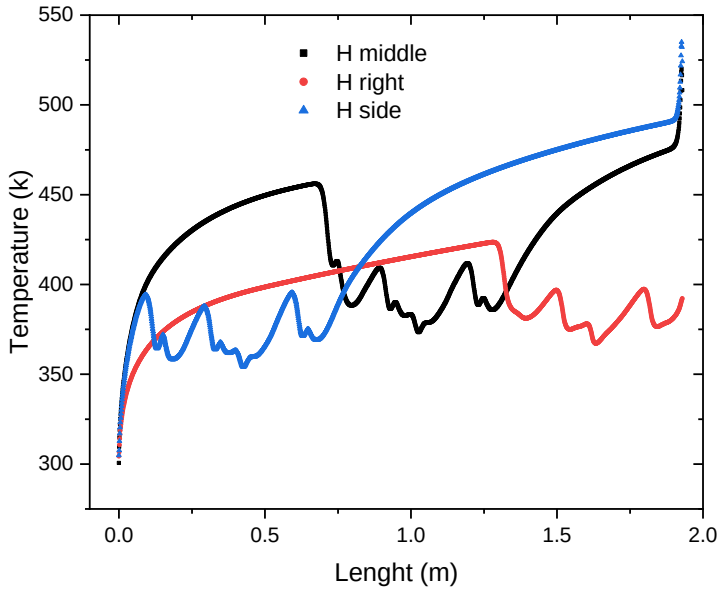

Figure IV.34 Temperature of the three modes (with the same number of baffles).

Fig IV.32 represents the contours of turbulent intensity in the case of H middle at Reynolds number Re=10257. Through this contour, we notice that the presence of obstacles creates a high intensity of turbulence; this leads to the removal of dormant thermal layers near the walls, especially the wall of the absorber plate.

As shown in the thermal field, we can distinguish two stages: before and after the baffles. There is a noticeable decrease in the temperature of the absorber plate in zone 2 (after the baffles) compared to zone 1. This explains the high heat transfer coefficient at each location of the baffles along the duct where the percentage of increase in the heat transfer coefficient was about X=60%, compared to the case of the absence of baffles (Figs IV.33, 34).

IV.4.4 Evaluation of the friction factor

Hydraulic performance is also essential in thermal collectors, as it determines the economic losses of these transformers, so in this part of the study, the friction coefficient f has been studied.

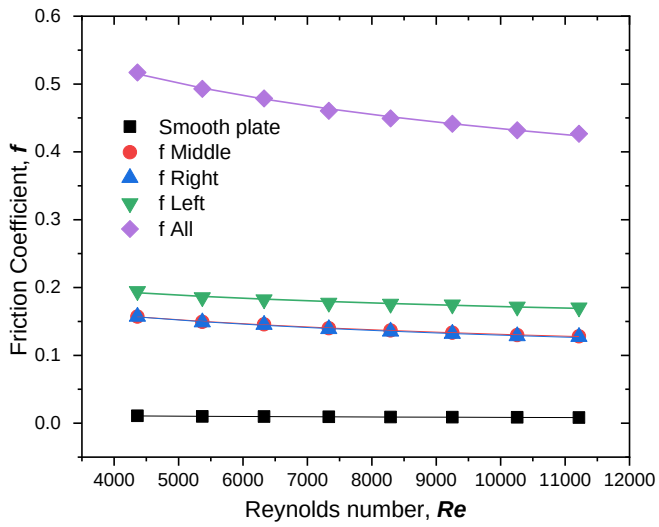

Figure IV.35 Change of the Friction coefficient as a function of Reynolds number.

The first noticeable observation is that all the coefficients were less than one; the maximum value was in the H all mode at Reynolds Re=11216, and the lowest values were recorded in the reference mode, that is, without baffles and ranged between f=0.0108 and f=0.0084. In terms of the change curve, it was a descending curve in all cases; as the Reynolds number increases, the Friction coefficient decreases. There is a big difference between the values of the coefficient of friction in the three modes (H Right, H Left, H Middle) compared to the mode of H All Fig IV.35. Moreover, we have confirmed that the Friction coefficient is not only related to the number of baffles and air velocity, but also the location of these baffles has a minor effect on this coefficient, as in the cases H left and H right.

IV.4.5 The thermo-hydraulic performance factor (THPF)

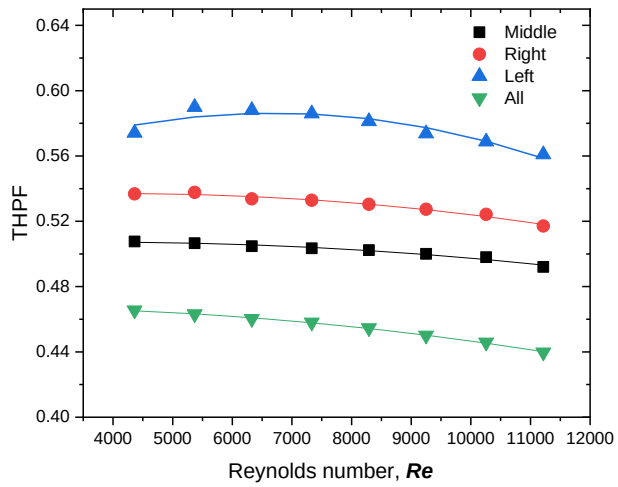

Figure IV.36 The THPF as a function of Reynolds number for all modes.

The THPF is what determines the thermal efficiency of this collector, taking into account the economic aspect. Based on the results, we found that the lowest Thermo-hydraulic performance factor (THPF) values (THPF=0.465 to THPF=0.439) were in the first position (H All) Fig IV.35. That is due to the high friction coefficient that was recorded. The highest noticeable values of this factor were in mode (H left), where the highest recorded value was THPF=0.0.59 at Reynolds Re=5368. Through this paper, we conclude that not only does the shape and number of baffles affect the Thermo-hydraulic performance, but that the same number and shape of baffles placed in different positions yield varied results. That is indeed an advantage since, using the same model and number; we can improve the hydraulic and thermal aspects by merely changing their position.

IV.5 Conclusion

This chapter presents numerical and experimental results of energy transfer inside the collector duct. All thermal properties have been studied for different modes, three of which have the same number of baffles in various locations with the case without baffles, in addition to the four formations at an angle of inclination 135°. As for the numerical part, the CFD analysis was accomplished using Ansys Fluent software 18.1. In this analysis, the number of nodes was chosen based on the proximity to the uncertainty of the extracted results. The turbulence model was also determined by comparing all turbulence models to the Dittus-Boelter correlation. Through the results, the following was uncovered:

The baffles have a close relationship with the heat of the absorber plate and the local heat transfer coefficient, as they create turbulence in their location, which affects the heat of the

absorber plate in the exact locale of the baffles themselves, and eventually, the overall local heat transfer.

It is not only the number and angle of inclination of baffles that affects the thermal-hydraulic performance, but even the location has a significant impact on them.

The CFD is an effective model that we can rely on in the future without referring to experimental limitations.

General conclusion

General conclusion

SACs are becoming an increasingly popular choice for heating and ventilating buildings, particularly in areas with abundant sunlight. However, to achieve optimal thermal performance, it is important to consider the design and conception of the SAC. As noted in the review of research, it's one key area for improvement to the use of specific baffles, to enhance heat transfer and increase efficiency. The baffles are used to disrupt the path lines of air-flow within the duct, creating turbulence that helps to increase the surface area available for heat exchange. The specific shape, size, orientation, and arrangement of these baffles can have a significant impact on performance. The researchers have explored various options to find the most effective designs.

This study aimed to investigate the potential of using obstacles to enhance the thermal and hydraulic performance of SACs, to achieve this and trying to conduct both experimental, and numerical simulations using CFD.

In the experimental phase, have constructed a prototype SAC with a rectangular duct, where the air was passed between the bottom, and the absorber plate. To enhance the heat transfer process various obstacles was introduced, in the flow path. After the enhancement, the stage of measuring the thermal and hydraulic performance of the system comes, under different operating conditions, including different flow rates and solar radiation levels.

In parallel, we conducted numerical simulations using CFD to investigate the fluid flow and heat transfer characteristics of the collector with and without baffles. The simulation results provided a detailed understanding of the complex fluid dynamics and heat transfer mechanisms, allowing us to optimize the design and placement of the baffles for maximum performance.

The results of our study showed that the introduction of obstacles in the flow path led to a significant improvement in the thermal and hydraulic performance of the SAC. The turbulent flow created by the obstacles to increase the heat transfer coefficient between the absorber plate and the passing air, resulting in higher thermal efficiency. Furthermore, the obstacles also helped to reduce pressure drop, improving the hydraulic efficiency of the system.

Our findings demonstrate the potential of using obstacles to enhance the performance of SACs, providing an effective and practical solution for improving energy efficiency and reducing the pressure drop. This work also highlights the importance of combining experimental and numerical approaches to gain a comprehensive understanding of fluid dynamics and heat transfer mechanisms in complex thermal collector.

In the experimental results focus on the thermal performance, according to five cases, and its results were shown that increasing the number of baffles used increases the heat transfer process inside the collector, this was shown by the heat transfer coefficient, the local heat transfer coefficient, and the Nusselt number; where the maximum values were h=15.84 and 17.46 W/m^2k in the two cases case V, and case IV respectively. The results also showed that the angle of

inclination of the SAC almost does not effect on the pressure drop, as for increasing the obstruction or the mass flow increases the pressure drop. For the study inside the channel, maximum values were recorded at L=0.375m in the local Nusselt number in the case 6M135 at all mass flow rates. Case 18M135 was chosen as the best case, through heat transfer, where the highest thermal efficiency values were recorded, the maximum value Ŋ=0.73 at 12:30 and mass flow m=0.032kg/s. with a small hydraulic performance compared to the literature.

In terms of the numerical study, the study was divided into two parts, one section concerned with the effect of the placement of obstacles, and the second section concerned with the effect of their number, so we start with the effect of their numbers, rectangular baffles were added perpendicularly to the air duct at an angle of inclination of 135°, and four cases, including the smooth duct, were analyzed using CFD Ansys Fluent 18.1. After selecting the turbulence model and verifying the accuracy of the numerical model through experimental investigation, the thermal and hydraulic performance of the studied thermal heater was evaluated using parameters such as Nusselt number, heat transfer coefficient, friction coefficient, and the THPF. Through a comprehensive analysis of these cases, the following observations were made:

- The RNG k-ε model is the turbulence model that gives closer results to the standard correlations of Dittus-Boelter and Modified Blasius.
- Adding baffles and increasing airflow rates in all cases leads to an increase in heat transfer. The case with 18 baffles at the highest Reynolds number (Re = 10257) recorded the highest Nusselt rate.
- The coefficient of friction f/f_0 is similarly affected by the increase in heat transfer, but the increase is slight when the Reynolds number increases.
- The local heat transfer coefficient in the duct changes with the position of every baffle, resulting in an increase in heat transfer from the absorber to the air. A remarkable peak was observed at each baffle due to the cracking of the dead thermal layers below the absorber.
- Heat transfer decreases from the inlet of the channel towards the outlet, while the absorber temperature increases in all cases.
- The cases with 10, 14, and 18 baffles showed a large convergence through the THPF, while there was a considerable difference between these cases and the case of 6 baffles which was selected as the best case for Re = 5368.
- Conducting an experimental investigation is costly in terms of effort, time, and money. However, by following the protocol used in this research, many experiments can be conducted using CFD only after validation.
- Increasing the number of baffles does not always improve both the thermal and hydraulic properties simultaneously.

From the second aspect of the numerical study, where the effect of the placement of obstacles was studied, its results showed the following:

- The baffles have a close relationship with the heat of the absorber plate and the local heat transfer coefficient, as they create turbulence in their location, which affects the heat of the absorber plate in the exact locale of the baffles themselves, and eventually, the overall local heat transfer.
- When both hydraulic and thermal performances are taken into account, the optimal model to be used is H left.
- It is not only the number and angle of inclination of baffles that affects the thermal-hydraulic performance, but even the location has a significant impact on them.
- The CFD is an effective model that we can rely on in the future without referring to experimental limitations.

References

1. Twldell, J. and W. Gillett, *JS Hsieh. Solar Energy Engineering. Prentice-Hall, Inc. Englewood Cliffs, New Jersey (1986). ISBN 0-I 3-822446-3 A comprehensive introductory text to solar.*
2. BENSACI, C.E., *Effect of the artificial roughness dispositions on the thermal exchanges in a flat solar collector*, 2021, Université Mohamed Khider–Biskra.
3. Kaygusuz, K., *Energy for sustainable development: A case of developing countries.* Renewable and Sustainable Energy Reviews, 2012. **16**(2): p. 1116-1126.
4. Javaid, M., et al., *Understanding the adoption of Industry 4.0 technologies in improving environmental sustainability.* Sustainable Operations and Computers, 2022.
5. Kalogirou, S.A., *Solar thermal collectors and applications.* Progress in Energy and Combustion Science, 2004. **30**(3): p. 231-295.
6. Aouissi, Z. and F. Chabane, *Numerical and experimental study of thermal efficiency of the transversal rectangular baffles with incline angle inside of solar air collector.* Energy Sources, Part A: Recovery, Utilization, and Environmental Effects, 2022. **44**(4): p. 8921-8942.
7. Kreith, F., *Solar heating and cooling: active and passive design*. 1982: CRC Press.
8. Aouissi, Z., et al., *Numerical and experimental investigations of heat transfer inside a rectangular channel with a new tilt angle of baffles for solar air heater.* Journal of Renewable Energy and Technology, 2023. **1**(1): p. 9-15.
9. Aouissi, Z., F. Chabane, and M.-S. Teguia, *Improving the thermal efficiency of solar air collector by creating turbulent flow using a new baffles combinations.* Iranian (Iranica) Journal of Energy & Environment, 2023: p. -.
10. Chabane, F. and N. Moummi, *Heat transfer and energy analysis of a solar air collector with smooth plate.* The European Physical Journal Applied Physics, 2014. **66**(1).
11. Ameur, H., *Effect of the baffle inclination on the flow and thermal fields in channel heat exchangers.* Results in Engineering, 2019. **3**.
12. Aouissi, Z., et al., *Determination of the heat transfer coefficient by convection, according to shape of the baffles (solar air collector).* Journal of Renewable Energies, 2022. **25**(1): p. 43–54-43–54.
13. Chabane, F. and Z. Aouissi, *Experimental investigations on the thermal efficiency of a solar air collector with transverse rectangular baffles incline by an angle of 135°.* Energy and Built Environment, 2023.
14. Khanlari, A., et al., *Experimental and numerical study of the effect of integrating plus-shaped perforated baffles to solar air collector in drying application.* Renewable Energy, 2020. **145**: p. 1677-1692.

15. Phu, N.M., P.B. Thao, and N. Van Hap, *Effective efficiency assessment of a solar air heater having baffles spaced with different successive ratios.* Case Studies in Thermal Engineering, 2021. **28**: p. 101486.
16. El-Said, E.M.S., *Numerical investigations of fluid flow and heat transfer characteristics in solar air collector with curved perforated baffles.* Engineering Reports, 2020. **2**(4).
17. Olfian, H., A. Zabihi Sheshpoli, and S.S. Mousavi Ajarostaghi, *Numerical evaluation of the thermal performance of a solar air heater equipped with two different types of baffles.* Heat Transfer, 2020. **49**(3): p. 1149-1169.
18. Ho, C.-D., et al., *Performance improvement of a double-pass solar air heater with fins and baffles under recycling operation.* Applied Energy, 2012. **100**: p. 155-163.
19. Chabane, F., N. Moummi, and A. Brima, *Experimental study of thermal efficiency of a solar air heater with an irregularity element on absorber plate.* International Journal of Heat and Technology, 2018. **36**(3): p. 855-860.
20. Bensaci, C.-E., et al., *Numerical and experimental study of the heat transfer and hydraulic performance of solar air heaters with different baffle positions.* Renewable Energy, 2020. **155**: p. 1231-1244.
21. Menni, Y., et al., *Heat transfer in air flow past a bottom channel wall-attached diamond-shaped baffle–using a CFD technique.* Periodica Polytechnica Mechanical Engineering, 2019. **63**(2): p. 100-112.
22. Menni, Y., A. Azzi, and A. Chamkha, *The solar air channels: comparative analysis, introduction of arc-shaped fins to improve the thermal transfer.* Journal of Applied and Computational Mechanics, 2019. **5**(4): p. 616-626.
23. Menni, Y., A.J. Chamkha, and A. Azzi, *Fluid flow and heat transfer over staggered '+ ' shaped obstacles.* Journal of Applied and Computational Mechanics, 2020. **6**(4): p. 741-756.
24. Khanoknaiyakarn, C., S. Kwankaomeng, and P. Promvonge. *Thermal performance enhancement in solar air heater channel with periodically V-shaped baffles*. in *2011 International Conference & Utility Exhibition on Power and Energy Systems: Issues and Prospects for Asia (ICUE)*. 2011. IEEE.
25. Hu, J., et al., *Performance improvement of baffle-type solar air collector based on first chamber narrowing.* Renewable Energy, 2019. **135**: p. 701-710.
26. Karim, M.A. and M.N.A. Hawlader, *Development of solar air collectors for drying applications.* Energy Conversion and Management, 2004. **45**(3): p. 329-344.
27. Wang, D., et al., *Evaluation of the performance of an improved solar air heater with "S" shaped ribs with gap.* Solar Energy, 2020. **195**: p. 89-101.
28. Ozgen, F., M. Esen, and H. Esen, *Experimental investigation of thermal performance of a double-flow solar air heater having aluminium cans.* Renewable Energy, 2009. **34**(11): p. 2391-2398.

29. Chabane, F., et al., *Experimental study of a solar air heater by adding an arrangement of transverse rectangular baffles perpendicular to the air stream.* International Journal of Green Energy, 2019. **16**(14): p. 1264-1277.
30. Chamoli, S. and N.S. Thakur, *Effect of roughness height ratio in V down perforated baffle roughness on thermohydraulic performance of solar air heater: an experimental study.* International Journal of Ambient Energy, 2013. **36**(5): p. 242-247.
31. Karwa, R., *Experimental studies of augmented heat transfer and friction in asymmetrically heated rectangular ducts with ribs on the heated wall in transverse, inclined, V-continuous and V-discrete pattern.* International Communications in Heat and Mass Transfer, 2003. **30**(2): p. 241-250.
32. Singh, A.P. and O. Singh, *Performance enhancement of a curved solar air heater using CFD.* Solar Energy, 2018. **174**: p. 556-569.
33. Patil, A.K., J. Saini, and K. Kumar, *Experimental investigation of enhanced heat transfer and pressure drop in a solar air heater duct with discretized broken V-rib roughness.* Journal of Solar Energy Engineering, 2015. **137**(2): p. 021013.
34. Arunkumar, H.S., K. Vasudeva Karanth, and S. Kumar, *Review on the design modifications of a solar air heater for improvement in the thermal performance.* Sustainable Energy Technologies and Assessments, 2020. **39**.
35. Chabane, F., N. Moummi, and S. Benramache, *Experimental study of heat transfer and thermal performance with longitudinal fins of solar air heater.* J Adv Res, 2014. **5**(2): p. 183-92.
36. Aoues, K., et al., *Amélioration des performances thermiques d'un capteur solaire plan à air: Etude expérimentale dans la région de Biskra.* 2009. **12**(2): p. 237–248-237–248.
37. Moummi, N., et al., *Energy analysis of a solar air collector with rows of fins.* Renewable Energy, 2004. **29**(13): p. 2053-2064.
38. Esen, H., *Experimental energy and exergy analysis of a double-flow solar air heater having different obstacles on absorber plates.* Building and Environment, 2008. **43**(6): p. 1046-1054.
39. Youcef-Ali, S., *Study and optimization of the thermal performances of the offset rectangular plate fin absorber plates, with various glazing.* Renewable Energy, 2005. **30**(2): p. 271-280.
40. Mahboub, C., et al., *Experimental study of new solar air heater design.* International Journal of Green Energy, 2016. **13**(5): p. 521-529.
41. Ural, T., *Experimental performance assessment of a new flat-plate solar air collector having textile fabric as absorber using energy and exergy analyses.* Energy, 2019. **188**.
42. Fiuk, J.J. and K. Dutkowski, *Experimental investigations on thermal efficiency of a prototype passive solar air collector with wavelike baffles.* Solar Energy, 2019. **188**: p. 495-506.

43. AISSAOUI, F., *Contribution à l'étude de transfert de chaleur d'un capteur solaire placé dans un climat aride: cas de la région de Biskra*, 2017, Université Mohamed Khider-Biskra.
44. Yeh, H.-M. and C.-D. Ho, *Collector Efficiency in Downward-Type Internal-Recycle Solar Air Heaters with Attached Fins.* Energies, 2013. **6**(10): p. 5130-5144.
45. Naphon, P. and B. Kongtragool, *Theoretical study on heat transfer characteristics and performance of the flat-plate solar air heaters.* International Communications in Heat and Mass Transfer, 2003. **30**(8): p. 1125-1136.
46. Sopian, K., et al., *Thermal performance of the double-pass solar collector with and without porous media.* 1999. **18**(4): p. 557-564.
47. El-Sebaii, A.A., et al., *Investigation of thermal performance of-double pass-flat and v-corrugated plate solar air heaters.* Energy, 2011. **36**(2): p. 1076-1086.
48. Thakur, D.S., M.K. Khan, and M. Pathak, *Performance evaluation of solar air heater with novel hyperbolic rib geometry.* Renewable Energy, 2017. **105**: p. 786-797.
49. Hernández, A.L., J.E. Quiñonez, and F.H. López, *Transient numerical study of thermo-energetic performance of solar air heating collectors with metallic porous matrix.* Solar Energy, 2019. **178**: p. 181-192.
50. Jha, R., et al., *Performance prediction of a solar heated house.* Energy Conversion and Management, 1992. **33**(4): p. 263-273.
51. Tyagi, R., R. Ranjan, and K. Kishore, *Performance studies on flat plate solar air heater subjected to various flow patterns.* Applied Solar Energy, 2014. **50**: p. 98-102.
52. Ho, C.D., et al., *The influences of recycle on performance of baffled double-pass flat-plate solar air heaters with internal fins attached.* Applied Energy, 2009. **86**(9): p. 1470-1478.
53. Chabane, F., et al., *Prediction of solar radiation according to aerosol optical depth.* Iranian (Iranica) Journal of Energy & Environment, 2020. **11**(4): p. 271-276.
54. Chabane, F., et al., *Theoretical Study of Global Solar Radiation on Horizontal Area for Determination of Direct and Diffuse Solar Radiation.* Iranian (Iranica) Journal of Energy & Environment, 2023. **14**(1): p. 9-16.
55. Aouissi, Z., et al., *Optimization of the heat exchange by adding the baffles to the streaming duct of the solar air collector.* Iranian (Iranica) Journal of Energy & Environment, 2022.
56. Kline, S.J., *Describing uncertainty in single sample experiments.* Mech. Engineering, 1953. **75**: p. 3-8.
57. Chabane, F., et al., *Influence of the rectangular baffle on heat transfer and pressure drop in the solar collector.* Energy Sources, Part A: Recovery, Utilization, and Environmental Effects, 2020: p. 1-17.

58. Menasria, F., M. Zedairia, and A.J.E. Moummi, *Numerical study of thermohydraulic performance of solar air heater duct equipped with novel continuous rectangular baffles with high aspect ratio.* Energy. 2017. **133**: p. 593-608.
59. Webb, R., E.J.I.J.o.H. Eckert, and M. Transfer, *Application of rough surfaces to heat exchanger design.* International journal of heat and mass transfer. 1972. **15**(9): p. 1647-1658.
60. Patankar, S.J.N.Y., *Numerical heat transfer and fluid flow Hemisphere Publishing Corporation.* 1980.
61. Cengel, Y.A., *Introduction to thermodynamics and heat transfer*. Vol. 846.
62. Fox, R.W., A.T. McDonald, and J.W. Mitchell, *Fox and McDonald's introduction to fluid mechanics*. 2020: John Wiley & Sons.
63. Duffie, J.A., W.A. Beckman, and W.J.N.Y.e.W. Worek, *Solar engineering of thermal processes (Vol. 3).* 1980.
64. Karmare, S. and A.J.S.E. Tikekar, *Analysis of fluid flow and heat transfer in a rib grit roughened surface solar air heater using CFD.* Solar Energy. 2010. **84**(3): p. 409-417.
65. Yadav, A.S. and J.J.I.J.o.T.S. Bhagoria, *A numerical investigation of square sectioned transverse rib roughened solar air heater.* International Journal of Thermal Sciences. 2014. **79**: p. 111-131.
66. Jin, D., et al., *Numerical investigation of heat transfer and fluid flow in a solar air heater duct with multi V-shaped ribs on the absorber plate.* Energy. 2015. **89**: p. 178-190.
67. Safer, N., M. Woloszyn, and J.J.J.S.E. Roux, *Three-dimensional simulation with a CFD tool of the airflow phenomena in single floor double-skin facade equipped with a venetian blind.* Solar Energy. 2005. **79**(2): p. 193-203.
68. Ben Slama, R., M. Bouabdallah, and M. Le Ray, *Improvement of turbulence in the solar collectors with air by the use of baffles in order to increase the efficiency.* Proceedings of COMAGEP1, Marrakech, May, 1994: p. 4-6.
69. Hachemi, A., *Contribution to obtaining the thermal performances of the plane solar air colectors, at bed furnished with lines of obstacles with tight steps*, 1992, Doctorate thesis, University of Valenciennes, France, December.
70. Dutta, S., et al. *Experimental study of heat transfer coefficient enhancement with inclined solid and perforated baffles*. in *International mechanical engineering congress and exposition, ASME paper*. 1997.
71. Lee, C., S.J.I.C.i.H. Abdel-Moneim, and M. Transfer, *Computational analysis of heat transfer in turbulent flow past a horizontal surface with two-dimensional ribs.* International Communications in Heat and Mass Transfer. *2001.* ***28****(2): p. 161-170.*

72. Layek, A., J. Saini, and S.J.R.E. Solanki, *Effect of chamfering on heat transfer and friction characteristics of solar air heater having absorber plate roughened with compound turbulators.* Renewable energy. 2009. **34**(5): p. 1292-1298.
73. Aravindh, M. and A.J.I.J.o.G.E. Sreekumar, *Efficiency enhancement in solar air heaters by modification of absorber plate-a review.* International journal of green energy. 2016. **13**(12): p. 1209-1223.